Automated Cell-targeted Electrophysiology In Vivo and Non-invasive Gamma Frequency Entrainment

by

Ho-Jun Suk

B.S., Cornell University (2008)
M.S., University of Illinois at Urbana-Champaign (2009)

Submitted to the Harvard-MIT Program in Health Sciences and Technology, in Partial Fulfillment of the Requirements for the Degree of

Doctor of Philosophy

at the

MASSACHUSETTS INSTITUTE OF TECHNOLOGY

June 2019

Signature redacted

Signature of Author.....
Harvard-MIT Program in Health Sciences and Technology
May 20, 2019

Signature redacted

Certified by.....
Ed Boyden, PhD
Y. Eva Tan Professor in Neurotechnology
Associate Professor of Biological Engineering and Brain and Cognitive Sciences, MIT Media Lab and McGovern Institute
Thesis Supervisor

Signature redacted

Accepted by.....
Emery N. Brown, MD, PhD
Director, Harvard-MIT Program in Health Sciences and Technology
Professor of Computational Neuroscience and Health Sciences and Technology

Automated Cell-targeted Electrophysiology In Vivo and Non-invasive Gamma Frequency Entrainment

by

Ho-Jun Suk

Submitted to the Harvard-MIT Program in Health Sciences and Technology
on May 20, 2019 in Partial Fulfillment of the
Requirements for the Degree of Doctor of Philosophy in
Medical Engineering and Medical Physics

ABSTRACT

Targeted patch clamp recording is a powerful method for characterizing visually identified cells in intact neural circuits, but it requires skill to perform. We found that a closed-loop real-time imaging strategy, which continuously compensates for cell movement while approaching the cell with a pipette tip, allows for the development of an algorithm amenable to automation. We built a robotic system that can implement this algorithm and validated that our system can automatically patch fluorophore-expressing neurons of multiple types in the living mouse cortex, with yields comparable to skilled human experimenters. By facilitating targeted patch clamp recordings *in vivo*, our robot may enable scalable characterization of identified cell types in intact neural circuits. Activities of individual neurons in neural circuits give rise to network oscillations, whose frequencies are closely related to specific brain states. For example, network oscillations in the 30 - 90 Hz range, observed using electroencephalogram (EEG), are called gamma oscillations and increase during attention, memory formation, and recall. In Alzheimer's disease (AD), gamma oscillations are disrupted compared to healthy individuals. Recently, non-invasive visual and auditory stimulations at 40 Hz, called Gamma ENtrainment Using Sensory stimulus ("GENUS"), have been shown to positively impact pathology and improve memory in AD mouse models, with concurrent visual and auditory GENUS leading to a more widespread effect in the AD mouse brain compared to visual or auditory stimulation alone. However, it is unclear what effect such sensory stimulations would have on the human brain. To test for the safety and feasibility of GENUS in humans, we developed a device that can deliver 40 Hz light and sound stimulations at intensity levels tolerable to humans. We found that our device can safely lead to steady 40 Hz entrainment in cognitively normal young (20 – 33 years old) and older (55 – 75 years old) subjects, with concurrent visual and auditory stimulation leading to stronger and more widespread entrainment than visual or auditory stimulation alone. These findings suggest that GENUS can be a safe and effective method for widespread 40 Hz entrainment, which may have therapeutic effects in people suffering from AD.

Thesis Supervisor: Ed Boyden, PhD
Title: Y. Eva Tan Professor in Neurotechnology
Associate Professor of Biological Engineering and Brain and Cognitive Sciences, MIT
Media Lab and McGovern Institute

ACKNOWLEDGEMENTS

First, I would like to thank my thesis supervisor, Professor Ed Boyden. Ed has been a tremendous mentor for me, giving me the opportunity to work on extremely fun and impactful projects, and also continuously providing invaluable advice along the way to help me reach the goals we had for the projects. His tireless desire to "solve the brain" and "make the world better", in addition to his out-of-this-world work ethic, has motivated and encouraged me to try to be the best researcher that I could be. My time in Ed's lab has been truly a blessing.

I am also extremely grateful for my thesis committee chair, Professor Li-Huei Tsai. Despite her busy schedule, she immediately agreed to be my chair when I asked, and she has continued to provide invaluable guidance and advice since then. Li-Huei has also been such a great PI to collaborate with, always appreciating my contribution no matter how small they had been. Li-Huei's love for research and her amazing drive to solve the aging brain have been truly inspiring.

I would also like to thank my committee members Professor Adam Cohen and Doctor Emery Brown. I really appreciate not only that Adam agreed to be on my committee even though I have never met him before and pretty much cold-emailed him, but also that he has provided a unique perspective on my projects that really helped them to be better. It was also a blessing for me to have Emery in my committee, getting the opportunity to learn so much about EEG, statistical analysis, and human trials. Emery was always happy to make time to meet with me to answer my questions and provide insightful advice, and I am extremely grateful for his time and help.

I also need to thank many (past and present) members of the Boyden lab. A big thank you has to go to Holly Birns, our lab's wonderful administrative assistant, who found a date and time for my defense that worked for all of my committee members (which really seemed to be an impossible task for me, given the busy schedule of my committee members). I want to thank Lisa Lieberson and Macey Lavoie as well, for all of their help with ordering and other important tasks that they helped me with. I am also very grateful for Dr. Ingrid van Welie. Ingrid was the one who actually made the imagepatching project possible, and I was so lucky to have had a chance to work with her on it. Without her expertise in *in vivo* patching and her patience with me as she was teaching me how to patch, the imagepatcher would not have been possible. I also need to thank Professor Suhasa Kodandaramaiah, Dr. Brian Allen, Dr. Giovanni Talei Franzesi, Demian Park, and Professor Craig Forest for their help with the imagepatcher project. I cannot count how many times I had to bug Suhasa, Brian, Giovanni, and Demian with questions about patching, but no matter how stupid my questions were, they were always extremely helpful with their answers and advice. I am also grateful for Professor Annabelle Singer, who gave me the opportunity to be involved in the collaboration with the Tsai lab.

There are many people in the Tsai lab for whom I am extremely grateful. Dr. Hannah Iaccarino and Dr. Anthony Martorell have been great colleagues, and it was so fun working with them. I also need to thank Dr. Diane Chan, Brennan Jackson, Vanesa Fernandez, Sara Beach (from the Gabrieli lab), Danielle Stark, Noah Milman, and Colton Stearns (a.k.a. the human gamma team). The human gamma work would not have been possible without them, and I

consider myself truly blessed to have had the opportunity to work with these smart and fun people. I also would like to thank Dr. Chinnakkaruppan Adaikkan, Dr. Hansruedi Mathys, and Dr. Jennie Young for extremely helpful discussions on GENUS and Alzheimer's Disease.

I would also like to acknowledge Dr. Emily Stephen, Professor Seong-Eun Kim, Professor Francisco Flores, and Dr. Sourish Chakravarty for their help on EEG data analysis.

I am also grateful for Samsung Scholarship, not only for providing the support I need to study and learn at MIT, but also for providing the opportunity to make Samsung Scholar colleagues and friends.

There are not enough words in this world to describe my appreciation and love for my parents, who have sacrificed so much for me and my brother. Their unconditional love has been and always will be what drives me to be a better person and a better parent myself. Hyungjun, my younger brother, has been such a great sibling, taking care of me even though I was the one who was supposed to take care of him and being my best friend as we lived through some tough times together. I am truly blessed to have such loving and wonderful family.

어머니, 아버지, 항상 저를 사랑으로 보살펴주시고 너무나도 좋은 롤모델이 되어주셔서 감사해요. 표현이 서툴러 지금까지 잘 나타내지 못했지만 항상 사랑하고 감사드려요. 항상 건강하시고 또 감사드려요.

형같은 동생 형준아, 항상 나에게 너무나도 좋은 형제가 되어주고 도움을 주어서 고마워. 서로 다른 곳에서 다른길을 가기에 예전만큼 함께하는 시간을 많이 없지만 그래도 항상 고맙고 사랑해. 형준이가 선택한 길에서 잘 해나가는 것 같아 너무 뿌듯하고 자랑스러워. Keep it up!

Most importantly, I would like to thank my wonderful wife Seonggyeong (Joy) Yun. My life would have been so much different without her love, encouragement, support, patience, and everything else. Seonggyeong fills my life with happiness and love, and I really look forward to spending the rest of my life with her. I also want to thank Arin, our baby daughter. She puts a smile on my face every day, and she has given me the opportunity to look at my life in a bigger context. Thank you and I love you Seonggyeong and Arin!

사랑하는 성경아, 긴 박사생활동안 항상 나를 사랑해주고 응원해줘서 고마워. 힘들고 어려운 시간들이 지나고 같이 되돌아 봤을때, 서로 마주보며 웃을 수 있게 더욱 열심히 노력할게. 많이 사랑해.

사랑하는 아린아, 내 이쁜 딸! 엄마와 아빠에게 와준 선물. 엄마와 아빠가 아린이 많이 사랑해. 지금처럼 건강하고 씩씩하게 자라줘~ 사랑해.

TABLE OF CONTENTS

Chapter 1: Introduction

The mammalian brain is composed of more than billion neurons (Nowakowski, 2006), each of which are capable of performing computations and transmitting information in the form of ionic currents through membrane channels and resulting electrical potentials. These individual neurons are intricately connected to one another to form networks, and synchronized neuronal activity within these networks results in brain waves that oscillate at various frequencies (Buzsáki and Draguhn, 2004). Understanding how neuronal activity and oscillations are related to higher order brain functions is one of the grand challenges in neuroscience. To tease out this relationship, tools that can accurately record and control neuronal activity are required.

The patch clamp technique, which utilizes a glass electrode to achieve electrical isolation of a patch of cell membrane, enables low-noise, high-temporal resolution recordings and manipulations of these electrical signals. Although recent advancements in sensor proteins, actuator proteins, and optical tools have enabled "all-optical" approaches to electrophysiology (Hochbaum et al., 2014; Kiskinis et al., 2018; Zhang et al., 2018), it is challenging to record signals on a millisecond timescale using these approaches, which is easily achievable with patch clamp recordings. In addition, the development and application of new optical methods still require validation using patch clamp recordings.

The patch clamp technique has found its use in a wide range of applications that span from the measurement of ionic currents through transmembrane channel proteins of denervated frog muscle fibers at its inception (Neher and Sakmann, 1976) to the characterization of identified cell types in the mammalian brain (Chen et al., 2015; Gentet et al., 2010, 2012; Pala and Petersen, 2015; van Welie et al., 2016) to functional studies of individual cells in brain disorders (Arispe et al., 1996; Dragicevic et al., 2015; Ibáñez-Sandoval et al., 2007; Nieweg et al., 2015). Similar to other techniques in the biological sciences that have become standardized tools, initial improvements of patch clamp that were focused on optimizing manual operations are now being followed by innovations enabling automation for better ease-of-use, reproducibility, throughput, and standardization.

1.1. Initial development of patch clamp technique *in vitro*

When the patch clamp technique was first developed by Neher and Sakmann in 1976, they used heat-polished pipettes with a tip diameter of 3 – 5 μm to measure the current from enzymatically cleaned cell membrane surface (Neher and Sakmann, 1976; Sakmann and Neher, 1984). To reduce noise due to the leakage shunt between the cell membrane and the bath, the pipette had to be pressed onto the surface of the cell membrane, forming an electrical seal with tens of MΩ resistance between the pipette tip and the membrane (Neher and Sakmann, 1976). It was later discovered that light suction applied to the pipette upon contact between the pipette tip and the cell membrane can increase the seal resistance to above a gigaohm (i.e., result in a gigaseal; Hamill et al., 1981; Sigworth and Neher, 1980). This discovery was important, because it improved the recording quality of the patch clamp technique (Sakmann and Neher, 1984) and enabled the development of different recording configurations (Hamill et al., 1981). These configurations include cell-attached, whole-cell, outside-out, and inside-out, each of which is best suited for different applications.

The need for direct contact between the pipette tip and the cell membrane limited the use of the patch clamp technique to isolated cells that have their membranes exposed (e.g., cultured cells on a dish), until it was discovered that neurons in mammalian brain slices can be patched after brief treatment of the tissue slices with proteolytic enzymes (Gray and Johnston, 1985). However, since proteolytic enzymes may damage the proteins on the cell membrane of interest, different approaches were sought and developed. To enable direct contact between the tip of a patch pipette and the tissue-covered cell membrane, these approaches implemented either a two-step process in which a separate, "cleaning" pipette was first used to remove the part of the tissue covering the cell body of interest (Edwards et al., 1989) or a one-step process in which positive pressure was applied to a patch pipette as it was penetrating the tissue and approaching the cell membrane (Blanton et al., 1989). The integration of differential interference contrast (DIC) optics was another major advancement for enabling patch clamping in brain slices, as the improved imaging quality offered by DIC-based microscopy enabled visually-guided patching of soma as well as dendrites of targeted neurons in mammalian brain slices (Stuart et al., 1993). DIC-based visually-guided patch clamping has become a standard method for studying neurons in brain slices. Finally, it is also possible to combine cell type-specific fluorescent labeling (e.g., as available in transgenic mice) and fluorescence imaging (e.g., using an epifluorescence microscope) with patch clamping to investigate genetically-defined neuronal classes *in vitro* (e.g., Ting et al., 2014).

1.2. Patch clamp recordings *in vivo*

Although brain slices preserve synaptic connections immediate to the cells of interest and enable investigation of neuronal activity in relatively intact local circuits, more insightful understanding of neuronal function under normal physiological conditions and its significance for higher order functions, such as sensory information processing, perception, and memory, can only be achieved in *in vivo* preparations. The first successful *in vivo* whole-cell patch clamp recordings were demonstrated in the visual cortex of live, anesthetized cats (Pei et al., 1991). Although these recordings were with an "incomplete" seal (i.e., the seal resistance was 100 – 300 MΩ), this work hinted at the possibility of obtaining successful patch clamp recordings *in vivo*. Several years later, it was demonstrated that whole-cell patch clamp recordings can be obtained from awake, head-fixed rodents (Lee et al., 2006, 2009; Margrie et al., 2002), establishing the patch clamp technique as an invaluable tool for correlating single neuron activity to higher order brain functions, such as sensing, movement, and other behaviors.

1.2.1. Blind patch clamp recordings

The first *in vivo* whole-cell patch clamp recordings were performed in a "blind" fashion. In this recording mode, the whole-cell configuration is achieved without any visualization of targeted neurons or patch pipettes. A patch pipette, with positive pressure being applied to its interior, is inserted into the brain to a target depth and then sequentially moved in small (2-3 μm) steps while monitoring the tip resistance. When the pipette tip makes contact with a cell membrane, an increase in the pipette resistance and a pulsation of the pipette current are observed. At this point, the pipette pressure is released and suction is applied to form a gigaseal, followed by short suction pulses leading to break-in of the membrane patch and the whole-cell configuration.

Advantages of the blind patch technique include its (theoretically) unlimited depth of recordings (since the depth of the targeted neurons is not limited by the optical constraints) and relatively large working area above the recording sites (Okada, 2012). While knowledge of the anatomical arrangement of various classes of cells in different brain areas allows one to enhance the probability of targeting specific cell types (e.g. layer V cortical neurons), on the whole, blind patching is not an ideal method for an investigation of specific cell types or cell classes (Margrie et al., 2003).

1.2.2. Image-guided patch clamp recordings

To overcome the limitation of the blind approach described above, *in vivo* two-photon laser scanning microscopy, which enables imaging of fluorescence signals relatively deep into the intact brain (Denk et al., 1994; Helmchen and Denk, 2005; Svoboda et al., 1997), has been integrated with patch clamping. In a method called "two-photon targeted patching" (TPTP; Komai et al., 2006; Margrie et al., 2003), cells that are fluorescently labeled by the generation of transgenic mice (e.g., Meyer et al., 2002) or by the injection of viral vectors (e.g., Callaway, 2005; Komai et al., 2006) are visualized simultaneously with a fluorescent dye-filled patch pipette, using a two-photon microscope. To distinguish the patch pipette from the cells, a fluorescent dye that has a significantly different emission spectrum compared to that of fluorescently labeled cells is used to fill the pipette. Schematic representation of a TPTP setup is shown in Figure 1.1A (adapted from Figure 1 in Komai et al., 2006), together with example dual-channel images of a targeted cell and a patch pipette in Figure 1.1B (adapted from Figure 2 in Margrie et al., 2003).

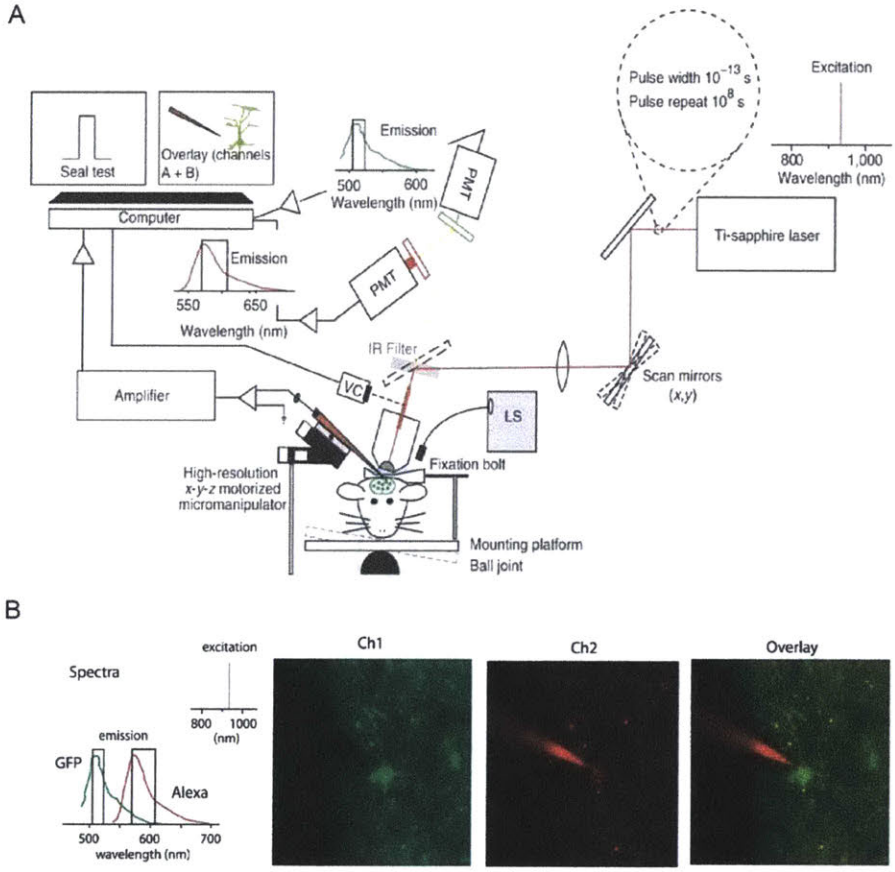

Figure 1.1. Two-photon targeted patching (TPTP).
(A) Schematic of a typical TPTP setup (adapted from Komai et al., 2006). (B) Example dual-channel images of a targeted cell and a patch pipette (adapted from Margrie et al., 2003).

In another method termed "shadow-patching" (Kitamura et al., 2008; Häusser and Margrie, 2014), the extracellular space in the wild-type brain is perfused with a fluorescent dye from a patch pipette, which enables the visualization of unlabeled cells as "shadows" and thus image-guided navigation of the patch pipette to these cells. For both TPTP and shadow-patching, once the pipette is positioned sufficiently close to the targeted cell, confirmation of contact between the pipette tip and the cell membrane, formation of a gigaseal, and rupture of the membrane patch for the whole-cell configuration are performed using similar procedures as in the blind approach.

Compared to the blind approach, image-guided patching is limited to a relatively low depth (~500 μm) due to tissue scattering that limits the imaging depth of two-photon microscopy. Despite this limitation, image-guided patching has been shown to be extremely valuable for cell type-specific characterizations of neurons in the intact brain (Chen et al., 2015; Gentet et al., 2010, 2012; Pala and Petersen, 2015; van Welie et al., 2016). Recent advances in laser scanning microscopy that enable imaging deeper in the intact tissue (e.g., three-photon microscopy described in Horton et al., 2013), combined with the development of improved fluorescent tags (e.g., near-infrared fluorescent proteins described in Piatkevich et al., 2017), may further broaden the application of image-guided patching.

1.2.3. Challenges of patch clamp recordings in vivo

Despite its obvious value as a tool for characterizing the function of cell-types in circuits, the patch clamp technique has not yet become a routine method in biological sciences, because it requires a lot of skill and experience to perform. Consequently, in the case of *in vivo* patch clamp in particular, the technique has been adopted only by a relatively small subset of electrophysiologists. Even for these experts, *in vivo* patching has relatively low data yield (for the blind approach, ~20-30% of pipettes used for patching result in the formation of gigaseal and whole-cell configuration, according to Lee et al., 2009; Margrie et al., 2002; for the two-photon image-guided approach, it is ~10-20%, according to Margrie et al., 2003), emphasizing the need for automated approaches to enable higher yield and throughput.

1.3. Automated patch clamp recordings

To facilitate the use of patch clamp as a standardized tool in biology, several attempts have been made to automate the sequential steps involved in using the technique, for both *in vitro* and *in vivo* preparations. Currently available automated systems and strategies have shown various levels of success at reproducing or surpassing the quality, yield, and throughput of recordings performed by human experimentalists.

1.3.1. Automated patch clamp recordings in vitro

Early efforts to automate the patch clamp technique have led to the development of planar devices for *in vitro* recordings from cultured cells (Dunlop et al., 2008; Okada, 2012). Instead of

the "top-down" approach used in the manual recordings for the pipette-target cell contact formation, these automated systems use a "bottom-up" configuration (Dunlop et al., 2008), in which each well of a multi-well plate has a small aperture on the bottom surface. After the target cells in suspension are introduced into the wells of these systems, a negative pressure is applied through the apertures to bring the cells close and subsequently form a gigaseal. Although these systems enable automated patch clamp recordings with much higher throughput compared to the manual approach, the planar configuration limits their use to cells that can be isolated and suspended in a solution (Okada, 2012).

Automated systems that utilize conventional patch electrodes and sample preparations have also been developed. For example, the multi-electrode patch-clamp system developed by Perin and Markram (2013) is built around a conventional patch rig and simplifies multi-cell patching in brain slices by automating positioning of patch pipettes close to targeted cells. The system also provides a pneumatic system controlled by a human interface device for repeatable and precise pipette pressure adjustments during patching. However, several key steps are still left for human experimenters to perform (e.g., the final approach to contact the cell with the pipette tip; triggering of pressure level adjustments for sealing and breaking in). With this system, twelve neurons could be patched simultaneously in brain slices of rats, far surpassing the number of cells that can be simultaneously patched using a fully manual approach (Perin and Markram, 2013).

A more recent system called the "Autopatcher IG" ("Image-Guided"; Wu et al., 2016) utilizes computer vision-based algorithms for automatic pipette tip calibration and fluorescent cell detection. It also automates pipette navigation to a targeted cell, seal formation, and break-in, providing a platform for fully automated patching of fluorescent cells in brain slices. The system could be used to automate patching of fluorescent layer V neurons in cortical slices of Thy1-ChR2-EYFP mice, obtaining similar recording quality compared to manual patching of neurons in brain slices of wild-type mice. The average times spent for pipette positioning, gigaseal formation, and break-in were also significantly reduced compared to manual patching. For patching non-fluorescent cells in wild-type mice (which required manual cell detection using DIC optics), the system required manual adjustments of pipette positioning for 47.7% of the trials (21 out of 44 trials), mostly caused by inaccuracies in automated micromanipulator positioning or failure of the patching algorithm to form a gigaseal (Wu et al., 2016). For fully automated trials (which accounted for 23 out of 44 trials, or 52.3%) and semi-automated trials (i.e., trials requiring manual adjustments), the rates of achieving the successful whole-cell configuration (defined as the condition in which the cell membrane resistance is lower than 300 MΩ and the holding current is between -200 pA and 100 pA) were 82.6% and 52.4% respectively, while it was 35.3% for manual trials. The seal resistance, the membrane capacitance, the membrane resistance, the access resistance, and the holding current were not significantly different between automatic/semi-automatic patching and manual patching, while the average times spent for pipette placement onto the target cell, gigaseal formation, and break-in were significantly shorter for automatic/semi-automatic patching compared to manual patching.

1.3.2. Automated blind patch clamp recordings in vivo

The first automated system for *in vivo* recordings was developed for blind patching (Kodandaramaiah et al., 2012). The LabVIEW-based system, called the "autopatcher", utilizes an

algorithm that divides the blind patching process into four distinct stages, as shown in Figure 1.2A (Figure 1(a) in Kodandaramaiah et al., 2012).

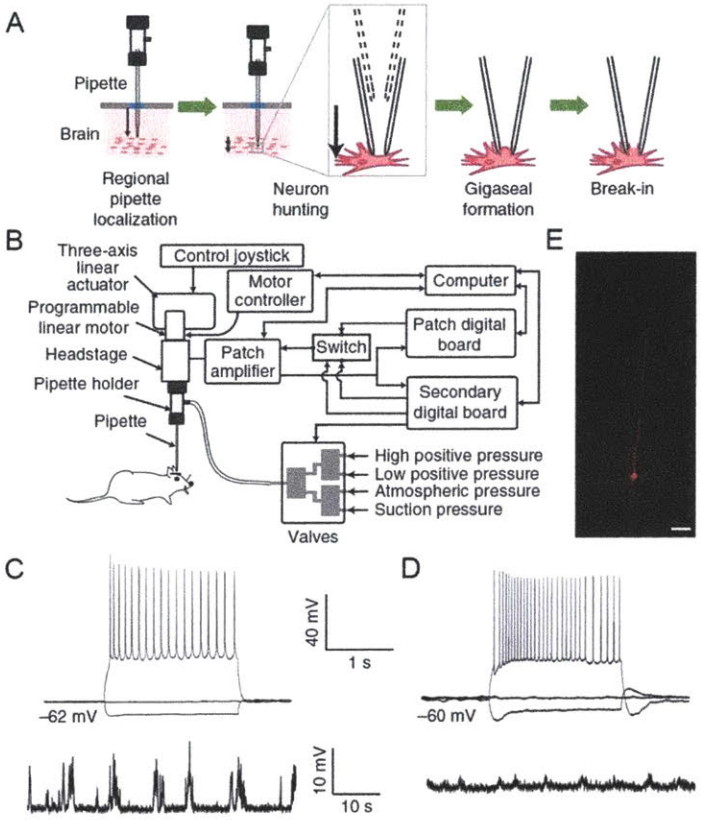

Figure 1.2. The autopatcher algorithm, setup, and performance, as shown in Figure 1 of Kodandaramaiah et al. (2012).
(A) The autopatching algorithm. (B) Schematic of the autopatcher setup. (C) Example current-clamp recordings from an autopatched cortical neuron (top: recordings with 2-s long current injection pulses at -60, 0, and +80 pA; bottom: recording at rest). (D) Example current-clamp recordings from an autopatched hippocampal neuron (top: recordings with 2-s long current injection pulses at -60, 0, and +40 pA; bottom: recording at rest). (E) Example image of a biocytin-filled autopatched cortical neuron.

To run this algorithm, the autopatcher integrates a set of standard patch clamp equipment, such as the pipette holder, the headstage, the patch amplifier, and the patch digital board, with programmable linear motors (for automated pipette navigation), computer-controlled pneumatic valves (for closed-loop pipette pressure modulation), and a digital board (for real-time pipette resistance measurement). Using the autopatcher, successful whole-cell recordings (defined as showing less than 500 pA of current when held at -65 mV for at least 5 minutes) could be obtained from both cortical and hippocampal neurons in anesthetized mice at a rate of 32.9% (gigaseal cell-attached recordings were obtained 36% of the time), which is similar or superior to the success rates for manual *in vivo* patching reported in literature (Kodandaramaiah et al., 2012; Lee et al., 2009; Margrie et al., 2002). In addition, the quality of whole-cell recordings (assessed using access resistance, holding current, resting potential, and holding time) and the time required to obtain whole-cell recordings were similar between autopatching and manual *in vivo* patching

(Kodandaramaiah et al., 2012; Lee et al., 2009; Margrie et al., 2002). It was later shown that the autopatcher could also be used to obtain whole-cell recordings from awake, head-fixed mice, either immobilized or freely-running on a floating ball (Kodandaramaiah et al., 2016). Schematic representation of the autopatcher setup and example recordings obtained using the autopatcher are shown in Figure 1.2B-D (Figure 1(b)-(d) in Kodandaramaiah et al., 2012).

The autopatching algorithm has also been used to enable simultaneous patching of multiple cells (i.e., multi-patching; Kodandaramaiah et al., 2018). The "multipatcher", composed of four interacting autopatching robots, could obtain dual and triple whole-cell recordings 30.7% of the time (which translated to the success rate of 31.7% when each pipette was considered individually, similar to that reported for the autopatcher) in the visual and somatosensory cortices of anesthetized mice, but it could not obtain quadruple recordings. When used in awake, head-fixed, body-restrained mice, the multipatcher led to at least one successful whole-cell recording 55.7% of the time and dual or triple recordings 17.5% of the time (which translated to the success rate of 17.3% when each pipette was considered individually).

Another automated system was recently developed for blind patching in awake, head-fixed, behaving mice (Desai et al., 2015). This MATLAB-based system not only automates the key steps in blind patching, such as penetration of the dura, moving of the pipette tip to a targeted region, searching of a neuron, sealing, and break-in, but it also enables automatic positioning of patch pipettes into craniotomies before the start of the patching process, by integrating a camera and an image-processing algorithm. Using this system, successful whole-cell recordings could be typically obtained in 5 minutes, at a rate of 17% in awake, head-fixed mice running on a wheel. The recording quality, as assessed using series resistance, was comparable to that obtained by manual patching, and the recording duration was 8 minutes on average (Desai et al., 2015).

To improve the yield of automated patch clamp recordings deep in the brain (e.g., in the thalamus), a robotic system that adds automatic lateral pipette navigation to the autopatching algorithm was developed recently (Stoy et al., 2017). As the pipette penetrates the brain to reach a desired region/depth for patching, the system detects an obstruction (e.g., a blood vessel) by detecting an increase in the pipette tip resistance. Once an obstruction is encountered, the pipette tip is retracted parallel to the pipette axis and the pipette tip resistance is subsequently recorded to establish a baseline value. The pipette tip is then moved laterally, lowered back to the depth at which the obstruction was detected, and the pipette tip resistance is checked again to determine if the tip resistance is less than 200 kΩ above the baseline value (in which case, it is presumed that the tip has successfully circumvented the obstruction). If the pipette tip still shows a resistance increase above the threshold value, the steps described above are repeated until the resistance increase is below the threshold or the lateral excursion exceeds 50 μm. The system could be used to obtain whole-cell recordings from neurons in the thalamus, with access resistance, holding currents, and resting membrane potentials that were comparable to those from cortical neurons. The success rate for a whole-cell recording from a thalamic neuron was 10%, which was significantly higher than that obtained without using the automatic lateral pipette navigation for dodging obstruction (Stoy et al., 2017).

1.3.3. Automated image-guided patch clamp recordings in vivo

One of the first attempts at automating image-guided patching *in vivo* has resulted in a system called "smartACT" (smart, Adaptive Cell Targeting), which enables automatic positioning of a patch pipette close to a targeted cell (Long et al., 2015). In the initial stages of its workflow, in which the pipette tip is positioned above the brain surface, smartACT utilizes 3D volume rendering of a two-photon image stack to allow for the selection of the pipette tip and target cell locations by a user. Once the pipette tip is automatically moved into the brain and placed at a certain distance away from the target cell, the system acquires another image stack and performs image segmentation on it to achieve automatic detection of the pipette tip and the target cell. The detection of the pipette tip and target cell locations enables adaptive adjustments of the pipette trajectory, resulting in a more accurate positioning of the pipette tip near the target cell. A user is then responsible for making the final approach to the cell, establishing contact with the cell membrane, gigasealing, and rupturing the cell membrane for whole-cell recordings. Using smartACT, the pipette tip could be moved from outside the brain to near a target cell in a similar time as a human experimenter, and manual patching following this automated pipette positioning led to whole-cell recordings in the primary visual cortex of anesthetized mice, with patched neurons showing electrophysiological characteristics similar to those in literature (Long et al., 2015). Although this system facilitates positioning of a patch pipette near a visually identified neuron, with the final patching process left for a human experimenter to complete, it does not fully address the need for manual skill and experience to perform image-guided patching *in vivo*.

1.4. Gamma oscillations

Regular and synchronized activity of neurons in the brain gives rise to network oscillations in various brain regions, such as the olfactory bub, thalamus, hippocampus, and neocortex (Bartos et al., 2007; Palop et al., 2007). These network oscillations show a wide range of frequencies, from delta (0.5 – 3 Hz) and theta (3 – 8 Hz) frequencies to gamma (30 – 90 Hz) and ultrafast (90 – 200 Hz) frequencies (Bartos et al., 2007). Previous studies have shown that fast-spiking, parvalbumin (FS-PV) expressing interneurons are important for the generation of gamma oscillations (Bartos et al., 2007; Palop et al., 2007), and that these oscillations are related to higher order brain functions, such as attention, memory formation, and recall (Bartos et al., 2007; Palop et al., 2007).

1.4.1. Gamma oscillations in Alzheimer's disease

Disruptions in gamma oscillations have been observed in several brain disorders, including bipolar disorder (Başar, 2013), epilepsy (Herrmann and Demiralp, 2005), and schizophrenia (Spencer et al., 2003; Uhlhaas and Singer, 2010). In Alzheimer's disease (AD), which is the most common type of primary degenerative dementias (Herrmann and Demiralp, 2005), gamma activity has been shown to be disrupted compared to healthy controls. For example, a study on spontaneous gamma oscillations during an eyes-closed state showed that the synchronization in the gamma frequency range was lower in AD patients compared to controls (Stam et al., 2002). In addition to the decreased gamma frequency synchronization, gamma responses elicited by sensory or cognitive stimulations were also shown to have a significant delay compared to healthy controls (Başar et al., 2016).

Mouse models of AD, like human AD patients, show disrupted gamma oscillations in their brain. For example, human amyloid precursor protein (hAPP) transgenic mice, which have abnormally high Aβ levels in their brain (Verret et al., 2012), show reduced gamma activity as well as spontaneous epileptiform discharges during periods of reduced gamma oscillations (Verret et al., 2012). This potentially supports the observation that human AD patients have increased seizure activity compared to healthy individuals (Amatniek et al., 2006). These findings suggest that abnormal gamma oscillations may play a key role in the AD pathology.

1.4.2. Effect of gamma oscillations on pathology of Alzheimer's disease

Recently, it has been shown that gamma frequency entrainment with flickering lights (called gamma entrainment using sensory stimulus or GENUS) reduces amyloid load and modifies microglia, effectively reducing AD pathology in AD mouse models (Iaccarino et al., 2016). The study first demonstrated that, by driving FS-PV interneurons in hippocampal subregion CA1 at 40 Hz using optogenetic tools, amyloid-β (Aβ) accumulation was significantly reduced in the stimulated brain region in 5xFAD mice, a well-established AD mouse model. Interestingly, optogenetically driving other cell types at 40 Hz or driving FS-PV interneurons at frequencies other than 40 Hz did not result in the reduction of amyloid levels, suggesting that 40 Hz stimulation of FS-PV interneurons may be key for effective amelioration of AD pathology. Based on these findings, visual stimulation with LED lights flickering at 40 Hz, which was found to increase 40 Hz oscillations in the primary visual cortex of 5XFAD mice (Iaccarino et al., 2016), was explored to see if this non-invasive approach can also lead to a reduction of amyloid levels. Surprisingly, after exposing 5xFAD mice to flickering LED lights for 1 hour, Aβ levels were reduced by more than 50% in the visual cortex compared to 5xFAD mice exposed to a dark condition for 1 hour, and this reduction was specific to the 40 Hz flicker frequency (i.e., constant light, 20 Hz, 80 Hz, and random flicker frequency conditions did not show significant change from the dark condition). The hour-long stimulation also led to changes in microglia morphology – namely, enlarged cell body and reduced primary process lengths, both of which are related to enhanced engulfment activity (Wang et al., 2015b) – as well as to increased co-localization of the microglia cell body with Aβ, suggesting improved amyloid endocytosis by microglia (Iaccarino et al., 2016). In addition, a long-term (i.e., 1 hour per day for 7 consecutive days) exposure to the LED lights flickering at 40 Hz led to not only less number of amyloid plaques but also smaller plaque sizes in the primary visual cortex. Tau phosphorylation, which is another AD-related pathology (Šimić et al., 2016), was also significantly reduced in the visual cortex following the 7 days, 1 hour per day exposure to the 40 Hz flickering LED lights.

The discovery of the effect of visual GENUS was soon followed by yet another striking finding that gamma entrainment using auditory stimulation can also effectively attenuate AD-related pathology in AD model mice (Martorell et al., 2019). In this study, it was demonstrated that a train of auditory tones repeating at 40 Hz could increase 40 Hz oscillations, decrease amyloid load, induce microglial responses, and reduce tau phosphorylation in the primary sensory cortex (in this case, the auditory cortex), similar to the 40 Hz flickering light. Auditory GENUS also increased the number of reactive-like astrocytes, blood vessel diameter, and co-localization of Aβ with lipoprotein receptor-related protein (LRP1), all of which suggest an improved Aβ clearance through the vasculature (Martorell et al., 2019). Importantly, it was found that spatial and recognition memory was significantly improved in 5xFAD mice exposed

to 7 days of auditory GENUS (1 hour per day) compared to control mice (i.e., mice not exposed to auditory GENUS), showing for the first time that GENUS can positively impact cognitive function. Unlike visual GENUS, the effect of auditory GENUS reached brain regions beyond primary sensory areas, inducing periodic modulation of spiking activity, reduced amyloid load, glial changes, increased blood vessel diameter, and decreased tau phosphorylation in the hippocampus. Auditory GENUS could also modulate neural activity in the medial prefrontal cortex, but the amyloid load in this area was significantly reduced only when both visual and auditory stimulations were presented together for 7 consecutive days (1 hour per day). The effect of the combined stimulation was again frequency-specific, with frequencies other than 40 Hz failing to reduce amyloid levels in the brain of 5xFAD mice. Although these discoveries are promising, the effect of GENUS on the human brain, especially in terms of safety and feasibility of gamma entrainment using sensory stimuli, still needs to be studied to determine the possibility of translating the GENUS approach to people with AD.

1.5. Thesis outline

In Chapter 2 of this thesis, we present a closed-loop real-time imaging strategy that automatically compensates for cell movement by tracking cell position and adjusting pipette motion while approaching a target. We also describe the integration of this automatic pipette positioning with our earlier impedance-based cell detection strategy (Kodandaramaiah et al., 2012, 2016) in an algorithm and the development of a robotic system implementing this algorithm. We show that our system can patch fluorophore-expressing neurons of multiple types in the living mouse cortex, without human intervention, with yields comparable to skilled human experimenters. In Chapter 3, we use the original autopatcher to obtain patch clamp recordings from cortical and hippocampal neurons in the intact mouse brain undergoing temporally interfering electric fields-based non-invasive brain stimulation, demonstrating how an automated patch clamping system can facilitate the development and validation of a new tool in neuroscience. In Chapter 4, we describe a device that we developed for delivering 40 Hz light and sound stimulations at intensity levels tolerable to humans. We then demonstrate that sensory stimulations from our device could induce steady 40 Hz entrainment on cognitively normal subjects, with concurrent visual and auditory stimulation resulting in stronger and more widespread entrainment than visual or auditory stimulation alone. We also show that our stimulations did not lead to any adverse side effects in our human subjects, suggesting that GENUS can be a safe and effective way of inducing widespread 40 Hz entrainment, which may have therapeutic effects in people suffering from AD.

Chapter 2: Automated cell-targeted patch clamp neural recordings *in vivo*[1]

2.1. Introduction

Targeted patch clamp recording of visually identified neurons (Dittgen et al., 2004; Kitamura et al., 2008; Margrie et al., 2003) is a powerful technique for electrophysiological characterization of cells of a given class in the living mammalian brain, and is in increasing demand for its ability to link a cell's molecular and anatomical identity with its electrophysiological characteristics in the context of specific behaviors, states, and diseases (Chen et al., 2015; Li et al., 2015; Pala and Petersen, 2015; Runyan et al., 2010; van Welie et al., 2016). However, the manual labor and skill required to perform visually guided patching *in vivo* have limited widespread adoption of the technique. Previously, we discovered that non-image guided (i.e., 'blind') patching *in vivo* could be reduced to an algorithm, and we accordingly built a robot, which we called the "autopatcher", that automatically performs blind patch-clamp recordings of single neurons in the intact brain by detecting cells based on changes in pipette tip impedance (Kodandaramaiah et al., 2012, 2016). Since then, several attempts have been made to automate visually guided patch clamp recordings of targeted neurons. Although these attempts have enabled automatic positioning of a patch pipette near a visually identified neuron, all currently available systems either need a human to perform the final patching process itself (Long et al., 2015) or require human adjustment of the patching process for about half of the trials (Wu et al., 2016). We realized that a system that can achieve the whole-cell patch clamp configuration from a targeted cell without human intervention needs to address a key technical challenge: as a patch pipette moves towards a target cell for patch clamping, the cell moves as well, causing the pipette to miss its mark without manual adjustments of pipette motion that compensate for cell movement.

We therefore designed a new kind of algorithm, which we call "imagepatching", in which real-time imaging in a closed-loop fashion allows for continuous adaptation of the pipette trajectory in response to changes in cell position throughout the patching process. We constructed a simple robotic system and software suite implementing imagepatching that can operate on a conventional two-photon microscope with commercially available manipulators and amplifiers, and show that we can obtain *in vivo* patch clamp recordings from fluorescently labeled neurons, of multiple cell types, in the living mouse cortex without any human intervention, and with a quality and yield similar to or even exceeding that obtained by skilled human experimenters. Our imagepatching robot is easy to implement, and will help enable scalable electrophysiological characterization of identified cell types in intact neural circuits.

2.2. Closed-loop real-time imaging algorithm for compensation of target cell movement during image-guided patch clamping

In the anesthetized mouse cortex, we found that moving a patch pipette by 300 – 400 μm from above the brain surface into layer 2/3 along the axial direction (i.e., parallel to the pipette axis, 30° below the horizontal) resulted in a target cell displacement of 6.8 ± 5.1 μm (mean ±

[1] The contents of this chapter have been published in *Neuron* (https://doi.org/10.1016/j.neuron.2017.08.011).

standard deviation used throughout; n = 25 cells in 6 mice; Figure S2.1A) in the transverse plane. In addition, we observed that pipette navigations in the vicinity of a targeted cell (i.e., pipettes moving by ~5 – 10 μm when starting ~20 – 30 μm away from the cell) caused the targeted cell to move by 2.2 ± 1.4 μm (n = 27 cells in 17 mice; Figure S2.1B) in the transverse plane. These findings suggested that to correctly place the pipette tip on a targeted cell and patch it in a fully automated fashion, the displacement of the target cell resulting from pipette movement needs to be compensated for as the pipette is advanced towards the cell. Accordingly, we developed a closed-loop real-time image-guided algorithm that involves repeated target cell imaging followed by centroid detection (Figure 2.1A(i)) and pipette movement (Figure 2.1A(ii) and (iii)) stages, to continuously compensate for cell movement as the pipette approaches the target. We found that with the closed-loop algorithm supporting pipette navigation to a targeted cell, the entire image-guided patching process could be reduced to a six-stage "imagepatching" algorithm (Figure 2.1B; full flowchart in Figure S2.2). Imagepatching fuses closed-loop real-time image-guided pipette positioning with our earlier impedance-based cell detection strategy (Kodandaramaiah et al., 2012, 2016) to enable automated cell-attached or whole-cell patch clamp recording of visually identified cells in the intact mammalian brain.

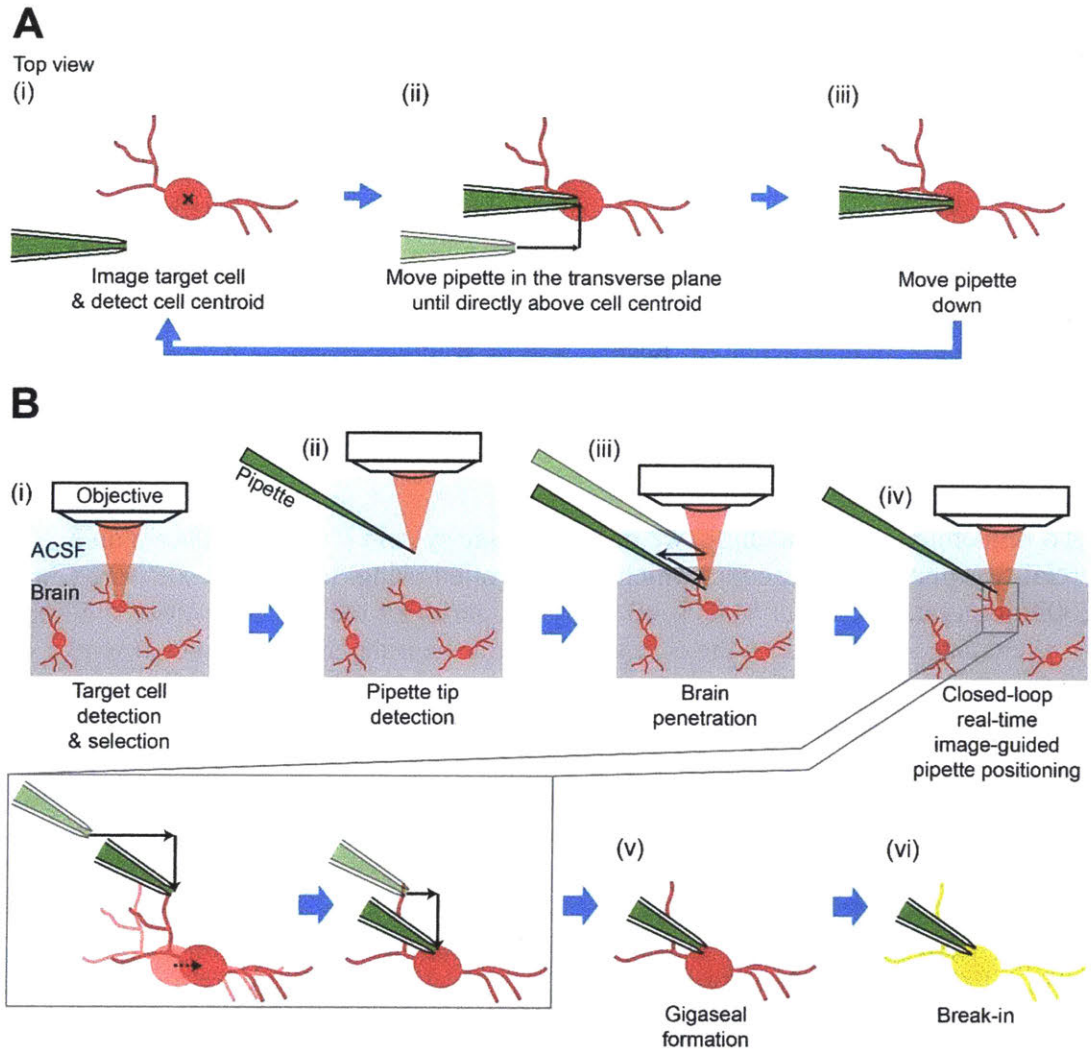
A
Top view
(i)
(ii)
(iii)
Image target cell
& detect cell centroid
Move pipette in the transverse plane
until directly above cell centroid
Move pipette
down
B
(i)
Objective
ACSF
Brain
(ii)
Pipette
(iii)
(iv)
Target cell
detection
& selection
Pipette tip
detection
Brain
penetration
Closed-loop
real-time
image-guided
pipette positioning
(v)
(vi)
Gigaseal
formation
Break-in
C
Computer
Ti-sapphire
laser
PMT2
Two-photon
microscope
Dichroic
PMT1
Dichroic
Digitizer
X-Y platform
& Z focus
motor
Autopatcher
control box
Switch
Amplifier
Headstage
Autopatcher
digital board
4-axis
manipulator
Fixation plate
High positive pressure
Low positive pressure
Atmospheric pressure
Suction pressure
Valves

Figure 2.1. Imagepatching: closed-loop real-time image-guided patch clamping *in vivo*.
(A) The closed-loop algorithm for continuous cell centroid localization and pipette position adjustment while approaching the targeted cell (for step-by-step flowchart, see Figure S2.2). Green, patch pipette filled with fluorescent dye; red, fluorescent cell targeted for patching; black x, target cell centroid; black arrows, pipette movement.
(B) The six stages of the image-guided automated patching algorithm (for step-by-step flowchart, see Figure S2.2). ACSF, artificial cerebrospinal fluid; red, fluorescent cells; green, patch pipette filled with fluorescent dye; light red, laser for two-photon imaging; black solid arrows, pipette movements; black dotted arrow, cell movement; yellow, target cell filled with the fluorescent dye from the pipette.
(C) Schematic of the imagepatcher hardware, composed of a conventional two-photon image-guided patch clamp rig and our previously developed autopatcher control box (Kodandaramaiah et al., 2012, 2016). Arrows indicate the direction of information flow. PMT, photomultiplier tube.

To implement imagepatching, we built a robotic system ("imagepatcher") on a commercial two-photon microscope, which we controlled using ScanImage software (Pologruto et al., 2003) integrated with our MATLAB code that performs the real-time closed-loop image analysis. We chose ScanImage as the core software for the imagepatcher, since it works with two-photon systems from multiple vendors, and because its open code allowed us to incorporate real-time analysis of ScanImage-acquired images. The imagepatcher hardware shown in Figure 2.1C was assembled by augmenting a conventional two-photon image-guided patch clamp rig with an autopatcher control box (Kodandaramaiah et al., 2012, 2016) that was modified to provide a wide range of pressure values (see Methods for details of this, as well as other technical implementation points summarized in the following section). We validated the imagepatcher by using it to obtain targeted *in vivo* recordings from tdTomato-expressing cells in somatosensory and motor cortices of anesthetized Cre-dependent reporter mice, namely parvalbumin (PV)-positive interneurons in PV-Cre x Ai14 mice and calcium/calmodulin-dependent protein kinase II isoform alpha (CaMKIIα)-positive pyramidal neurons in CaMKIIα-Cre x Ai14 mice (Clarke, 1993; Hippenmeyer et al., 2005; Tsien et al., 1996). PV-positive and CaMKIIα-positive cells had different cortical densities (9.6 ± 6.3 tdTomato-expressing cells per volume of 200 × 200 × 100 μm^3 in 9 PV-Cre x Ai14 mice vs 47.0 ± 31.8 tdTomato-expressing cells in this volume in 7 CaMKIIα-Cre x Ai14 mice) and morphologies (example two-photon images of tdTomato-expressing cells in layer 2/3 somatosensory cortex of each mouse line are shown in Figures 2.4A and 2.4B), and thus allowed us to explore the degree of generality that the imagepatcher offers to an end user.

2.3. Imagepatcher operation

The imagepatcher starts by executing a target cell detection stage (Figure 2.1B(i)), in which two-photon images of the mouse brain are acquired and then analyzed to identify fluorescent cells. From these candidate cells, the end user can select a neuron of interest using the imagepatcher's graphical user interface (see Appendix A: Imagepatcher user manual for details). The imagepatcher then moves on to the pipette tip detection stage (Figure 2.1B(ii)), where a dye (e.g., Alexa 488)-filled patch pipette is brought into the field-of-view above the brain, and the tip of the patch pipette is automatically located. The pipette tip is identified using a

pipette tip detection algorithm (Figure 2.2A) derived from our finding that the cluster of bright pixels in the pipette image (Figure 2.2A(ii), area bounded by yellow outline), which represents the fluorescence from the dye inside the pipette, robustly changes its position as the focal plane of the microscope objective is moved downward from above the pipette tip. Accordingly, we developed a pipette tip detection algorithm to acquire a z-stack around the pipette tip (Figure 2.2A(i)) and to identify the image in the stack capturing the cluster of bright pixels that is furthest away from the far end of the pipette (represented by the centroid of the cluster in the topmost image in the stack; Figure 2.2A(ii.i), black x), assigning the z-coordinate of this farthest-cluster image as the z-coordinate of the pipette (Figure 2.2A(iii), $z_{pipette}$). The portion of the pipette tip detection algorithm responsible for the identification of the pipette tip in the image at $z_{pipette}$ (Figure 2.2A(iv)) was developed based on the fact that an image focused on the pipette tip shows a triangular object corresponding to the pipette shank converging to a point (i.e., the pipette tip). We therefore designed the pipette tip detection algorithm to find the cluster of bright pixels that captures three vertices of the pipette from the image at $z_{pipette}$ (Figure S2.3A(ii.ii)), which is then analyzed to identify the pixel corresponding to the pipette tip (Figure S2.3A(iii)). When tested on 16 z-stacks (2 μm step size, 20 images, 17x zoom), each of which captured the tip of a separate Alexa 488-filled patch pipette (angled at 30° below the horizontal) at a distinct position within the stack, the pipette tip detection algorithm was capable of accurately extracting the pipette tip, with the tip location determined by the algorithm deviating from the visually assessed tip position by -1.0 ± 0.8 μm, -0.2 ± 0.4 μm, and 1.0 ± 2.4 μm in the x, y, and z directions respectively. The algorithm's performance was similar for patch pipettes at different angles below the horizontal (see Methods, "Performance of the pipette tip detection algorithm at angles other than 30° below the horizontal" for details).

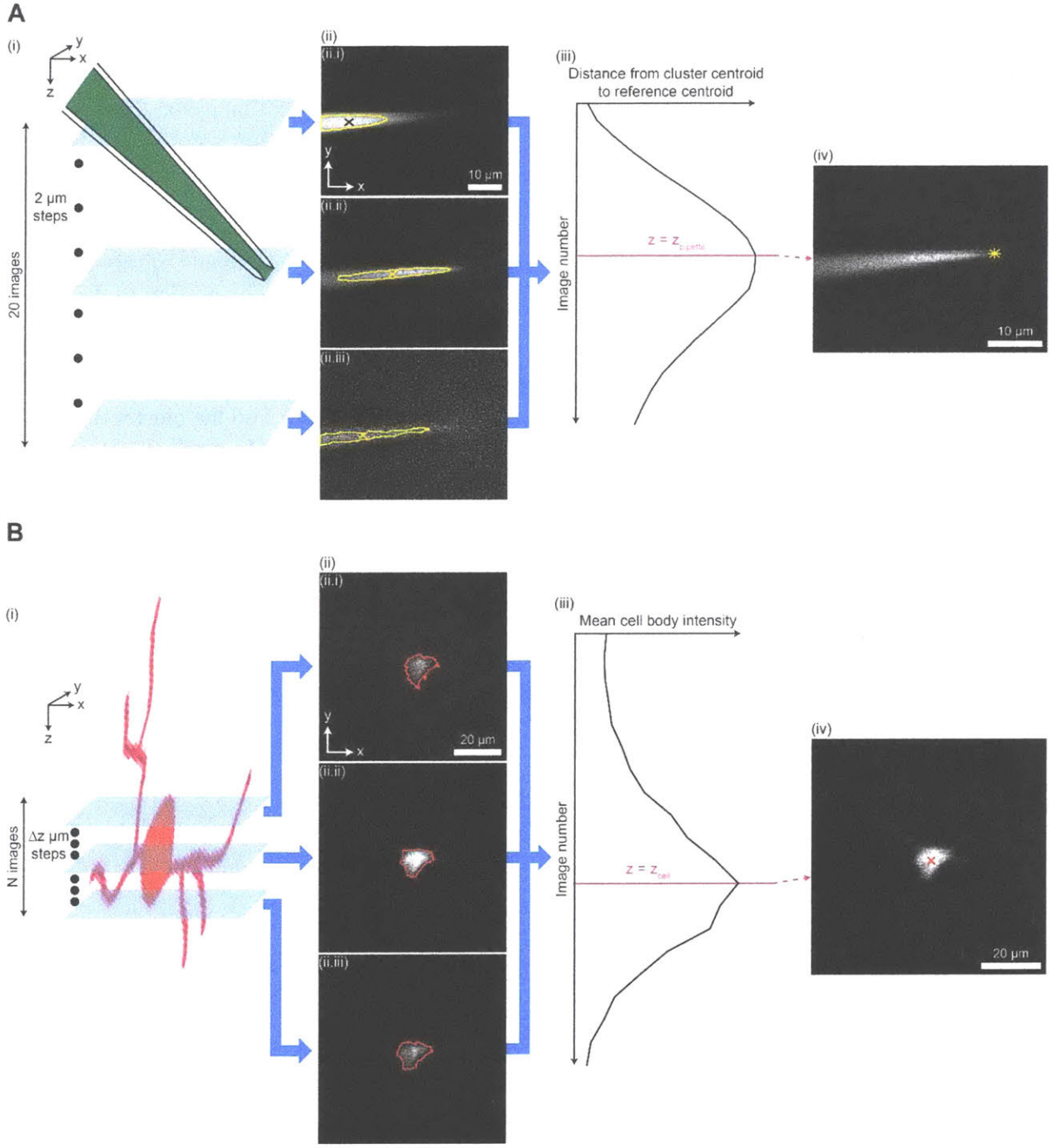

Figure 2.2. Key algorithms for closed-loop real-time image analysis.
(A) Steps of the pipette tip detection algorithm. (i) A z-stack with 20 images and 2 µm step between consecutive images is acquired around a pipette filled with a dye (e.g., Alexa 488, green). (ii) Each image in the z-stack is analyzed to identify the cluster of bright pixels (area bounded by yellow outline, corresponding to the fluorescence from Alexa 488 inside the pipette) and the centroid of the cluster (x). The centroid in the topmost image of the z-stack ((ii.i), black x) is used as a reference location corresponding to the far end (i.e., end opposite to the pipette tip) of the pipette. Images 1 (ii.i), 10 (ii.ii), and 20 (ii.iii) of the z-stack, numbered from top to bottom, are shown as examples. (iii) The distance between the cluster centroid (x in (ii)) and the

reference centroid (black x in (ii.i)) is calculated for each image in the z-stack. The image at which this distance is the largest is identified as the image focused on the pipette tip (magenta line). The z-coordinate of the focused image corresponds to that of the pipette tip ($z_{pipette}$). (iv) The image focused on the pipette tip is analyzed to yield the location of the pipette tip in the transverse plane (yellow star). For image analysis steps used to locate the pipette tip in the transverse plane, see Figure S2.3A.
(B) Steps of the cell position detection algorithm. (i) A z-stack is acquired around a tdTomato-expressing cell (red), with N images and Δz step between consecutive images (N = 24, Δz = 3 μm for cell position detection in the brain penetration stage; N = 10, Δz = 2 μm for cell position detection in the closed-loop real-time image-guided pipette positioning stage). (ii) Each image in the z-stack is analyzed to detect the boundary of the cell body (red outline). Images 8 (ii.i), 12 (ii.ii), and 16 (ii.iii) of the z-stack, numbered from top to bottom, are shown as examples. (iii) The mean intensity of pixels representing the cell body (i.e., pixels surrounded by the detected boundary in (ii)) is calculated for each image in the z-stack. The image at which this mean intensity is the highest is identified as the image focused on the centroid of the cell body (magenta line). The z-coordinate of the focused image corresponds to that of the cell centroid (z_{cell}). (iv) The image corresponding to the z-coordinate of the cell centroid is analyzed to yield the centroid position in the transverse plane (red x). For image analysis steps used to detect the boundary and the centroid of the cell body, see Figure S2.3B.

The pipette tip location determined during the pipette tip detection stage is used by the imagepatcher to compute the ideal trajectory to the target cell at the start of the brain penetration stage (Figure 2.1B(iii)), and also to calculate the pipette tip position in subsequent stages of imagepatching; we decided not to utilize the pipette tip detection algorithm (Figure 2.2A) to locate the pipette tip from the brain penetration stage onward, because a pipette that entered the brain without contamination ejected a plume of fluorescent dye that obscured the exact location of the pipette tip, which made it difficult to robustly resolve the pipette tip using an image-based algorithm. To enter the brain, the imagepatcher applies high positive pressure (600 mBar) to the pipette and moves it along the calculated trajectory at about 600 μm/s (i.e., at the maximum speed that our 4-axis micromanipulator can generate under software control; the same speed is used to move the pipette throughout the imagepatcher operation) until the pipette tip is within 75 μm from the initial target cell location. At this point, the pipette pressure is quickly reduced to 300 mBar to prevent excessive background fluorescence, but if little or no dye is ejected around the pipette tip, or a drastic resistance increase is observed, the pipette is deemed contaminated and brief pulses of positive pressure (>300 mBar) are applied to clean the pipette tip (as described in Komai et al., 2006). The pressure value of the pulse is increased until the pipette tip is cleared, but no more than 800 mBar is applied as a pipette ejecting the dye at this high pressure can cause excessive background fluorescence that interferes with cell detection in subsequent steps of imagepatcher operation. If the clogged state persists even after two pulses of high positive pressure, the contaminated pipette is automatically retracted. The imagepatcher applies a pipette pressure of 300 mBar while moving the clean pipette to the vicinity of the target, as we found this pressure value to be high enough to keep the pipette tip clean inside the brain, but not so high as to cause a lingering flood of dye that would lead to excessive background fluorescence (see Methods, "Derivation of pipette pressure for brain entry and cell approach" for details).

Once the pipette tip is within 50 μm from the target cell's initial location, the imagepatcher re-images and re-detects the target cell to account for cell movement resulting from pipette entry into the brain, using the cell position detection algorithm described in Figure 2.2B. The algorithm was derived based on the fact that in fluorescence microscopy, a fluorescent object looks the brightest when it is in focus (i.e., an image of a fluorescently labeled cell captures pixels corresponding to the fluorescence of the cell, and these pixels have higher intensities in an image focused on the cell compared to out-of-focus images). We thus built the cell position detection algorithm to detect the cell body in each image of a z-stack of the target cell (Figure 2.2B(ii)) and then to identify the image with the highest mean pixel intensity within the cell body (Figure 2.2B(iii), magenta line), which yields the z-coordinate of the target cell (Figure 2.2B(iii), z_{cell}). We also designed the cell position detection algorithm to identify the centroid (i.e., center of mass) of the cell body in the image at z_{cell} (Figure 2.2B(iv), red x), which is then assigned as the cell position in the transverse plane, because the cell body centroid is where investigators manually performing image-guided patching would aim with the tip of a patch pipette (Häusser and Margrie, 2014; Komai et al., 2006). When tested on 21 z-stacks (2 or 3 μm step size, 20 or 24 images, 17x zoom; from 5 mice), each capturing a PV-positive neuron at a different position within the cortex, the cell position detection algorithm correctly yielded x, y, and z coordinates of the cell centroid in all 21 stacks (visually assessed). Following cell position detection, the pipette is moved so that its tip is 25 μm above the updated target cell centroid, and the pipette tip is checked again for contamination.

With the clean pipette in place, the closed-loop real-time image-guided pipette positioning stage (Figure 2.1B(iv)) begins by lowering the pipette pressure (to 100 mBar) to prevent the target cell from being blown out of place and by performing another cell position detection (as in Figure 2.2B) to update the location of the target cell. The imagepatcher then repeatedly finds the target cell centroid (Figures 2.1A(i) and 2.2B(iv)) and repositions the pipette in the transverse plane according to the offset from the pipette tip to the cell centroid (Figure 2.1A(ii)) before each downward 3 μm z-step towards the target cell (Figure 2.1A(iii); example data from multiple steps of this closed-loop operation in Figures 2.3A and 2.3B, with corresponding imagepatching impedance trajectory in Figure 2.3C). Similar to manual image-guided patching *in vivo* (Häusser and Margrie, 2014; Komai et al., 2006; Margrie et al., 2003), both visual (pipette tip within the boundary of the target cell soma; Figure 2.3A(iii)) and electrical (resistance increase that exceeds a certain threshold; Figure 2.3C(iii)) parameters are repeatedly checked while the pipette advances towards the target cell to determine when the pipette tip touches the target cell membrane. The imagepatcher maintains the pipette pressure at 100 mBar until the pipette tip makes contact with the cell membrane, because we found that this pressure helped prevent pipette tip clogging and allowed a detectable change in pipette resistance to be observed when the pipette tip touched the cell membrane (as in Figure 2.3C(iii)) while not blowing the target cell out of place and not resulting in excessive background fluorescence (see Methods, "Derivation of pipette pressure for brain entry and cell approach" and "Optimization of cell-pipette contact detection, gigaseal formation, and break-in" for details). Once the pipette tip makes contact with the cell membrane, the imagepatcher dynamically changes the pipette pressure from 100 mBar to 30 mBar to prepare for gigaseal formation. We found that this lowering of pressure resulted in reduction of, and fluctuation of, the amplitude of current pulses that were observed in response to the application of voltage steps to the pipette tip, corresponding to the heartbeat modulation that has been reported previously (Häusser and

Margrie, 2014; Komai et al., 2006; Margrie et al., 2003). We also found that the amount of amplitude reduction, which we computed by comparing the pipette resistance before and after the pressure change, and the amount of amplitude fluctuation, which we quantified by calculating the standard deviation of the amplitude of current pulses, were useful predictors of gigaseal formation when they each exceeded a certain threshold (see Methods, "Optimization of cell-pipette contact detection, gigaseal formation, and break-in" for details). The imagepatcher therefore checks if resistance change and the standard deviation of the current pulse amplitude following the lowering of pipette pressure to 30 mBar are high enough before advancing to the gigaseal formation stage (Figure 2.1B(v)).

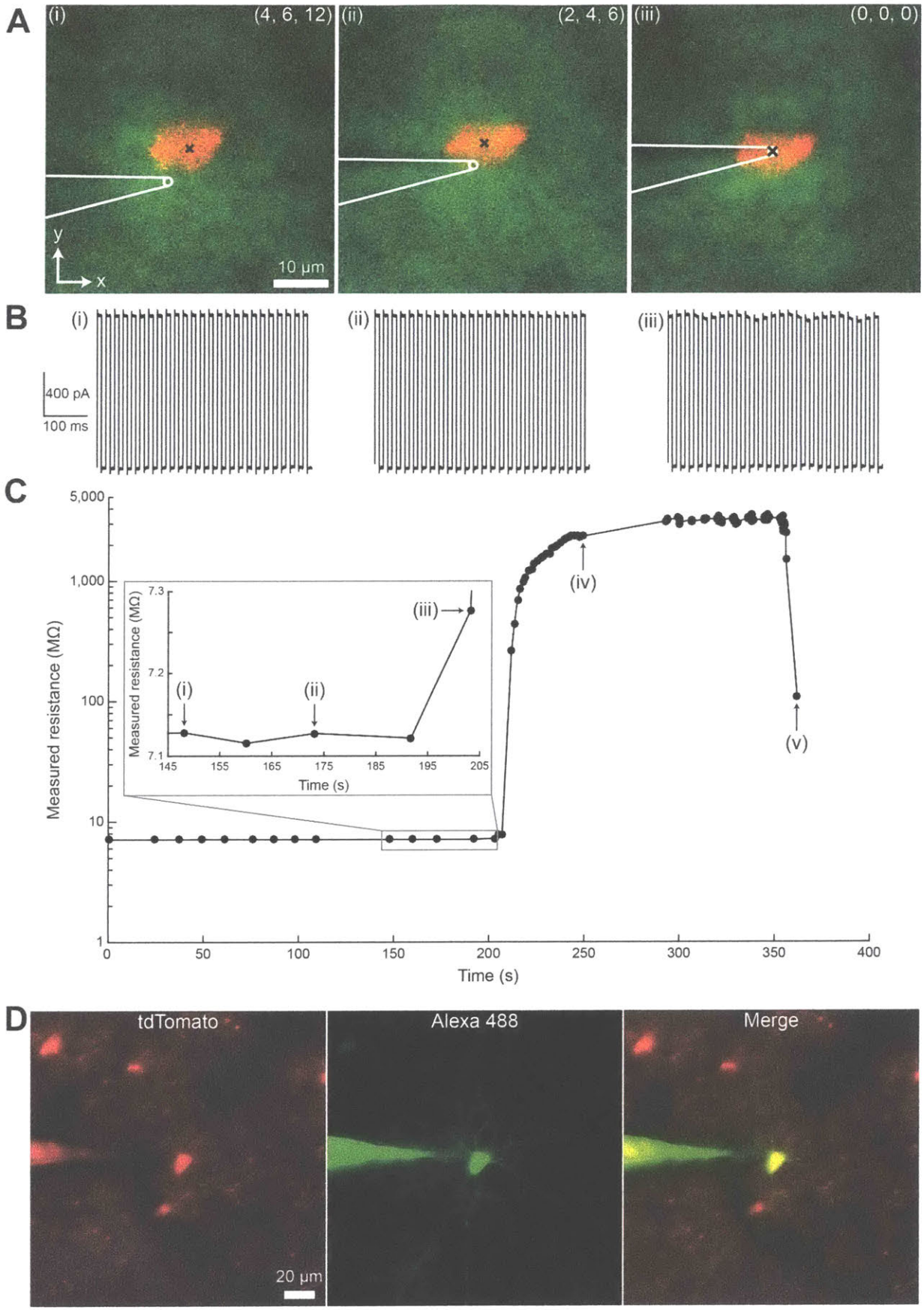
A
(i)
(4, 6, 12)
(ii)
(2, 4, 6)
(iii)
(0, 0, 0)
y
x
10 µm
B
(i)
(ii)
(iii)
400 pA
100 ms
C
Measured resistance (MΩ)
Time (s)
(i)
(ii)
(iii)
(iv)
(v)
D
tdTomato
Alexa 488
Merge
20 µm

Figure 2.3. Imagepatcher operation.
(A) Two-photon images of a parvalbumin (PV)-positive neuron acquired at three different time points (indicated by Roman numerals for reference in (B) and (C)) during closed-loop real-time image-guided pipette positioning. White, sketch of pipette tip; green, Alexa 488; red, tdTomato; x, target cell centroid; numbers in the upper right, vector (x, y, z) from the pipette tip to the target cell centroid (in μm).
(B) Pipette current traces in response to 10 mV voltage pulses, with Roman numerals indicating the corresponding images in (A).
(C) Pipette resistance during imagepatching over time, with Roman numerals corresponding to time points referenced in (A) and (B): (i) pipette is 12 μm above the target cell centroid; (ii) pipette is 6 μm above the centroid; (iii) pipette is 0 μm above the centroid (i.e., in contact with the cell); (iv) gigaohm seal is established; (v) cell is broken-into.
(D) Maximum intensity projection (MIP) of a z-stack (48 images, 2 μm step size) of an imagepatched PV-positive neuron, showing tdTomato (left, red), Alexa 488 (middle, green) and overlay (right).

During gigaseal formation, the positive pressure is removed and 20 mBar suction is applied while hyperpolarizing the pipette. When a gigaohm seal is established (Figure 2.3C(iv)), the imagepatcher operation may be halted to obtain cell-attached extracellular recordings. For whole-cell mode, the imagepatcher advances to the break-in stage (Figure 2.1B(vi)), in which increasing pulses of suction (starting at 25 mBar and increased up to 350 mBar) are applied to achieve the whole-cell configuration (Figure 2.3C(v)). As done at the completion of manual image-guided patching *in vivo* (Häusser and Margrie, 2014; Komai et al., 2006; Margrie et al., 2003), the imagepatcher checks if the dye from the pipette is filling the target cell, by first acquiring a z-stack around the target cell, then identifying pixels corresponding to the cell body (as in Figure 2.2B(ii)), and finally calculating the mean pixel intensity of the cell body in the microscope channel corresponding to the pipette dye, to verify successful break-in (example of a dye-filled cell at the end of successful imagepatching is shown in Figure 2.3D).

2.4. Imagepatcher performance

Using the imagepatcher, stable cell-attached extracellular and whole-cell intracellular recordings could be obtained from PV-positive neurons (example recordings in Figures 2.4C and 2.4E) and CaMKIIα-positive neurons (example recordings in Figures 2.4D and 2.4F) in layer 2/3 of somatosensory and motor cortices of anesthetized mice, enabling *in vivo* observations of supra- and subthreshold activities of these cells. Access resistance, resting potential, and holding current (Figures 2.4G-2.4I) of imagepatched cells (n = 24 PV-positive neurons from 14 PV-Cre x Ai14 mice and 13 CaMKIIα-positive neurons from 7 CaMKIIα-Cre x Ai14 mice) were comparable to those reported by previous studies involving two-photon image-guided patching of cortical neurons *in vivo* (Atallah et al., 2012; Gentet et al., 2010, 2012; Mateo et al., 2011; Pala and Petersen, 2015), and were not significantly different from the cells that we manually patched (n = 11 PV-positive neurons from 8 PV-Cre x Ai14 mice; Figures S2.4A-S2.4C; P = 0.49 for access resistance, P = 0.08 for resting potential, P = 0.19 for holding current when comparing imagepatched and manually patched PV-positive cells; two-sided Student's t-test with 95% confidence level, assuming unknown and unequal variances). Other properties of imagepatched neurons, such as input resistance and spontaneous firing rate (Figures S2.4D and

S2.4E; n = 9 PV-positive neurons from 5 PV-Cre x Ai14 mice and 13 CaMKIIα-positive neurons from 7 CaMKIIα-Cre x Ai14 mice), also showed distributions of values that overlapped with those obtained in previous *in vivo* studies of cortical neurons (Mateo et al., 2011; Pala and Petersen, 2015).

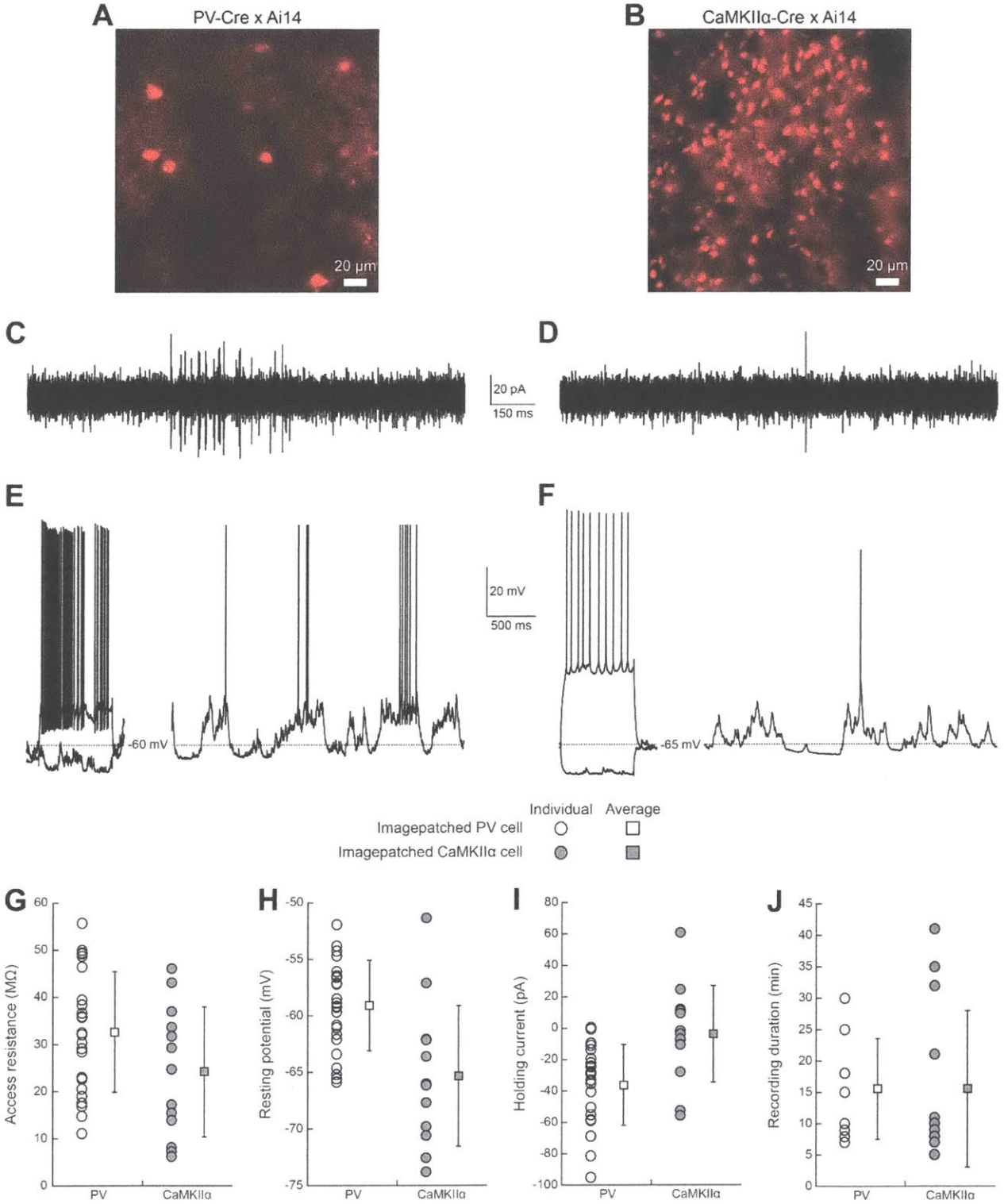

Figure 2.4. Imagepatching of multiple cell types in mouse cortex.
(A) Maximum intensity projection of a z-stack (20 images, 5 μm step size) of tdTomato (red)-expressing PV-positive cells in layer 2/3 somatosensory cortex of a PV-Cre x Ai14 mouse.
(B) Maximum intensity projection of a z-stack (20 images, 5 μm step size) of tdTomato (red)-expressing CaMKIIα-positive cells in layer 2/3 somatosensory cortex of a CaMKIIα-Cre x Ai14 mouse.
(C) Cell-attached current recording from an imagepatched PV-positive neuron.
(D) Cell-attached current recording from an imagepatched CaMKIIα-positive neuron.
(E) Whole-cell voltage recordings from an imagepatched PV-positive neuron under current injection (left, −100 and +200 pA), and at rest (right).
(F) Whole-cell voltage recordings from an imagepatched CaMKIIα-positive neuron under current injection (left, −100 and +200 pA), and at rest (right).
(G-J) Recording quality of imagepatched PV-positive neurons (white symbols; n = 24 cells from 14 PV-Cre x Ai14 mice for G-I; n = 9 cells from 5 PV-Cre x Ai14 mice for J) and imagepatched CaMKIIα-positive neurons (gray symbols; n = 13 cells from 7 CaMKIIα-Cre x Ai14 mice) in somatosensory and motor cortices of isoflurane-anesthetized mice. Square and error bars are mean ± standard deviation.
(G) Access resistance.
(H) Resting potential.
(I) Holding current.
(J) Recording duration.

The imagepatcher obtained targeted patch clamp recordings in 10 ± 3 minutes from the brain penetration stage onwards (n = 24 PV-positive neurons from 14 PV-Cre x Ai14 mice and 13 CaMKIIα-positive neurons from 7 CaMKIIα-Cre x Ai14 mice; each of the two preceding stages of the algorithm takes around one to two minutes extra), with the recordings lasting for 7 – 30 minutes for PV-positive neurons (n = 9 cells, 5 PV-Cre x Ai14 mice; Figure 2.4J) and 5 – 41 minutes for CaMKIIα-positive neurons (n = 13 cells, 7 CaMKIIα-Cre x Ai14 mice; Figure 2.4J). When targeting PV-positive cells, the gigaohm seal was obtained 42 times out of 108 attempts, and 24 of the 42 gigaohm seals successfully led to the whole-cell configuration (from 17 PV-Cre x Ai14 mice, of which 16 yielded one or more gigaohm seals and 14 yielded one or more whole-cell configurations). For CaMKIIα-positive cells, from 65 trials, the gigaohm seal was achieved 19 times, out of which the whole-cell configuration was achieved 13 times (from 10 CaMKIIα-Cre x Ai14 mice, of which 10 yielded one or more gigaohm seals and 7 yielded one or more whole-cell configurations). These success rates (for PV-positive neurons, 38.9% for obtaining gigaohm seals, and 22.2% for the whole-cell configuration; for CaMKIIα-positive neurons, 29.2% for obtaining gigaohm seals, and 20.0% for the whole-cell configuration) are comparable to or higher than that obtained by manually performing two-photon image-guided patching of fluorescently labeled neurons *in vivo* (for us, 10.6% success rate for manual whole-cell patching of tdTomato-expressing PV-positive neurons; n = 11 out of 104 attempts, 19 PV-Cre x Ai14 mice; a 10 – 20% success rate for obtaining a whole-cell recording from an EGFP-labeled PV-positive neuron was reported in Margrie et al., 2003). During our imagepatching experiments, some pipettes were occluded after brain penetration (n = 22 out of 108 when targeting PV-positive neurons; 14 out of 65 when targeting CaMKIIα-positive neurons; detailed breakdown of unsuccessful patching attempts in Table S2.1), and were automatically retracted by the imagepatcher; focusing on trials that entered the closed-loop stage (Figure 2.1B(iv)), the rates of

successfully achieving the gigaohm seal and the whole-cell configuration were 48.8% and 27.9% respectively (n = 42 gigaohm seals and 24 whole-cell configurations out of 86 trials) for PV-positive neurons, and 37.3% and 25.5% respectively (n = 19 gigaohm seals and 13 whole-cell configurations out of 51 trials) for CaMKIIα-positive neurons. These success rates did not vary substantially with target cell depth (Table S2.2) nor with the density of labeled cells around a target cell (Table S2.3), suggesting that the imagepatcher performance was consistent.

2.5. Discussion

We developed an algorithm and a robotic system that fully automates targeted patch clamping of visually identified cells *in vivo*, by implementing closed-loop real-time imaging to dynamically adjust the pipette position to hone in on a cell of interest. Our strategy makes the imagepatcher the first system that enables fully hands-free navigation of a patch pipette to a targeted cell and subsequent automated patch clamping in the intact brain. Unlike other previous systems that heavily rely on human intervention for successful patch clamp recordings of visually identified cells (Long et al., 2015; Perin and Markram, 2013; Steinmeyer and Yanik, 2012; Wu et al., 2016), the imagepatcher eliminates the need for manual adjustments and corrections during the entire patching process, making the robot a powerful tool that can facilitate systematic electrophysiological characterizations of specific classes of cells. Certain factors that can prevent investigators performing manual patching from achieving the whole-cell patch clamp state, such as variations in pipette trajectory, pipette movement speed, and pipette pressure levels, are also reduced in our automated system. The reduction of variation in these factors provides consistency in patch clamping procedures that may be difficult to obtain manually and may prove particularly beneficial for studies targeting very sparse populations of cells.

With our software designed to work in parallel with ScanImage operation, and our hardware designed to augment a conventional two-photon microscope in a modular way, the imagepatcher may be adapted to work on any microscope that ScanImage (or another openly modifiable software package) supports. Although our current study focused on targeted patching guided by two-photon microscopy in the intact brain, the imagepatcher could, in principle, also be used to automate and enable experiments utilizing other imaging modalities (e.g., one-photon fluorescence microscopy) and/or other tissues or preparations – as long as a target provides fluorescence corresponding to its size and position. In case of experiments involving targeted patching of non-fluorescent, unlabeled cells (i.e., "shadowpatching" developed by Kitamura et al., 2008), the cell position detection algorithm (Figure 2.2B), as it currently stands, may lead to incorrect identification of the target cell's z-coordinate, because we found from our shadow images that the mean pixel intensity of the cell body shadow does not vary with a defined pattern as a function of microscope focus (unlike cells labeled with a photostable fluorescent marker, which look the brightest when in focus). A new cell position detection algorithm that identifies the z-coordinate of a target cell based on its other properties (e.g., cell body size, cell body shape) might permit, in the future, automation of shadowpatching. The open nature of the imagepatcher code allows for integration of such an algorithm, in addition to tuning of software settings that might be required for different microscopes and imaging conditions.

Integrating our robot with patch pipette cleaning protocols for repeated patch pipette use (Kolb et al., 2016) may enable the elimination of some of the manual preparatory steps required to utilize imagepatching (e.g., filling a patch pipette with intracellular solution and inserting it into a pipette holder). By developing and using a bright pipette dye that has a fluorescence emission spectrum overlapping minimally (or ideally, not overlapping at all) with that of the target cells' fluorescent marker, the high level of background fluorescence that results from multiple penetrations into the brain may have little or no effect on cell position detection and targeting by the imagepatcher, enabling many imagepatching trials and thus patch clamp recordings per animal. Further augmentation of the imagepatcher hardware (i.e., integration of multiple autopatcher control boxes, each linked to an individual pipette, with a single two-photon microscope) and refinement of the software (e.g., code development for simultaneous micromanipulator control in response to multiple pipette impedances and imaged positions of target neurons) may also enable multi-cell targeted patch clamp recordings *in vivo* (Jouhanneau et al., 2015; Pala and Petersen, 2015; van Welie et al., 2016), which will provide information on how cells communicate with each other in an intact brain network. Although we have not obtained patch clamp recordings in the awake brain using the imagepatcher, with an appropriate restraint habituation strategy (to reduce brain motion), a robust image analysis approach (which compensates for large motion artifacts), or a real-time target cell switching (which enables targeting of an alternative cell, if present, when motion artifacts are large enough to displace the originally targeted cell out of the field-of-view), the imagepatcher may enable patch clamping of targeted neurons in awake animals.

2.6. Methods

2.6.1. Experimental model and subject details

All experimental procedures were performed on 6 – 8 week old transgenic mice, male and female used equally, of PV-Cre (Jax strain #: 017320) x Ai14 (tdTomato; Jax strain #: 007914) genotype or CaMKIIα-Cre (Jax strain #: 005359) x Ai14 (tdTomato; Jax strain #: 007914) genotype, in accordance with protocols approved by the Massachusetts Institute of Technology (MIT) Committee on Animal Care (CAC). Six PV-Cre x Ai14 mice were used to quantify neuron movements in response to a pipette entering the brain (Figure S2.1A), and seventeen additional PV-Cre x Ai14 mice were used to measure how much neurons change their locations when a pipette is navigated towards them inside the brain (Figure S2.1B). Eight PV-Cre x Ai14 mice were used to find the set of optimal pipette pressure levels for brain entry and cell approach during patching (Methods, "Derivation of pipette pressure for brain entry and cell approach"). Z-stacks of tdTomato-labeled parvalbumin (PV)-positive neurons, which were used to validate our cell detection algorithm (Figure 2.2B), were obtained from somatosensory and motor cortices of five PV-Cre x Ai14 mice. We used twenty PV-Cre x Ai14 mice to optimize the portion of the closed-loop image-guided pipette positioning stage responsible for resistance-based detection of the pipette tip-cell membrane contact, as well as the gigaseal formation and the break-in stages (Methods, "Optimization of cell-pipette contact detection, gigaseal formation, and break-in"). Three PV-Cre x Ai14 mice were used to derive the dye-based pipette blockage test (Methods, "Derivation of dye-ejection based pipette blockage test"). For comparing the cortical density of calcium/calmodulin-dependent protein kinase II alpha (CaMKIIα)-positive neurons to that of PV-positive neurons, z-stacks of tdTomato-expressing cells were obtained

from somatosensory and motor cortices of seven CaMKIIα-Cre x Ai14 mice and nine PV-Cre x Ai14 mice. To validate the robotic system running the imagepatching algorithm (Figure 2.4), seventeen PV-Cre x Ai14 mice and ten CaMKIIα-Cre x Ai14 mice were used, while nineteen PV-Cre x Ai14 mice were used for the manual patching experiments (Figures S2.4A-S2.4C).

2.6.2. Method details

Surgical procedures

Throughout the surgery, mice were anesthetized with 1 – 2% (vol/vol) isoflurane in oxygen and maintained at 37°C using a heating pad. After shaving the scalp, the mouse was placed in a custom-built stereotax, with its eyes covered with ophthalmic ointment. Betadine and 70% ethanol were then applied to the shave area for sterilization. A polycarbonate recording chamber was implanted on the skull using dental acrylic, and a 1 – 2 mm diameter craniotomy, contained inside a 3 mm diameter window of the recording chamber, was made 1.5 – 2 mm posterior to the bregma and 1.5 – 2 mm to the right of the midline. The dura was then carefully removed to expose the brain surface. Right before starting an imaging or a patch clamp experiment, 1.5% (vol/w) agar in HEPES buffered artificial cerebrospinal fluid (ACSF, containing 145 mM NaCl, 5.4 mM KCl, 10 mM HEPES, 1.8 mM $CaCl_2$, 1 mM $MgCl_2$ (Chen et al., 2015) or 150 mM NaCl, 2.5 mM KCl, 10 mM HEPES, 2 mM $CaCl_2$ and 1 mM $MgCl_2$ (van Welie et al., 2016); pH adjusted to 7.3 – 7.4 with NaOH) was applied on top of the brain to dampen pulsations caused by respiration and heartbeat, and then the craniotomy was covered with ACSF to keep the brain moist throughout the experiment. We took extra care to minimize bleeding throughout the surgery as blood on the cortical surface can greatly diminish optical clarity during two-photon imaging (Komai et al., 2006). In case of bleeding, the brain surface was irrigated with ACSF to stop the bleeding and remove as much blood as possible from the cortical surface. At the end of the experiment, mice were euthanized under anesthesia.

Electrophysiology

Cell-attached and whole-cell patch clamp recordings were performed on mice under 1 – 1.5% isoflurane anesthesia on a 37°C heating pad (DC Temperature Control System, FHC). Patch pipettes with resistance values between 5 – 7.5 MΩ were prepared by pulling filamented borosilicate glass capillaries (Warner or WPI) using a micropipette puller (Flaming-Brown P97 model, Sutter Instruments or PC-10 vertical puller, Narishige). These pipettes were filled with an internal solution containing (in mM): 135 K-gluconate, 4 KCl, 10 HEPES, 10 Na_2-phosphocreatine, 4 MgATP, 0.3 Na_3GTP (pH adjusted to 7.3 – 7.4 with KOH; osmolarity 280 – 290 mOsm), and 50 μM Alexa 488 dye (ThermoFisher; for pipette visualization under the two-photon microscope) or 125 K-Methanesulfonate, 7 KCl, 10 HEPES, 2 MgATP, 2 Na_2ATP, 0.5 Na_2GTP, 0.05 EGTA (pH adjusted to 7.3 with KOH; osmolarity 280-290 mOsm), and 50 μM Alexa 488 dye. Fully manual patch clamp experiments (Figures S2.4A-S2.4C) were performed following previously reported protocols (Häusser and Margrie, 2014; Komai et al., 2006).

Hardware and software setup

We modified a standard two-photon image-guided *in vivo* patch clamp rig to construct the imagepatching system (Figure 2.1C). Hardware for the standard rig included a two-photon laser scanning microscope (Ultima moving *IV*, Prairie Technologies), a mode-locked Ti-sapphire laser (Mai Tai HP; Spectra-Physics), a water-immersion objective (CFI75 LWD 16x W NA 0.8

WD 3.0mm objective, Nikon), a programmable 4-axis micromanipulator comprised of a single-axis micromanipulator (SMX-SA, Sensapex) mounted at a 30° angle below the horizontal on a left-handed three-axis micromanipulator (SMX-L-RS-50-HL-US, Sensapex), a pipette holder (Warner) mounted on the single-axis micromanipulator and connected to the CV-7B headstage of a patch amplifier (Multiclamp 700B, Molecular Devices) via an intermediate cable (IM-SMB, Sensapex), and a digitizer (Digidata 1440A, Molecular Devices) relaying signals between the amplifier and a computer. The laser was set to emit 960 nm (~800 mW average output power), which could excite both tdTomato and Alexa 488. To minimize bleed-through, we replaced the user-exchangeable PMT filters in the Ultima (which are optimized for dual labeling using Alexa 594 and Alexa 488) with red (630/30 nm, Chroma) and green (510/10 nm, Semrock) filters. The 4-axis micromanipulator was connected to a rotary knob controller (SMXS-K-2-RS-US) that communicated with the computer through a USB port.

The patch amplifier and the digitizer of the standard rig were connected to our autopatcher control box as previously described (Kodandaramaiah et al., 2012, 2016) (Figure 2.1C). The autopatcher control box was constructed as previously described (Kodandaramaiah et al., 2012, 2016), with a slight modification; potentiometers mounted on the front panel of the original autopatcher control box, each of which is used to manually pre-set a pressure value to be used during the autopatcher operation (see Kodandaramaiah et al., 2016 for details), were replaced by analog outputs from a standard data acquisition (DAQ) device (PCIe-6343, National Instruments) that can be programmed to send a command voltage of an arbitrary value to electronic pressure regulators inside the autopatcher control box, thus enabling automated, real-time control of the pipette pressure to any desired level at any rate (e.g., in a ramp) during the imagepatcher operation (note that PCIe-6343 can be replaced by any programmable device that can generate analog output ranging from 0 to 5 VDC, with < 400 mA).

To operate the microscope with ScanImage 3.8, a MATLAB-based open-source software package, previously reported instructions (Wilson et al., 2013) were followed to make necessary connections between the microscope hardware and the computer. ScanImage was configured such that each acquired image has a single frame with 256 lines per frame and 256 pixels per line, and each line is scanned in 2.64 ms for a frame rate of 1.48 frames per second. To acquire high quality images of a neuron at the end of the imagepatching experiment (example image in Figure 2.3D), ScanImage was configured to produce 2048 lines per frame and 2048 pixels per line at a frame rate of 0.18 frames per second.

We used MATLAB R2013b (MathWorks) to write and run our program executing the imagepatching algorithm. Our program was divided into two main modules: (i) a graphical user interface (GUI) that allows the user to start the imagepatching algorithm and to view the results of image acquisition as well as analysis during the algorithm execution (see Methods S1 in Suk et al., 2017, "find_cells_gui_SI.m"); (ii) image analysis code that is executed upon the completion of image acquisition to perform real-time image analysis (see Methods S1 in Suk et al., 2017, "image_autopatcher_v1.m"; MATLAB scripts can be bound to one or more ScanImage events, such as the start of the ScanImage software and the completion of image acquisition, by adding them as user functions; see Appendix: Imagepatcher user manual and the ScanImage website [https://openwiki.janelia.org/wiki/pages/viewpage.action?pageId=29524376] for details). A ScanImage function responsible for image frame generation, called makeFrameByStripes, was

augmented with our code to direct raw image data acquired by the microscope to our image analysis code (see Methods S1 in Suk et al., 2017, "makeFrameByStripes.m," for the function with our code).

During the imagepatcher operation, when the pipette resistance had to be measured, the autopatcher digital board (USB-6211, National Instruments) was used to apply 50 Hz, 10 mV square waves to the pipette tip and to record the resulting current pulses at 20 kHz. 10 mV (i.e., amplitude of the applied voltage) was divided by the amplitude of each current pulse, and the average of the resulting values was assigned as the pipette resistance while the standard deviation of the resulting values was used as a metric quantifying the amount of heartbeat modulation. We performed whole-cell recordings of patched cells using Clampex 10.4 (Molecular Devices), acquiring data through a low-pass filter (Bessel filter, 10 kHz cutoff) at a rate of 40,000 samples per second. The acquired signals were analyzed using MATLAB 2013b (MathWorks) and Clampfit 10.5 (Molecular Devices).

Assessment of target cell movements in response to pipette navigations into and inside the brain

Cell movements following the pipette navigation into the brain (Figure S2.1A) were observed by first locating a tdTomato-labeled cell ~150 – 250 μm below the brain surface and recording the coordinates of the cell centroid (visually assessed). Using trigonometric functions in MATLAB, the pipette trajectory parallel to the pipette axis (i.e., 30° below the horizontal) was then calculated, setting the start and the end of the trajectory to the locations 25 μm above the brain surface and 50 μm directly above the cell centroid respectively. Subsequently, a patch pipette whose resistance value was between 5 – 7.5 MΩ was filled with the internal solution and installed into the pipette holder that was positioned on the left side of the craniotomy. While applying low positive pressure (~15 – 30 mBar), the pipette was moved into the ACSF covering the brain, positioning the pipette tip at the start position of the calculated trajectory. A high positive pressure (~200 – 300 mBar) was then applied to the pipette, and the single-axis micromanipulator (i.e., the micromanipulator whose axis is parallel to the pipette axis) was controlled using MATLAB code (Methods S1 in Suk et al., 2017, "move_sensapex_manipulator_HJS.m") interacting with a software development kit from Sensapex (the software development kit available on the Sensapex website [http://www.sensapex.com/support/downloads-updates/]) to automatically and accurately move the pipette along the calculated trajectory at ~600 μm/s. When the pipette movement was complete, a z-stack (20 or 24 images, 2 μm or 3 μm step size, 17x zoom) was acquired around the original cell centroid coordinates that were recorded before the pipette movement. The z-stack was analyzed post-hoc to determine the new coordinates of the cell centroid (visually assessed), and these coordinates were compared to those of the cell centroid before the pipette movement into the brain to quantify the amount of cell displacement.

To determine the amount of cell movement in response to the pipette navigation inside the brain (Figure S2.1B), a patch pipette (resistance value 5 – 7.5 MΩ) filled with the internal solution was first placed inside the brain, with its tip located ~20 – 30 μm above a tdTomato-labeled cell and ~5 – 13 μm away from the cell centroid in the transverse plane, simulating an offset from the pipette tip to the target cell that can result from the pipette entry into the brain. After recording the coordinates of the cell centroid (visually assessed), the micromanipulator was

automatically moved using MATLAB code (Methods S1 in Suk et al., 2017, "move_sensapex_manipulator_HJS.m") in the x, y, and z directions to place the pipette tip ~10 – 20 μm directly above the cell centroid, which is where an investigator manually performing patching would aim to bring the pipette tip to approach the targeted cell in the vertical direction (Häusser and Margrie, 2014; Komai et al., 2006). Once the micromanipulator movement was complete, a z-stack (20 or 24 images, 2 μm or 3 μm step size, 17x zoom) was acquired around the cell centroid coordinates that were recorded prior to the pipette navigation. Post-hoc analysis of the z-stack was then performed to locate the new cell centroid (visually assessed), coordinates of which were compared to those of the cell centroid before the pipette navigation inside the brain to quantify the amount of cell movement.

Details of the pipette tip detection algorithm

The pipette tip detection algorithm first applies a 2D Gaussian filter (19 x 19 window; 9/2 variance) to each image in the z-stack of a patch pipette to remove the background noise. The filtered topmost image of the stack is then subjected to a range of threshold values (corresponding to 1 – 95% of the maximum pixel intensity of the filtered image) to determine the maximum threshold value at which the resulting cluster of bright pixels (Figure 2.2A(ii.i), area bounded by yellow outline) has a characteristic shape (i.e., has 3 endpoints when subjected to the bwmorph function with 'endpoints' operation in MATLAB); in case of multiple clusters for a single threshold value, the largest cluster (i.e., the cluster composed of the highest number of pixels) is analyzed for the endpoint detection. Subsequently, the cluster obtained from the filtered topmost image at this threshold value is analyzed to determine its area (i.e., number of pixels in the cluster; using MATLAB's bwboundaries function) and centroid (Figure 2.2A(ii.i), black x; using MATLAB's regionprops function with 'centroid' as an input argument). The detected centroid is also considered as the pixel corresponding to the far end of the pipette (i.e., the end opposite to the pipette tip) and used as the reference point in the subsequent stages of the algorithm. The rest of the filtered images in the stack are then subjected to a range of threshold values, identifying the threshold value for each image at which the resulting cluster has an area closest to that obtained from the topmost image (Figure 2.2A(ii.ii), (ii.iii), areas bounded by yellow outlines); in case of multiple clusters for a single threshold value, the largest cluster (i.e., the cluster composed of the highest number of pixels) is used for the area comparison. Each of the resulting cluster is subsequently subjected to MATLAB's regionprops function (with 'centroid' as an input argument) to locate its centroid (Figure 2.2A(ii.ii), (ii.iii), yellow x's). The distance between this cluster centroid and the reference point (i.e., cluster centroid in the topmost image of the stack; Figure 2.2A(ii.i), black x) is calculated for each image, and the calculated values are sorted according to the image number (Figure 2.2A(iii)), with the images in the stack numbered from top to bottom (i.e., the topmost image was image 1). After filtering the sorted distance values with a 5-point moving average filter, the algorithm identifies the image number at which the filtered distance value starts to flatten (Figure 2.2A(iii), magenta line) by first calculating the approximate derivative of the filtered values (i.e., difference between two consecutive filtered values), then filtering the approximate derivative using a 19-point moving average filter, and finally finding the first instance where the filtered derivative value exceeds the original derivative value. The algorithm assigns the z-coordinate of the corresponding image as the z-coordinate of the pipette tip (Figure 2.2A(iii), $z_{pipette}$).

After assigning the z-coordinate of the pipette tip, the algorithm calculates the angle

between the cluster centroid in image 1 (Figure 2.2A(ii.i), black x) and the cluster centroid in the image at $z_{pipette}$, which is assigned as the pipette angle in the transverse plane. Subsequently, the image at $z_{pipette}$, smoothed by a 2D Gaussian filter (19 x 19 window; 9/2 variance) (Figure S2.3A(i)), is segmented using a range of threshold values (corresponding to 5 – 75% of the maximum pixel intensity of the filtered image). The algorithm then analyzes the resulting clusters (Figure S2.3A(ii), white) for the endpoint detection (using the bwmorph function with 'endpoints' operation in MATLAB; Figure S2.3A(ii), yellow boxes); in case of multiple clusters for a single threshold value, the largest cluster (i.e., the cluster composed of the highest number of pixels) is analyzed for the endpoint detection. The lowest threshold value at which the resulting cluster has 3 vertices or endpoints (Figure S2.3A(ii.ii), yellow boxes) is considered optimal for isolating the pixels that accurately represent the entire body of the pipette tip, and the corresponding cluster of pixels (Figure S2.3A(ii.ii), white) is further analyzed for the pipette tip detection; other threshold values that are higher or lower than the optimal value result in clusters that have less or more than 3 endpoints, and are not further analyzed (example images of the clusters resulting from a threshold value higher and lower than the optimal value shown in Figure S2.3A(ii.i) and (ii.iii) respectively, with the yellow boxes representing the endpoints of these clusters). Out of all the pixels in the cluster resulting from the optimal threshold value, the one that is the furthest away from the centroid of the cluster is identified. Its distance to the centroid is then used as the length of a line (Figure S2.3A(iii), yellow dotted line) pointing in the direction of the pipette angle in the transverse plane (the angle that was determined earlier as described above) and emanating from the cluster centroid (Figure S2.3A(iii), yellow x). The pixel in the cluster closest to the endpoint of the line is assigned as the tip of the pipette in the transverse plane (Figure S2.3A(iii), yellow star; Figure 2.2A(iv), yellow star), and the location of the pixel in the image is assigned as the x and y coordinates of the pipette tip. See "find_one_pipette_HJS.m" and "pipette_tip_detection_HJS.m" in the Methods S1 in Suk et al., 2017 for MATLAB codes running the algorithm.

Details of the cell position detection algorithm

The cell position detection algorithm begins its operation by subjecting each image in the z-stack of a tdTomato-expressing cell to a 2D Wiener filter (3 x 3 window), removing the background noise. Each filtered image (example filtered image shown in Figure S2.3B(i)) is then segmented using a range of threshold values (corresponding to 5 – 95% of the maximum pixel intensity of the filtered image), and the area of (i.e., the number of pixels in) the resulting clusters of pixels (Figure S2.3B(ii), white) is compared to a reference area (i.e., the area of the target cell chosen by the user during the target cell detection and selection stage); in case of multiple clusters for a single threshold value, the cluster whose centroid is the nearest to the image center and whose area is the closest to the reference area is used for the area comparison. The threshold value at which the resulting cluster of pixels has the area closest to the reference area is considered optimal for identifying the pixels accurately representing the target cell soma, and is isolated by the algorithm from other threshold values that lead to clusters of pixels that represent only a small portion of the cell body (example image of such a cluster shown in Figure S2.3B(ii.i)) or capture background pixels (example image of such a cluster shown in Figure S2.3B(ii.iii)). The cluster obtained by using the optimal threshold value (Figure S2.3B(ii.ii)) is then subjected to MATLAB's bwboundaries function to determine the pixels that represent the boundary (Figure S2.3B(ii.ii), red outline; Figure 2.2B(ii), red outline) and the interior (Figure S2.3B(ii.ii), white; Figure 2.2B(ii), area inside the red outline) of the cross-section of the cell

body captured by each image in the stack. The centroid of the cluster (Figure S2.3B(iii), red x) is also determined using MATLAB's regionprops function (with 'centroid' as an input argument). The algorithm then calculates the mean intensity of pixels representing the interior of the cell body from each image and sorts the calculated values according to the image number, with the images in the stack numbered from top to bottom (i.e., the topmost image was image 1; example plot of the mean pixel intensity as a function of image number shown in Figure 2.2B(iii)). The image capturing the cross-section of the cell body with the highest mean pixel intensity (i.e., the brightest cross-section of the cell body; Figure 2.2B(iii), magenta line) is considered to be focused on the centroid of the cell body, and its z-coordinate is assigned as the z-coordinate of the cell centroid (Figure 2.2B(iii), z_{cell}). Subsequently, the x and y coordinates of the cluster centroid in the image at z_{cell} (Figure S2.3B(iii), red x; Figure 2.2B(iv), red x), which is determined along with those of the clusters in other images in the stack as described above, are assigned as the x and y coordinates of the cell centroid. See "soma_contour_detection.m" and "image_autopatcher_v1.m" in Methods S1 in Suk et al., 2017 for MATLAB codes running the algorithm.

Micromanipulator-microscope platform calibration

Before performing imagepatching experiments, step sizes of motion and axis angles of the micromanipulator were automatically calibrated to those of the motorized platform of the two-photon microscope, which moved the microscope objective relative to the sample to be imaged, using the imagepatcher. In the first stage of calibration, which was performed once upon initial hardware setup, a patch pipette filled with 50 μM Alexa 488 dye (in deionized water) was installed into the pipette holder, and its tip was manually moved to the center of the field-of-view using the rotary knob controller of the 4-axis micromanipulator. The expected angle below the horizontal for each of the 4 micromanipulator axes was then specified by typing in a value in the corresponding text box on the imagepatcher GUI (for our micromanipulator, 30 for diagonal, 0 for x, 0 for y, and 90 for z-axis). Subsequently, the calibration of one of the micromanipulator axes was initiated by clicking one of four pushbuttons displayed on the GUI, each button corresponding to the calibration of each of the 4 axes of the micromanipulator. Pressing the pushbutton started the acquisition of a z-stack (20 images, 2 μm step size, 17x zoom) around the pipette. The location of the pipette tip was then automatically identified using the pipette tip detection algorithm (Figure 2.2A), and the imagepatcher program sent a command to the micromanipulator to move the axis being calibrated forward by a pre-set distance (30 μm for the diagonal axis; 25 μm for x, y, and z axes). Following the micromanipulator movement, the microscope objective was moved to the expected pipette tip position; the expected pipette tip position was calculated by first mapping the micromanipulator axis movement to the x, y, and z directional movements of the motorized platform of the microscope, using both the pipette angle in the transverse plane, which was obtained from the z-stack using the pipette tip detection algorithm (Figure 2.2A), and the expected angle below the horizontal of the moved axis (e.g., when a pipette facing dead-right moves along the diagonal axis by 30 μm, the pipette tip moves by $30 \cdot \cos(30^\circ) \cdot \cos(0^\circ) \approx 26$ μm in the x-direction, $30 \cdot \cos(30^\circ) \cdot \sin(0^\circ) = 0$ μm in the y-direction, and $30 \cdot \sin(30^\circ) = 15$ μm in the z-direction), and then adding the mapped values to the original pipette tip location. With the microscope objective at the expected pipette tip position, another z-stack (20 images, 2 μm step size, 17x zoom) was acquired, and the actual pipette tip location was determined using the pipette tip detection algorithm (Figure 2.2A). The angle and the distance between the new tip location and the original tip location were then calculated in the angle and

distance units of the microscope's motorized platform. Subsequently, the calculated values were assigned to the forward movement of the micromanipulator axis being calibrated. For the backward movement calibration, the program moved the axis of the micromanipulator backward by the pre-set distance (30 μm for the diagonal axis; 25 μm for x, y, and z axes) and then detected the resultant pipette tip location. As done for the forward movement calibration, the angle and the distance between the tip locations before and after the backward movement were calculated in the microscope's motorized platform units, and the calculated values were assigned to the backward movement of the micromanipulator axis being calibrated. The forward and backward movement calibrations were then repeated for other pre-set distances (55, 150, 320, 350, 420, and 480 μm for the diagonal axis; 150, 325, 400, and 460 μm for x and y axes; 50, 150, 200, and 250 μm for the z axis). Once the calibration for the axis was complete, the calibration results were saved into a .m file, which we could load to our program for future imagepatching experiments. Without replacing the patch pipette, each of the rest of the micromanipulator axes was calibrated in the same way as described above.

The second stage of calibration was implemented to account for a variability in the locked position of the pipette, which stemmed from a lever-based locking mechanism of our micromanipulator. Unlike the first stage that was performed only once, the second stage of calibration was automatically executed for each imagepatching experiment at the start of the brain penetration stage (Figure 2.1B(iii)). Right before performing the second stage of calibration, the amount that each micromanipulator axis would have to move to reach the targeted position inside the brain (i.e., 50 μm directly above the target cell centroid) was calculated using the calibration results from the first stage. Subsequently, the new calibration results were obtained by moving each micromanipulator axis by the calculated amount and finding the new pipette tip location following the axis movement; the new pipette tip location was determined using the same procedure implemented for the first stage of calibration, except the expected pipette tip position after the micromanipulator movement was calculated using the calibration results from the first stage instead of the expected angle below the horizontal specified in the imagepatcher GUI. See "find_cells_gui_SI.m" in Methods S1 in Suk et al., 2017 for MATLAB code executing the calibration.

Details of the imagepatcher operation

At the start of the imagepatching experiment, we opened ScanImage and imaged the brain inside the craniotomy to visually determine the location of the brain surface. The z-position of the objective corresponding to where we found the brain surface was denoted as the z-coordinate of the brain surface by the imagepatcher. We then specified the number of images (5 – 10), the step size between two consecutive images (5 – 10 μm), and the starting depth (100 – 250 μm) of a z-stack to be acquired inside the brain by using the corresponding text boxes on the imagepatcher GUI. The z-stack acquisition (and the target cell detection and selection stage; Figure 2.1B(i)) was started by pressing the corresponding pushbutton on the imagepatcher GUI, and a display window inside the GUI sequentially showed the most recently acquired image during the stack acquisition. At the end of the stack acquisition, the GUI also showed the list of acquired images, which could be used to select images to display in the display window and to run automated cell detection on. After choosing 1 – 3 images, each capturing at least one or two bright cells (visually assessed), by clicking the images in the list, we set the minimum brightness (specified as percentage of the maximum pixel intensity of each of the selected images) of cells

to detect to any value between 10 and 25% while setting the desired minimum and maximum cell body radii to 3 and 15 μm respectively by using the corresponding text boxes on the GUI. Out of all the tdTomato-expressing PV-positive neurons captured by the images, only those that met our detection criteria were identified by the imagepatcher and shown with red outlines in the display window of the GUI; the imagepatcher detected the cells by smoothing each of the selected images using a 2D Wiener filter (3 x 3 window), then segmenting each of the filtered images using the minimum brightness as the threshold value, and finally determining the boundary of resulting objects that met our radii specifications (see "find_center_and_circle_soma_cell_radius_range.m" in Methods S1 in Suk et al., 2017 for MATLAB code responsible for the cell detection). To conclude the target cell detection and selection stage, we chose a target cell to patch by clicking the interior of one of the outlined cells in the display window, which turned the outline of the selected cell to yellow and registered the information about the target cell (x, y coordinates of the target cell centroid, z-coordinate of the target cell depth, area of the target cell, minimum brightness threshold for the cell detection) in the imagepatcher.

Following the target cell selection, we initiated the pipette tip detection stage (Figure 2.1B(ii)) by clicking the corresponding pushbutton on the GUI. This stage began with the autopatcher control box outputting 15 mBar to the pipette while the imagepatcher moved the microscope objective vertically to position the objective away from the brain surface and to provide enough space for a patch pipette. We then filled a pipette with the internal solution, installed it into the pipette holder, and used the rotary knob controller of the 4-axis micromanipulator to manually move the pipette tip to the center of the objective field-of-view (FOV). While imaging the pipette via ScanImage, we used a slider presented on the imagepatcher GUI to adjust pipette pressure to a value that minimized a plume of dye at the pipette tip and subsequently made the pipette tip clearly visible (visually assessed; typically 6 to 8 mBar). A z-stack (20 images, 2 μm step size, 17x zoom) was then acquired around the pipette tip by pressing the corresponding pushbutton on the GUI. From this stack of images, the imagepatcher detected the pipette tip (using the pipette tip detection algorithm described in Figure 2.2A) and logged the maximum intensity of pixels representing the pipette in the image focused on the pipette tip.

Next, the brain penetration stage (Figure 2.1B(iii)) was started by clicking the corresponding pushbutton on the GUI. Before moving the pipette into the brain, step sizes of motion and axis angles of the micromanipulator were automatically calibrated to those of the motorized platform of the two-photon microscope (i.e., the second stage of micromanipulator calibration was performed; see "Micromanipulator-microscope platform calibration" section for details); in subsequent steps of the imagepatching process, the imagepatcher calculated the pipette tip location by adding calibrated micromanipulator axes displacements to the original pipette tip location before the micromanipulator movement. Following the calibration, the imagepatcher calculated a linear path along the diagonal axis of the micromanipulator (i.e., a trajectory parallel to the pipette axis) with the start and end points located 25 μm above the brain surface and 50 μm directly above the target cell centroid respectively. The micromanipulator was then automatically moved to bring the pipette tip to the start point of the calculated path, and 600 mBar was applied to the pipette by the autopatcher control box. At this point, the imagepatcher measured the pipette resistance for 5 seconds and displayed the result; if the displayed value was

outside of an acceptable range (e.g., 5 – 7.5 MΩ), it was assumed that the pipette was clogged with some undesired particles (in case of resistance greater than 7.5 MΩ) or the pipette tip was broken (in case of resistance less than 5 MΩ), and we retracted the pipette to install a new one. For the pipette with a resistance value within the acceptable range, the imagepatcher logged the pipette resistance and then moved the pipette along the calculated path into the brain. Once the pipette tip entered the brain and was positioned 75 μm above the target cell centroid (i.e., 25 μm above the endpoint of the calculated trajectory), dye ejection at the pipette tip was examined by the imagepatcher to check the pipette tip quality; if an image (17x zoom) capturing the pipette tip at the image center had either the maximum pixel intensity at least 2 times higher than that logged at the end of the pipette tip detection stage (i.e., maximum intensity of pixels representing the pipette in the image focused on the pipette tip, acquired outside the brain), or the median of pixel intensities at least 40% of the maximum pixel intensity of the image and the maximum pixel intensity at least as high as the maximum intensity logged at the end of the pipette tip detection stage, the imagepatcher considered the pipette to be clean (see Methods, "Derivation of dye-ejection based pipette blockage test for derivation of these criteria"). Once the clean pipette reached the end point of the calculated path (i.e., 50 μm above the target cell centroid), its pressure was automatically lowered to 300 mBar, and the imagepatcher checked the pipette tip for clogging by measuring the pipette resistance and comparing the measured value to the value obtained outside the brain (i.e., 25 μm above the brain surface), and by performing another evaluation of dye ejection. After this quality check, the imagepatcher acquired a z-stack (24 images, 3 μm step size, 17x zoom) around the original target cell centroid (i.e., target cell centroid logged at the end of the target cell detection and selection stage) and determined the target cell position (using the cell position detection algorithm described in Figure 2.2B) to update the target cell location. The imagepatcher then logged this new cell position and moved the x, y, and z axes of the micromanipulator such that the pipette tip would be 25 μm directly above the updated target cell centroid. After the micromanipulator movement, the dye ejection and the pipette resistance were again examined by the imagepatcher to check the pipette tip for clogging, concluding the brain penetration stage.

At the start of the closed-loop real-time image-guided pipette positioning stage (Figure 2.1B(iv)), the pipette pressure was automatically lowered to 100 mBar, and another z-stack (10 images, 2 μm step size, 17x zoom) was automatically acquired around the target cell centroid logged during the brain penetration stage. After finding the coordinates of the target cell centroid from the stack (using the cell position detection algorithm described in Figure 2.2B), the imagepatcher entered the closed-loop (Figure 2.1A), repeatedly updating the cell centroid location and positioning the pipette tip directly above the cell centroid following each 3 μm-pipette step in the z-direction. Every z-step of the pipette was followed by automatic acquisition of two images; to support repeated cell centroid detection while minimizing image acquisition time, one image, instead of a full z-stack, was captured at the z-coordinate of the cell centroid determined at the start of the stage, with an assumption that small z-steps used in the closed-loop would cause negligible movement of the cell in the z-direction; the second image was acquired at the calculated location of the pipette tip to check for dye ejection and subsequently verify the pipette tip quality as done in the preceding stage. The imagepatcher also measured the pipette resistance and logged the measured value after each pipette step in the z-direction to monitor changes in the pipette resistance. When the imagepatcher detected a small resistance increase while approaching the target cell, the pipette pressure was automatically lowered to 30 mBar and

the current pulses at the pipette tip were checked for another increase in resistance as well as heartbeat modulation, both of which indicated tight contact between the pipette tip and the cell membrane.

Once this resistance increase and heartbeat modulation were detected, the imagepatcher initiated the gigaseal formation stage (Figure 2.1B(v)). In this stage, the pipette movement was stopped, and suction as well as hyperpolarizing voltage were automatically applied to form a gigaohm seal between the pipette and the cell membrane. Once a stable gigaseal was established (i.e., the pipette resistance stayed above a gigaohm and did not increase by more than 15% over a 15-second period), the imagepatcher GUI displayed a pushbutton for starting the break-in process. By clicking this pushbutton, we started the break-in stage (Figure 2.1B(vi)). At the start of the stage, the imagepatcher established a baseline of cell filling by the pipette dye (i.e., determined the amount of pipette dye inside the target cell) by acquiring a z-stack (10 images, 2 μm step size, 17x zoom) around the cell, identifying pixels corresponding to the cell body in the focused image of the stack using the cell position detection algorithm described in Figure 2.2B, and calculating the mean pixel intensity of the cell body in the microscope channel corresponding to the pipette dye (channel 2 for our microscope). Subsequently, suction pulses were applied in a ramp by the autopatcher control box while monitoring the seal resistance. Once the resistance dropped below a value characteristic of the whole-cell state, the imagepatcher imaged the target cell again (at the cell depth and centroid determined from the previous z-stack; 1 image, 17x zoom) to calculate the mean pixel intensity within the cell boundary in channel 2. When the new mean value was at least 15% higher than the original value obtained before the suction pulses, the imagepatcher considered the cell to be filled sufficiently with the pipette dye and concluded the break-in stage. Once the imagepatcher operation was complete, we recorded signals from cells that had achieved a successful whole-cell state, which we defined as that requiring no more than 500 pA current injection to hold the cell at -65 mV (i.e., exhibiting holding current less than or equal to 500 pA) in the voltage-clamp mode, as we did previously (Kodandaramaiah et al., 2012). See Appendix A: Imagepatcher user manual for detailed description on how to interact with the imagepatcher GUI for an imagepatching experiment.

Performance of the pipette tip detection algorithm at angles other than 30° below the horizontal

15 pipettes all angled at 25° below the horizontal were each imaged using a z-stack (2 μm step size, 20 images, 17x zoom), with each z-stack capturing the pipette tip at a distinct position within the stack. By applying the pipette tip detection algorithm (Figure 2.2A) to each of the 15 z-stacks, we found that the algorithm yielded pipette tip locations that were close to those determined visually, with the tip positions from the algorithm and from visual assessment differing by (mean ± s.d.) -1.5 ± 1.4 μm, 0.1 ± 1.0 μm, and 1.6 ± 3.0 μm in the x, y, and z directions respectively. The pipette tip detection algorithm also enabled accurate tip detection from another 15 z-stacks (2 μm step size, 20 images, 17x zoom) that each captured the tip of a separate pipette angled at 35° below the horizontal at a distinct position within the stack; the tip locations determined by the pipette tip detection algorithm from the 15 z-stacks were (mean ± s.d.) -0.7 ± 0.5 μm, -0.5 ± 0.8 μm, and 0.4 ± 1.4 μm off of the visually assessed tip positions in the x, y, and z directions respectively.

Derivation of pipette pressure for brain entry and cell approach

To determine the optimal pipette pressure for entering the brain during the brain penetration stage (Figure 2.1B(iii)), a few penetrations were performed with 100 mBar, 200 mBar, 400 mbar, 600 mBar, and 800 mBar pressure applied at the back of the pipette (these pressure values were chosen based on previously reported protocols for fully manual two-photon image-guided or blind patch clamp recordings *in vivo* (Häusser and Margrie, 2014; Komai et al., 2006; Lee et al., 2009; Margrie et al., 2002), in which pipette pressure ranging from 100 mBar to 800 mBar were typically used). For our experiments, we used Alexa 488-filled patch pipettes angled at ~30° below the horizontal, moving ~300 – 400 μm in the diagonal direction (i.e., parallel to the pipette axis), from outside the brain near the brain surface to inside the brain (i.e., ~150 – 200 μm deep in the cortex; layer 2-3 for adult mouse brain (Altamura et al., 2007; Mountcastle, 2003)), at ~600 μm/s (i.e., the maximum speed that our 4-axis micromanipulator could generate under software control). As expected, higher pressure (i.e., 600 mBar and 800 mBar) produced less pipette blockage compared to lower pressure values. However, 800 mBar led to much background signal that caused bleed-through of the Alexa 488 signal into the imaging channel used to visualize tdTomato, making it difficult to resolve tdTomato-expressing cells after brain penetration. As a result, we decided to focus on 600 mBar and found the pressure to cause a reasonably low pipette blockage rate (12.5%; 2 out of 16 trials; 3 PV-Cre x Ai14 mice) when used as the pipette pressure for brain penetration. We therefore chose to implement 600 mBar as the pipette pressure for brain entry during the brain penetration stage of the imagepatching algorithm (Figure 2.1B(iii)).

The optimal set of pipette pressure levels for approaching the cell once inside the brain was determined based on our manual patching experiments as well as the values provided in previously reported protocols for manual patching (Häusser and Margrie, 2014; Komai et al., 2006). During our manual slice and *in vivo* patching experiments, we had a few trials in which a gigaohm seal was quickly obtained with an Alexa 488-filled pipette that continuously ejected a plume of dye at its tip until right before it made contact with the target cell. From these trials, we inferred that one of the most critical prerequisites of gigaseal formation might be maintaining a "clean" pipette tip throughout its movement inside the tissue, all the way up to the point where it makes contact with the target cell (this assumption agrees with what has been briefly described in Margrie et al., 2002). During our initial experiments, we observed that the pipette would often cease to eject the dye at its tip (i.e., the pipette was contaminated, as described in Komai et al., 2006) while moving inside the tissue at 20 – 40 mBar, which is the range of pipette pressure values used in previously reported protocols for two-photon image-guided patching *in vivo* (Häusser and Margrie, 2014; Komai et al., 2006). We tried a few different pressure values that were higher than 40 mBar, and found 100 – 300 mBar to be high enough to keep the pipette tip blockage rate reasonably low (21.7%; 5 out of 23 trials; 5 PV-Cre x Ai14 mice) while navigating the pipette inside the tissue, but not so high as to cause bleed-through of the pipette dye fluorescence into the tdTomato imaging channel. However, we also noticed that when the pipette pressure was ~300 mBar, the cells were often "blown away" by the pipette even when the pipette tip was somewhat distant from the target cell (e.g., ~10 – 20 μm from the target cell membrane, which corresponded to ~20 – 30 μm distance between the pipette tip and the center of a ~20 μm diameter cell). To prevent the pipette blowing away the target cell, we tried a few combinations of distances and pressure values for approaching the target cell. As a result, we found a pressure of ~100 mBar to keep the cell in place right until the pipette tip made contact with the cell membrane (contact between the pipette tip and the cell membrane was visually assessed by

observing the presence of heartbeat modulation as in Komai et al., 2006; n = 17 tdTomato-expressing PV-positive cells from 3 PV-Cre x Ai14 mice). We therefore decided to implement three different pressure values in the brain penetration (Figure 2.1B(iii)) and closed-loop real-time image-guided pipette positioning (Figure 2.1B(iv)) stages of the imagepatching algorithm while approaching the target cell: (i) 600 mBar for moving the pipette into the brain through upper cortical layers to 75 μm away from the center of the target cell; (ii) 300 mBar for moving the pipette to 25 μm away from the center of the target cell; (ii) 100 mBar for making the final approach to the cell.

Optimization of cell-pipette contact detection, gigaseal formation, and break-in

Akin to manual two-photon image-guided patching (Häusser and Margrie, 2014; Komai et al., 2006; Margrie et al., 2003) and our previously developed blind autopatching method (Kodandaramaiah et al., 2012, 2016), imagepatching uses an increase in pipette resistance as a signal for when the pipette tip contacts the cell membrane. To determine the amount of resistance increase corresponding to a cell membrane-pipette tip contact amenable to a gigaohm seal, we tried forming a gigaseal (by applying slight suction to the pipette and hyperpolarizing the pipette) after observing resistance increases over consecutive z steps (3 μm step size). After a few trials on tdTomato-expressing PV-positive neurons in somatosensory and motor cortices of anesthetized PV-Cre x Ai14 mice, we found that a 20 – 50% increase in pipette resistance, which is the amount visually assessed during manual patching when the pipette tip-cell membrane contact is amenable to gigaseal formation (Häusser and Margrie, 2014; Margrie et al., 2002, 2003), was hard to observe when the increase in resistance was calculated over a single z step (i.e., over 3 μm; step size of 3 μm was used for single z steps throughout cell-pipette contact detection optimization described below) of a pipette at 100 mBar. This characteristic resistance increase was observable by taking one or more additional steps towards the target cell after seeing some resistance increase over 3 μm, but these extra steps sometimes damaged the cell membrane, resulting in cell lysis. Even when the cell seemed intact, releasing the positive pressure and applying light suction following the 20 – 50% resistance increase over 2 or more consecutive z steps (i.e., over 6 μm or more) did not improve the rate of forming a gigaseal compared to the same pressure modulation following a single z step with less resistance increase, maybe because the pipette tip was pushed too much into the target cell, damaging the cell membrane. As expected, there were instances in which analyzing the pipette resistance over a single z step seemed "noisy", showing some resistance increases even when the pipette tip was far away from the target cell membrane. However, we could minimize the number of such false positives by analyzing the resistance increase only when the distance between the pipette tip and the cell centroid was small enough that a contact was likely (e.g., the pipette tip-cell centroid distance was less than the radius of the target cell). As a result, we decided to closely examine the resistance increase over a single z step of a patch pipette as the tip of the pipette at 100 mBar was brought in contact with the cell membrane, aiming to determine the amount of resistance increase that subsequently maximized the rate of forming a gigaseal. Since most of the single z steps led to a pipette resistance increase of less than 1% when the pipette tip was far away from the cell membrane, we studied the relationship between the amount of resistance increase of at least 1% over a single z step and the likelihood of successful gigaseal formation. By analyzing 46 gigaseal formation attempts (in 14 mice), in which we released positive pressure and applied suction using the autopatcher control box immediately after observing a resistance increase of 1% or more over a single z step, we found that resistance increases by 4% or more over a single

z step led to successful gigaseal formation 22.2% of the time (n = 4 gigaseals out of 18 attempts), while single z steps with a resistance increase between 1% and 4% yielded a higher rate of successful gigaseal formation of 32.1% (n = 9 gigaseals out of 28 attempts). Out of the 28 attempts with a resistance increase between 1% and 4% over a single z step, we also found that single z steps with a resistance increase between 1 and 2% were more likely to result in successful gigaseal formation (50%; n = 4 gigaseals out of 8 attempts) compared to those with higher amounts of resistance increase (e.g., 27.3%, or n = 3 gigaseals out of 11 attempts, for single z steps with a 2 – 3% resistance increase; 22.2%, or n = 2 gigaseals out of 7 attempts, for single z steps with a 3 – 4% resistance increase). As a result, we decided to use a resistance increase by 1% over a single z step (i.e., an increase by ~60 – 70 kΩ over 3 μm for 6 – 7 MΩ pipettes) as the threshold in the imagepatching algorithm for the detection of contact between the pipette tip and the cell membrane.

Once the pipette tip made contact with the cell membrane, the micromanipulator was halted to keep the pipette stationary, and the pipette pressure was lowered from 100 mBar to 30 mBar to prepare the target cell for gigaseal formation. From a few manual patching experiments, we found that this reduction in pipette pressure led to an increase in pipette resistance by ~1.5% or more when the pipette tip was in close contact with the cell membrane, perhaps because the lower positive pressure allowed the cell membrane, which had been displaced away from the pipette tip due to the higher positive pressure, to spring back towards the pipette tip. In addition to the resistance increase, we could also observe heartbeat modulation of the pipette current pulses as described before (Häusser and Margrie, 2014; Komai et al., 2006; Margrie et al., 2002). The metric used to quantify heartbeat modulation was derived based on our finding during manual patching that, when the pipette tip was in close contact with the cell membrane, current pulses resulting from 50 Hz square waves of injected voltage had a characteristic variation in their resistance values when obtained over 1 second. Specifically, we observed that when the pipette tip at ~30 mBar was in tight contact with the cell membrane, the resistance values of 50 current pulses (corresponding to a 1-second long measurement; resistance was calculated by dividing the amplitude of the injected voltage by the amplitude of an observed current pulse) showed a standard deviation of at least 0.1 MΩ, and a subsequent suction led to a gigaseal (n = 6 neurons, 6 mice). We therefore used the standard deviation of the current pulse resistances calculated over 1 second at 30 mBar pipette pressure as a second criterion for detecting contact between the pipette tip and the cell membrane. Even when the resistance increase was less than ~1.5% or the amount of heartbeat modulation was less than 0.1 MΩ, a tight contact amenable to gigaseal formation could be achieved by first increasing the pipette pressure back to 100 mBar (to clear the pipette tip in case it became partially occluded while at 30 mBar) and then advancing the pipette tip by one or more additional z steps until a resistance increase by ~1.5% or more was observed. We mimicked this resistance-based check for the pipette tip-cell membrane contact at 30 mBar in the imagepatching algorithm by first performing two consecutive resistance measurements in response to 50 Hz square waves, each for 1 second, then comparing each of the average resistance values (each taken over 1 second) to the pipette resistance observed before reducing the pipette pressure to 30 mBar, and finally resuming the pipette z steps if the resistance increase was less than 1.5% or if the standard deviation of current pulse resistances was less than 0.1 MΩ (see Figure S2.2, "closed-loop real-time image-guided pipette positioning," for details).

After checking the pipette tip-cell membrane contact at 30 mBar, a ramp of suction (-20 mBar/s) was applied to reach a final value of -20 mBar, to achieve a gigaohm seal. If the rate of resistance increase was slow (i.e., the pipette resistance measured 10 seconds after the suction reached the final value of -20 mBar was less than 2 times the resistance measured right before applying the ramp of suction), stronger suction up to -100 mBar was applied in a ramp at -20 mBar/s; negative pressure stronger than -100 mBar was not implemented based on our observation during manual trials that suction levels more negative than -100 mBar did not help to form a gigaseal, but instead led to premature and leaky break-ins. The holding voltage was also set to -65 mV as the seal was being formed. If the pipette resistance did not reach 300 MΩ within 5 seconds after applying the hyperpolarizing voltage, the pressure level was modulated among 0, 25, and -20 mBar to "coax" the cell membrane into forming a gigaseal. This coaxing process was developed from our manual patching experiments in which alternating the pipette pressure among 0, 25, and -20 mBar led to a gigaseal formation for some of the trials that seemed to be failing (with the pipette resistance increasing very slowly or becoming stagnant following the suction and hyperpolarization), and it was required for 8 out of 42 gigaseals when targeting PV-positive neurons (in 16 PV-Cre x Ai14 mice) and for 4 out of 19 gigaseals when targeting CaMKIIα-positive neurons (in 10 CaMKIIα-Cre x Ai14 mice) during the imagepatching algorithm validation. If more than 5 minutes were needed for the pipette resistance to exceed a gigaohm, then the pipette was retracted from the brain to start a new trial. Otherwise, the pipette resistance was continuously recorded until it reached a stable value, not increasing by more than 15% over 10 seconds (see Figure S2.2, "gigaseal formation," for details).

The break-in process was developed based on a combination of previous developed protocols (Häusser and Margrie, 2014; Komai et al., 2006; Margrie et al., 2003) and our experience with manual patching. Three consecutive pulses of suction were applied, with each pulse increasing in suction from 0 mBar to -25 mBar at -20 mBar/s and then returning to 0 mBar. These suction pulses were repeatedly applied every 5 seconds until the whole-cell configuration was verified with both visual (i.e., the target cell being filled with the pipette dye, indicated by an increase of at least 15% in the mean pixel intensity inside the patched cell boundary in the pipette dye channel) and electrical (i.e., resistance recorded < 300 MΩ) indications. If the whole-cell state could not be achieved after three consecutive pulses, the suction endpoint was lowered by 25 mBar, and suction pulses were again applied to the cell. If a suction endpoint lower than -350 mBar had to be applied, the pipette was retracted to start a new trial. With this algorithm, we were able to achieve the whole-cell configuration successfully from a gigaseal ~57% of the time when targeting PV-positive neurons (n = 24 out of 42 gigaseals in 16 PV-Cre x Ai14 mice) and ~68% of the time when targeting CaMKIIα-positive neurons (n = 13 out of 19 gigaseals in 10 CaMKIIα-Cre x Ai14 mice) during the imagepatching algorithm validation, where a successful whole-cell state is defined as that with less than 500 pA of leakage current when held at -65 mV in voltage-clamp mode.

Derivation of dye-ejection based pipette blockage test

We derived an algorithm for determining the amount of dye being ejected at the pipette tip, which indicates the pipette quality (Komai et al., 2006), from test images of clean and contaminated pipettes inside the somatosensory and motor cortices of anesthetized PV-Cre x Ai14 mice (3 mice). We used 12 pipettes, angled at ~30° below the horizontal, positioned ~150 – 200 μm deep inside the brain, applying ~300 mBar at the tip, to obtain test images (17x zoom),

from which characteristic features were analyzed. We captured images of these pipettes both outside the brain (at ~6 – 8 mBar to make the pipette tip visible) and inside the brain (at ~300 mBar, right after entering the brain at ~600 μm/s). Out of 12 pipettes, 7 were "clean", clearly showing the dye being ejected at the tip, while the rest were occluded. By comparing these two groups, we found that all of the images capturing a clean pipette possessed either or both of the following characteristics: (i) the maximum pixel intensity of the image captured inside the brain was at least 2 times higher than the maximum pixel intensity of the image captured outside the brain; (ii) the maximum pixel intensity of the image captured inside the brain was at least as high as the maximum pixel intensity of the image captured outside the brain, and the median of the pixel intensities of the image captured inside the brain was at least 40% of the maximum pixel intensity of the image captured inside the brain. In contrast, none of the blocked pipette images showed the above characteristics. We thus decided to use conditions (i) and (ii) for the pipette tip quality check during the imagepatching operation.

Quantification of PV-positive and CaMKIIα-positive cell densities.

Z-stacks of two-photon images (each z-stack with five 223.5 x 223.5 μm^2 images and 10 μm step between consecutive images) were acquired at a depth of ~100 – 250 μm in somatosensory or motor cortex of anesthetized PV-Cre x Ai14 mice or CaMKIIα-Cre x Ai14 mice. One or more z-stacks were acquired per mouse, with each stack at different depth and lateral location within the craniotomy. Cells expressing tdTomato were counted manually from each of the z-stacks and then scaled to give the number of cells in a volume of 200 x 200 x 100 μm^3.

Input resistance and spontaneous firing rates of imagepatched cells.

Input resistance (Figure S2.4D) of an imagepatched cell was determined by repeatedly injecting a hyperpolarizing current pulse (-100 pA, 1 second long) to the cell right after achieving the whole-cell configuration, then calculating the average of membrane voltage over two 100 ms periods (one right before current injection and another at the end of current injection), and finally dividing the absolute value of the difference between the average values of two 100 ms periods by 100 pA. Spontaneous firing rate (Figure S2.4E) of an imagepatched cell was determined by calculating the frequency of action potentials about 4 to 5 minutes after break-in over a period of one minute.

2.6.3. Quantification and statistical analysis

The statistical details for comparing the recording quality metrics between the imagepatched and fully manually patched PV-positive neurons (Figures S2.4A-S2.4C) are provided in the Results section. The p-values associated with the Student's t-Test were calculated using *ttest()* function in Excel 2013, with *Tails* parameter = 2 for two-tailed distribution and *Type* parameter = 3 for two-samples with unequal variance.

2.6.4. Data and software availability

The Imagepatcher software and the user guide are included as Methods S1 in Suk et al., 2017.

2.7. Supplemental information

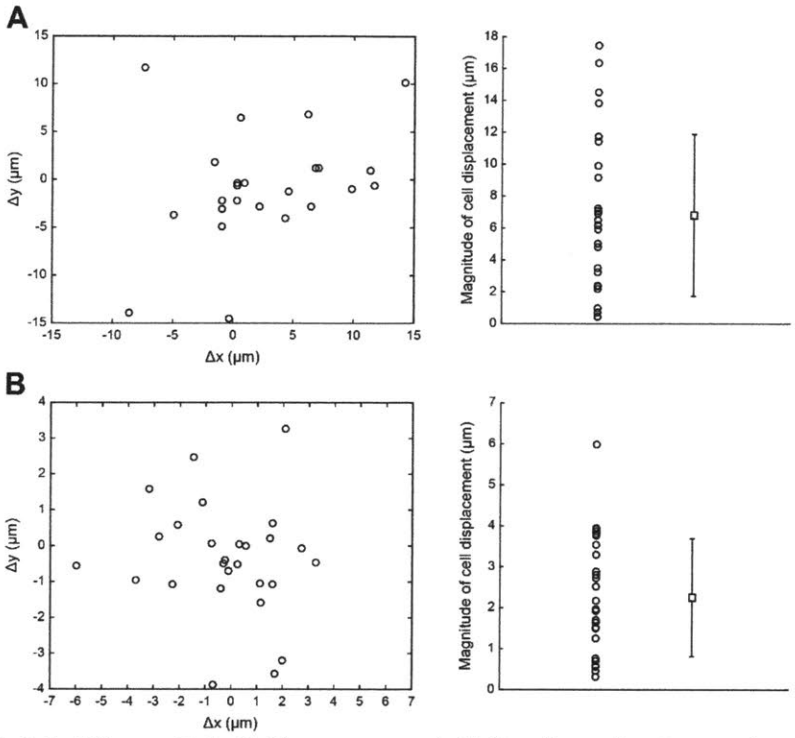

Figure S2.1, related to Figure 2.1. Cell movements following pipette navigations into the brain.

(A-B) Target cell displacements in the transverse plane (left) and their magnitude (right), following pipette navigations into the brain. Δx, change in the x coordinate of the target cell centroid, with a positive value corresponding to a cell movement to the right relative to the original location; Δy, change in the y coordinate of the target cell centroid, with a positive value corresponding to a cell movement in the anterior direction relative to the original location. Each circle represents a movement of a single cell, while squares and error bars are mean ± standard deviation.

(A) Target cell movements following pipette navigation along a linear trajectory parallel to the pipette axis (n = 25 cells in 6 anesthetized mice), with the pipette moving from above the brain surface to cortical layer 2/3.

(B) Target cell movements following pipette navigation in the x, y, and z directions (n = 27 cells in 17 anesthetized mice), with the pipette moving from a point 20 – 30 μm away from the target cell centroid to a point 10 – 20 μm directly above the target cell centroid.

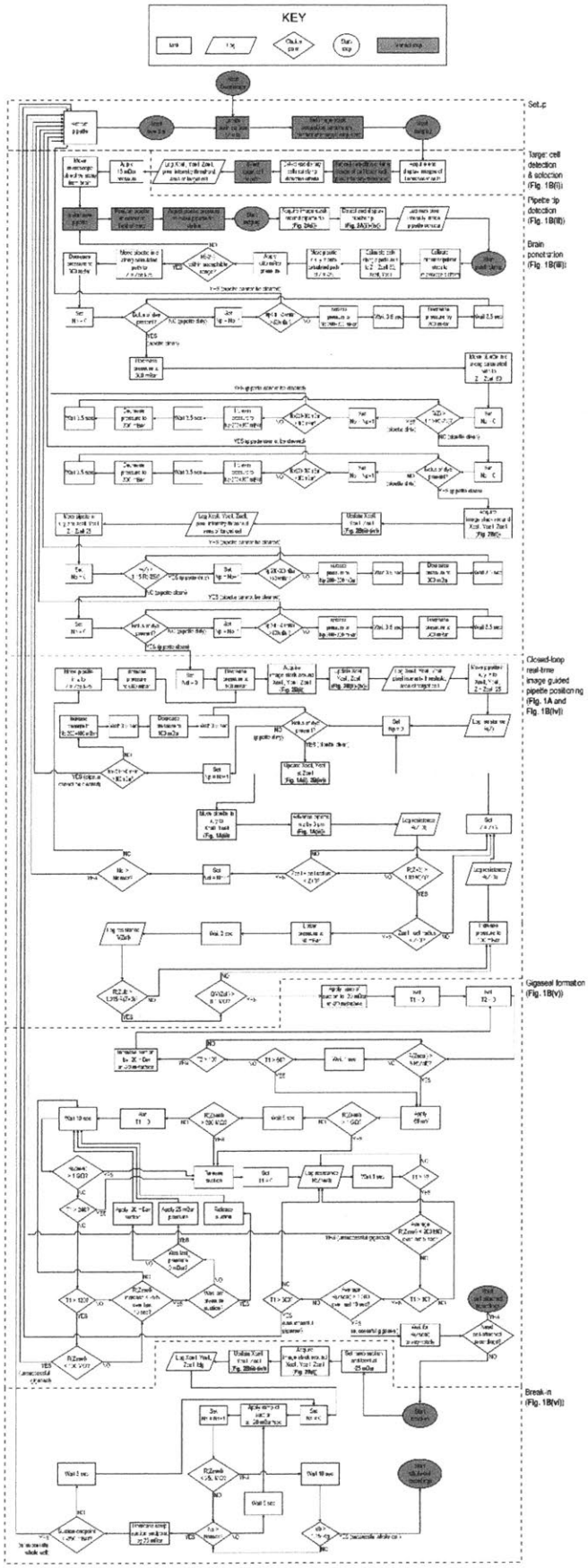
KEY
Set-up
Target cell detection & selection (Fig. 1B(i))
Pipette tip detection (Fig. 1B(ii))
Brain penetration (Fig. 1B(iii))
Closed-loop real-time image guided pipette positioning (Fig. 1A and Fig. 1B(iv))
Gigaseal formation (Fig. 1B(v))
Break-in (Fig. 1B(vi))

Figure S2.2, related to Figure 2.1. Step-by-step flowchart, showing the entire imagepatching process.

Dotted lines frame each of the stages of the algorithm; within the dotted line frames, symbols represent task, logging, and choice points, along with text explaining the individual steps and consequences of each decision (see "**KEY**" for definition of symbols). Abbreviations: Z, depth inside the brain, in microns (with more positive Z values indicating deeper positions inside the brain); Zcell, depth of the target cell, Xcell, x-coordinate of the target cell centroid at Zcell; Ycell, y-coordinate of the target cell centroid at Zcell; x, movement direction along the x-axis of the 4-axis manipulator; y, movement direction along the y-axis of the 4-axis manipulator; z, movement direction along the z-axis of the 4-axis manipulator; d, movement direction along the diagonal axis (i.e., axis parallel to the pipette) of the 4-axis manipulator; R(Z), pipette resistance at depth Z; Np, counter for the pipette clearing pressure pulse; Ncl, total number of times the closed-loop is run; Nclmax, limit on the number of times the closed-loop is run; Zcll, depth at which pipette pressure is lowered to 30 mBar; R(Zcll), pipette resistance at Zcll; HBM(Zcll), amount of heartbeat modulation at Zcll; R(Zseal), pipette resistance at the depth at which a gigaseal and the whole-cell state are being achieved, which will vary over time as the algorithm progresses; T1, time, in seconds; T2, time, in seconds; Ns, total number of times a suction pulse is applied for break-in; Nsmax, limit on the number of times a suction pulse is applied for break-in; Id, mean pixel intensity inside the target cell contour, in the microscope channel corresponding to the pipette dye; Idg, Id when R(Zseal) is higher than 1 GΩ; Idb, Id when R(Zseal) is less than 250 MΩ.

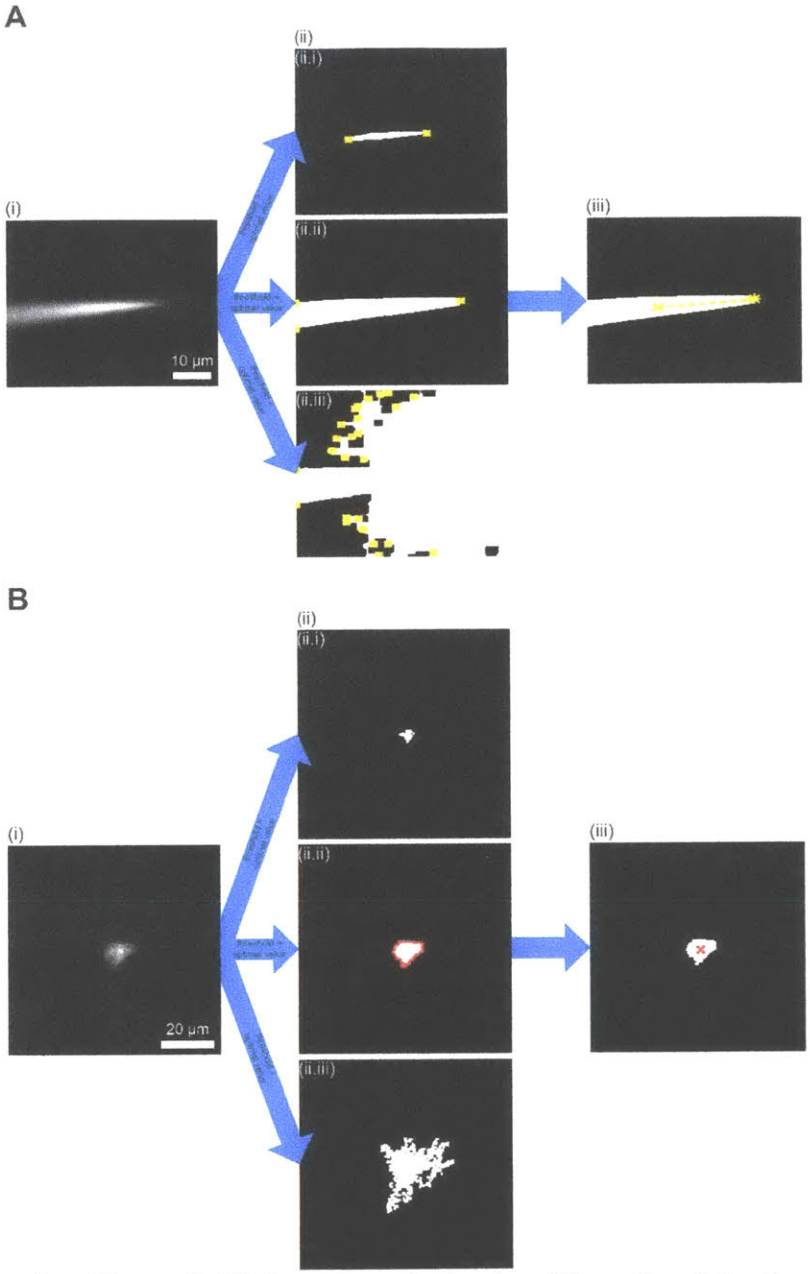

Figure S2.3, related to Figure 2. 2D image analysis algorithms for detecting pipette tips and cell centroids.

(A) Steps used to detect the tip of a fluorescent dye filled patch pipette from an image focused on the pipette tip. (i) An image of the pipette at the z-coordinate of the pipette tip (i.e., an image focused on the pipette tip) is filtered using a 2D Gaussian filter. (ii) Threshold values corresponding to 5 – 75% of the maximum pixel intensity of the filtered image are applied to the filtered image, and the resulting clusters (white) are subjected to MATLAB's endpoint detection function (bwmorph function with 'endpoints' operation) to identify the endpoints (yellow boxes). Clusters and endpoints resulting from threshold values corresponding to 75 (ii.i), 13 (i.e., optimal threshold value; ii.ii), and 3% (ii.iii) of the filtered image's maximum pixel intensity are shown as examples. (iii) The cluster resulting from the optimal threshold value is analyzed to locate its centroid (yellow x) and extrapolate a line from the centroid in the direction of the pipette angle

(yellow dotted line). The pixel in the cluster that is closest to the endpoint of the extrapolated line (i.e., endpoint opposite to the centroid) is designated as the pipette tip (yellow star).
(B) Steps used to detect the cell boundary and centroid from each image in a z-stack acquired around a fluorescent cell. (i) An image in a z-stack acquired around a tdTomato-expressing cell is filtered using a 2D Wiener filter. (ii) Threshold values corresponding to 5 – 95% of the maximum pixel intensity of the filtered image are applied to the filtered image, and the resulting clusters (white) are analyzed to determine their areas (i.e., numbers of pixels in the clusters). The cluster whose area is the closest to that of the cell chosen by the user during the target cell detection and selection stage ((ii.ii), white) is further processed to determine its boundary ((ii.ii), red outline). Clusters resulting from threshold values corresponding to 50 (ii.i), 20 (i.e., optimal threshold value; ii.ii), and 3.5% (ii.iii) of the filtered image's maximum pixel intensity are shown as examples. (iii) The cluster obtained by applying the optimal threshold value to the filtered image is processed to yield its centroid (red x), designated as the centroid of the cell in the image.

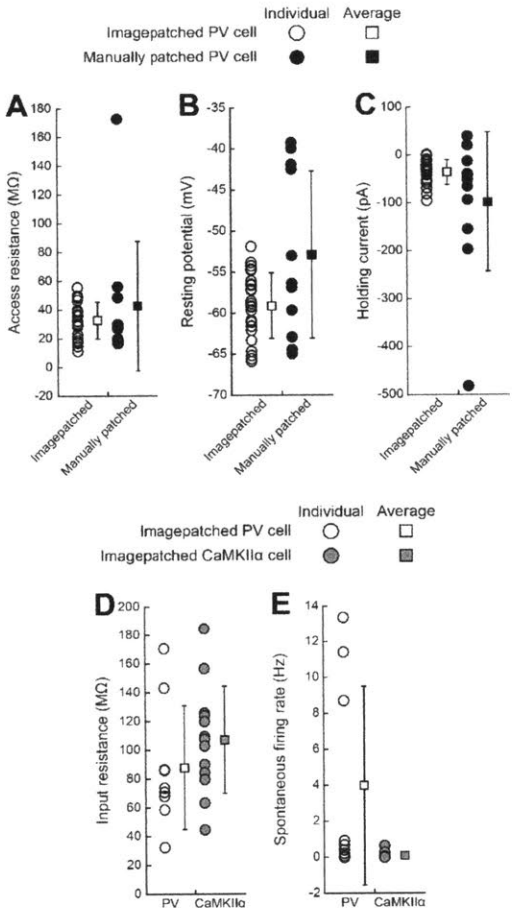

Figure S2.4, related to Figure 2.4. Recording quality and electrophysiological properties of imagepatched neurons.

(A-C) Recording quality of imagepatched (white symbols; n = 24 cells from 14 mice) vs manually patched (black symbols; n = 11 cells from 8 mice) tdTomato-expressing PV-positive interneurons in somatosensory and motor cortices of isoflurane-anesthetized PV-Cre x Ai14 mice. Squares and error bars are mean ± standard deviation.

(A) Access resistance.

(B) Resting potential.

(C) Holding current.

(D-E) Electrophysiological properties of imagepatched tdTomato-expressing PV-positive neurons (white symbols; 9 cells from 5 PV-Cre x Ai14 mice) and imagepatched tdTomato-expressing CaMKIIα-positive neurons (gray symbols; 13 cells from 7 CaMKIIα-Cre x Ai14 mice) in somatosensory and motor cortices of isoflurane-anesthetized mice. Squares and error bars are mean ± standard deviation.

(D) Input resistance.

(E) Spontaneous firing rate.

Failure Modes	PV	CaMKIIα
Pipette Blockage	20.4% (n = 22)	21.5% (n = 14)
Failed Gigaseal Formation	37.0% (n = 40)	43.1% (n = 28)
Loss of Seal During Break-in	16.7% (n = 18)	9.2% (n = 6)
Untargeted Patch	3.7% (n = 4)	6.2% (n = 4)

Table S2.1, related to Figure 2.4. Four failure modes of the imagepatcher.
Imagepatching attempts that did not result in successful whole-cell recordings (84 out of 108 attempts targeting PV-positive neurons, from 17 PV-Cre x Ai14 mice; 52 out of 65 attempts targeting CaMKIIα-positive neurons, from 10 CaMKIIα-Cre x Ai14 mice) can be grouped into 4 failure modes: (i) 'pipette blockage' includes imagepatching attempts in which a pipette failed to eject enough dye at its tip or experienced a significant rise in its resistance value after entering the brain or while approaching the target cell; (ii) 'failed gigaseal formation' includes imagepatching attempts in which contact between an uncontaminated pipette tip and the target cell membrane, followed by pipette pressure modulation and hyperpolarization, did not result in a gigaseal; (iii) 'loss of seal during break-in' includes imagepatching attempts in which application of suction pulses following successful gigaseal formation led to a loss of gigaseal or cell lysis; and (iv) 'untargeted patch' includes imagepatching attempts in which an unlabeled cell (i.e., a cell that was not fluorescently tagged), sitting right on top of a targeted cell, was patched instead of the target cell.

Target Cell Depths Below The Brain Surface	Success Rates			
	PV		CaMKIIα	
	Gigaseal	Whole-cell	Gigaseal	Whole-cell
≥100 and <200 μm	50.0% (n = 24 out of 48)	29.2% (n = 14 out of 48)	40.0% (n = 14 out of 35)	25.7% (n = 9 out of 35)
≥200 and <300 μm	48.6% (n = 18 out of 37)	27.0% (n = 10 out of 37)	31.3% (n = 5 out of 16)	25.0% (n = 4 out of 16)

Table S2.2, related to Figure 2.4. Success rates at different target cell depths, for trials that entered the closed-loop stage of imagepatching.
One unsuccessful attempt targeted a PV-positive cell at a depth below 300 μm and is not included in the table.

PV			CaMKIIα		
Number of Labeled Cells in 200 x 200 x 100 μm³ Volume	**Success Rates**		**Number of Labeled Cells in 200 x 200 x 100 μm³ Volume**	**Success Rates**	
	Gigaseal	**Whole-cell**		**Gigaseal**	**Whole-cell**
<6	42.1% (n = 8 out of 19)	31.6% (n = 6 out of 19)	<20	40.0% (n = 4 out of 10)	30.0% (n = 3 out of 10)
≥6 and <10	57.1% (n = 16 out of 28)	32.1% (n = 9 out of 28)	≥20 and <35	30.8% (n = 4 out of 13)	15.4% (n = 2 out of 13)
≥10 and <14	33.3% (n = 8 out of 24)	20.8% (n = 5 out of 24)	≥35 and <65	47.1% (n = 8 out of 17)	35.3% (n = 6 out of 17)
≥14	66.7% (n = 10 out of 15)	26.7% (n = 4 out of 15)	≥65	27.3% (n = 3 out of 11)	18.2% (n = 2 out of 11)

Table S2.3, related to Figure 2.4. Success rates for different labeling densities of cells around a target cell, for trials that entered the closed-loop stage of imagepatching.
The number of labeled cells around a target cell in a 200 x 200 x 100 μm³ volume was determined by scaling the number of tdTomato-expressing cells in a z-stack (5 images, 10 μm step size, field of view of 223.5 x 223.5 μm²) that captured the target cell near the center of its field of view.

Chapter 3: Using the autopatcher as a validation tool for temporal interference brain stimulation[2]

3.1. Introduction

Physical means of brain stimulation, such as the use of implanted electrodes for deep brain stimulation (DBS), have led to widespread excitement about the possibility of repairing neural dysfunction through direct control of brain circuit dynamics, including multiple FDA-approved therapies for previously intractable brain disorders (Greenberg et al., 2010; Kalia et al., 2013). Electrical stimulation via implanted electrodes sparsely activates distributed sets of neurons (Histed et al., 2009), in a fashion different from direct optogenetic control of local cells (Gradinaru et al., 2009). The impact of electromagnetic stimulation on brain circuitry is an emergent function of the fields applied, the excitability properties of the neurons themselves, and the configuration of the neural network in which they are embedded (Merrill et al., 2005). As a result of this complexity, physical means of brain stimulation are often used in a phenomenological way, especially because the excitability properties of neurons vary across different cell types, and thus understanding how a given brain stimulation method impacts a given brain function may require analyzing many factors.

However, some properties of neurons are likely universal — for example, the intrinsic low-pass filtering of electrical signals by the neural membrane (Hutcheon and Yarom, 2000), which prevents neural electrical activity from following very high-frequency oscillating (e.g., ≥ 1 kHz) electric fields. Here, we explore whether the biophysics underpinning such a potentially universal property might support novel strategies for electrical brain stimulation. In particular, if we apply high-frequency oscillating electric fields at multiple sites outside the brain, neurons in the brain will not be able to follow these high-frequency fields directly. However, if two such electric fields are applied at high frequencies that differ by a small amount, which corresponds to a low frequency that neurons can follow, neurons in the brain may be able to demodulate and follow the envelope modulation that results from the temporal interference between these two applied fields, and which oscillates at the difference frequency. If the amplitude of the envelope modulation reaches a maximum at a site deep in the brain, it might be possible to drive deep-lying neurons without recruiting overlying ones. We here test this concept, which we call temporal interference (TI) stimulation, by measuring electrophysiological responses from stimulated neurons *in vivo* using the autopatcher (Kodandaramaiah et al., 2012, 2016). We demonstrate that, while cortical and hippocampal neurons in the intact mouse brain do not respond to high frequency (1 kHz, 2 kHz) electric fields themselves, they can be activated by TI stimulation, with their firing rate closely mirroring the frequency difference between two high frequency electric fields used in TI.

3.2. Results

We first set out to examine whether the TI concept could indeed result in well-defined low-frequency envelope modulated electric fields. In the TI concept (Figure 3.1A), electric

---

[2] The contents of this chapter have been published in *Cell* (https://doi.org/10.1016/j.cell.2017.05.024).

currents are applied at high frequencies f_1 and $f_2 = f_1 + \Delta f$ that fall outside the range of normal neural operation, but which differ by a small amount, Δf, that falls within the frequency range that neurons can respond to. The superposition of the two electric fields inside the brain results in an electric field at a frequency of $(f_1 + f_2)/2$, whose envelope is modulated at the frequency Δf (Figure 3.1B). The amplitude of the envelope modulation at a particular location depends on the vectorial sum of the two applied field vectors at that point and as a result can have a maximum at a point distant from the electrodes, potentially even deep in the brain (Figure 3.1C). The location of this envelope maximum depends on the electrode configuration, as well as properties of the applied waveforms. For the trapezoidal configuration shown in Figure 3.1A, the low-frequency envelope oscillates at a frequency of 40 Hz, with waveforms in Figure 3.1B plotted at the two specific points highlighted by Roman numerals in Figure 3.1A. For example, Figure 3.1Bi shows a large envelope modulation amplitude at a location where the two fields are large and aligned, whereas Figure 3.1Bii shows a small envelope modulation amplitude at a location where the two fields are less aligned.

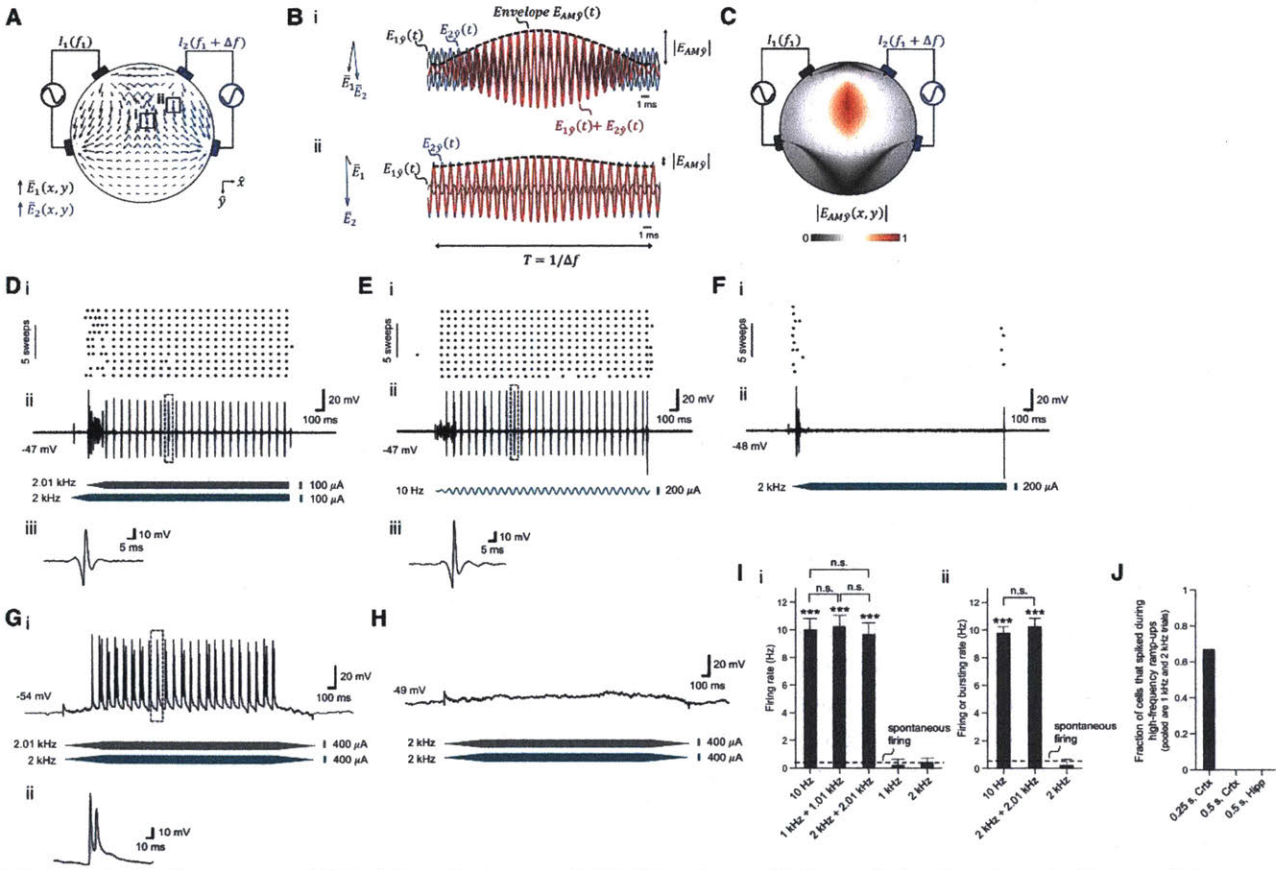

Figure 3.1. Concept of TI Stimulation and Validation of Neural Activation in Intact Mouse Brain.

(A–C) TI concept.

(A) Electric field vectors $\overline{E}_1(x, y)$ and $\overline{E}_2(x, y)$ (gray and blue arrows respectively) resulting from alternating currents I_1 and I_2 simultaneously applied to the scalp of a simplified head model (simulated as a cylinder filled with saline). I_1 and I_2 are applied at kHz frequencies f_1 (1 mA at 1 kHz in this example, applied across the gray electrodes) and f_2 (1 mA at 1.04 kHz, across the blue electrodes) that are higher than the range of frequencies of normal neural operation, so that

neurons are driven only at the difference frequency. Field amplitudes were normalized to maximum. The field vectors are taken at a time point in which the two currents were applied in-phase from top to bottom electrodes.

(B) Magnified views of the electric field vectors $\overline{E}_1$ and $\overline{E}_2$ (again normalized to maximum) in the regions indicated by boxes in A and indicated by Roman numerals (*left*), with plots (*right*) of time-domain sinusoidal waveforms of the electric field amplitudes $E_{1\hat{y}}(t)$ (gray) and $E_{2\hat{y}}(t)$ (blue) along the $\hat{y}$ direction, as well as the envelope resulting from the superposition of the two fields, i.e., $E_{1\hat{y}}(t) + E_{2\hat{y}}(t)$ (red). $E_{AM\hat{y}}(t)$ is the envelope modulation waveform along the $\hat{y}$ direction (black dashed line).

(C) Color map (normalized to maximum) of the spatial distribution of the envelope modulation amplitude along the $\hat{y}$ direction (as plotted for two points in B), for the modeled configuration shown in A.

(D–J) TI effects on neural activity, assessed with in vivo whole cell patch clamp in anesthetized mouse.

(D–F) Representative neural responses from a single patched neuron in the somatosensory cortex undergoing TI stimulation (D) (gray waveform, stimulation at 2.01 kHz, 100 μA amplitude, 0.25 s ramp-up, 1.75 s duration, 0.25 s delay; blue waveform, 2 kHz, 100 μA amplitude, 0.25 s ramp up, 2 s duration, no delay), 10 Hz stimulation (E) (blue waveform, 10 Hz, 200 μA amplitude, 0.25 s ramp-up period, 2 s duration) and high-frequency stimulation (F) (blue waveform, 2 kHz, 200 μA amplitude, 0.25 s ramp-up, 2 s duration). Showing (i) spike raster plots, (ii) traces of current-clamp recording and (iii) magnified views of the trace regions indicated by boxes in (ii). Traces were filtered using a fifth-order Butterworth band-stop filter with cutoff frequencies of 1 kHz and 15 kHz and with a third order Butterworth high-pass filter with a cutoff frequency of 100 Hz to remove 10 Hz and 2 kHz stimulation artifacts; see Figures S3.1A–S3.1I for non-filtered traces.

(G and H) Representative neural responses from a single patched neuron in hippocampus undergoing TI stimulation (G); gray waveform, stimulation at 2.01 kHz, 400 μA amplitude, 0.5 s ramp-up, 2 s duration, 0.5 s ramp-down; blue waveform, 2 kHz, 400 μA amplitude, 0.5 s ramp up, 2 s duration, 0.5 s ramp-down; shown are (i) traces of current-clamp recording and (ii) magnified views of the trace regions indicated by boxes in (i) and high-frequency stimulation (H); gray waveform, 2 kHz, 400 μA amplitude, 0.5 s ramp-up, 2 s duration, 0.5 s ramp-down; blue waveform, 2 kHz, 400 μA amplitude, 0.5 s ramp-up, 2 s duration, 0.5 s ramp-down). Traces were filtered using a fifth order Butterworth band-stop filter with cutoff frequencies of 1 kHz and 15 kHz to remove 2 kHz stimulation artifacts.

(I) Spike frequency in neurons undergoing stimulation, as assessed by whole patch clamp in anesthetized mice (plotted are mean ± SD). (i) Neurons in somatosensory cortex, from left to right: 10 Hz stimulation (200 μA, n = 7 cells from 4 mice), TI stimulation with 1 kHz + 1.01 kHz (current sum 200 μA, n = 6 cells from 2 mice), TI stimulation with 2 kHz + 2.01 kHz (current sum 200 μA, n = 7 cells from 3 mice), 1 kHz stimulation (200 μA, n = 5 cells from 2 mice), 2 kHz stimulation (200 μA, n = 6 cells from 3 mice). (ii) Neurons in hippocampus, from left to right: stimulation with two sinusoids at 10 Hz (current sum 714 ± 367 μA mean ± SD, n = 6 cells from 3 mice), TI stimulation with 2 kHz + 2.01 kHz (current sum 733 ± 100 μA, n = 8 cells from 4 mice), stimulation with two sinusoids at 2 kHz (current sum 880 ± 178 μA, n = 5 cells from 3 mice). Dashed lines, mean spontaneous firing rate; stimulation duration, ~2 s; *** indicates $p < 1.0E-20$ for comparison of mean firing rate of a condition versus mean spontaneous firing rate, and n.s. indicates no significant difference between indicated conditions, for post hoc tests

following one-way ANOVA with factor of stimulation condition; see Table S3.1 for full statistics from cortical and hippocampal recordings. See Figures S3.1J and S3.1K for traces at different currents for the conditions corresponding to (G)–(H).
(J) Fraction of cells that transiently spiked during the high-frequency stimulation ramp-ups (pooled together are 1 kHz with no TI and 2 kHz with no TI); '0.25 s, Crtx', ramp-up period 0.25 s, neurons in cortex, n = 6 cells from 2 mice; '0.5 s, Crtx', ramp-up period 0.5 s, neurons in cortex, n = 6 cells from 3 mice; '0.5 s, Hipp', ramp-up period 0.5 s, neurons in hippocampus, n = 5 cells from 3 mice.

To assess whether such low-frequency field envelopes could effectively drive neural spiking activity, we applied TI stimulation transcranially to anesthetized living mice, and recorded the responses by using automated whole-cell patch clamp neural recording. Currents were applied via two electrodes on the skull (with a ~0.5 mm gap between their edges), and recordings were made in the somatosensory cortex. We found that interferential stimulation with two sinusoids at 2.01 kHz and 2 kHz, resulting in a Δf envelope frequency of 10 Hz, was able to recruit neurons to fire at 10 Hz (Figure 3.1D), as efficaciously as direct 10 Hz stimulation (Figure 3.1E) that would be expected to broadly affect neural activity (Miranda et al., 2013). High-frequency stimulation (with one sinusoid at 2 kHz and no TI) did not result in activity (Figure 3.1F), beyond a brief transient associated with the beginning of stimulation in some cells (n = 4 out of 6 cells from 2 mice) when 0.25 s sinusoidal ramp-up times were used. When 0.5 s ramp-up times were used, no such transient activity was observed in any cells (n = 5 cells from 2 mice), suggesting that the transient spiking activity observed earlier was due to the speed of the 0.25 s duration ramp-up (Figure 3.1J). We validated TI stimulation on a population of cortical cells (Figure 3.1Ii) and found that interferential stimulation with a difference frequency of 10 Hz resulted in spike frequencies of 10.21 ± 0.83 Hz (mean ± SD), for a 1 kHz carrier frequency (n = 6 cells from 2 mice) and 9.68 ± 0.85 Hz for a 2 kHz carrier frequency (n = 7 cells from 3 mice; see Table S3.1 for full statistics associated with Figure 3.1Ii).

To validate whether neuronal firing can be manipulated at different depths in tissue, we performed automatic patch clamp recording in the mouse hippocampus. Currents were applied via two electrodes that were located on the skull, with proximal edges 1.5–2 mm apart. We found that interferential stimulation (with two sinusoids at 2.01 kHz and 2 kHz, resulting in a Δf envelope frequency of 10 Hz) was able to recruit neural firing in synchronization with the envelope—with either single spikes (n = 3 cells from 2 mice) or brief bursts of spikes (n = 5 cells from 3 mice; a burst was defined as a < 50 ms spiking event with inter-spike interval ≤ 15 ms; 1.3 ± 0.37 mean spikes per burst ± SD; 9.07 ± 3.2 ms inter-spike interval) elicited by the TI stimulation (in detail: mouse 1 had one cell with a burst response; mouse 2 had two cells with single spike responses; mouse 3 had two cells with a burst response; mouse 4 had two cells with a burst response and one cell with a single spike response) (Figure 3.1G). Direct application of high-frequency stimulation (with two sinusoids on the two electrodes, both at 2 kHz) did not result in activity (Figure 3.1H). No spiking transient was observed because we used the slower, 0.5 s duration ramp-up that we had previously observed to eliminate this transient (Figure 3.1J; n = 5 cells from 3 mice). We found (Figure 3.1Iii) that interferential stimulation with a difference frequency of 10 Hz resulted in spike or burst occurrence frequencies of 10.23 ± 0.61 Hz for a 2 kHz carrier frequency (n = 8 cells from 4 mice; see Table S3.1 for full statistics associated with Figure 3.1Iii). The timing of the spikes or the first spikes of bursts, relative to the peak of the TI

envelope, was −2.8 ± 4.8 ms, i.e., when the envelope amplitude was >97% of its peak amplitude, which was not different from the timing of spikes evoked by 10 Hz stimulation relative to the 10 Hz sinusoid peak (−1.3 ± 2.2 ms; pairwise t test, p = 0.47).

The membrane potential of neurons undergoing TI stimulation repolarized between single spikes, or between brief bursts of spikes, to the baseline membrane potential (cortex, −10.36 ± 27.84 mV, mean difference from baseline ± SD; p = 0.74, pairwise t test; n = 13 cells from 5 mice; hippocampus, 5.5 ± 7.89 mV; p = 0.34; n = 8 cells from 4 mice). The spike frequency during the 20th bout of TI stimulation (tested in three cells in the somatosensory cortex from one mouse; 2 s stimulation followed by 2 s rest) was 9.93 ± 0.2 Hz (mean ± SD), not different from the spike frequency during the 1st bout (p = 0.95; pairwise t test), and the spike amplitude during the 20^{th} bout of TI stimulation was not different from the spike amplitude during the first bout (5.3 ± 3.5 mV, mean amplitude difference ± SD; p = 0.75, pairwise t test); see Figures S3.1L–S3.1N for representative traces. The membrane potential of neurons undergoing high-frequency stimulation (with two sinusoids on the two electrodes, both at 2 kHz or at 1 kHz) in both the cortex and the hippocampus was not different from the baseline membrane potential before the stimulation (cortex, 1.67 ± 4.87 mV, mean difference from baseline ± SD, measured 1 s after stimulation onset; p = 0.66, pairwise t test; n = 11 cells from 5 mice; hippocampus, −1.7 ± 5.39 mV; p = 0.91; n = 5 cells from 3 mice).

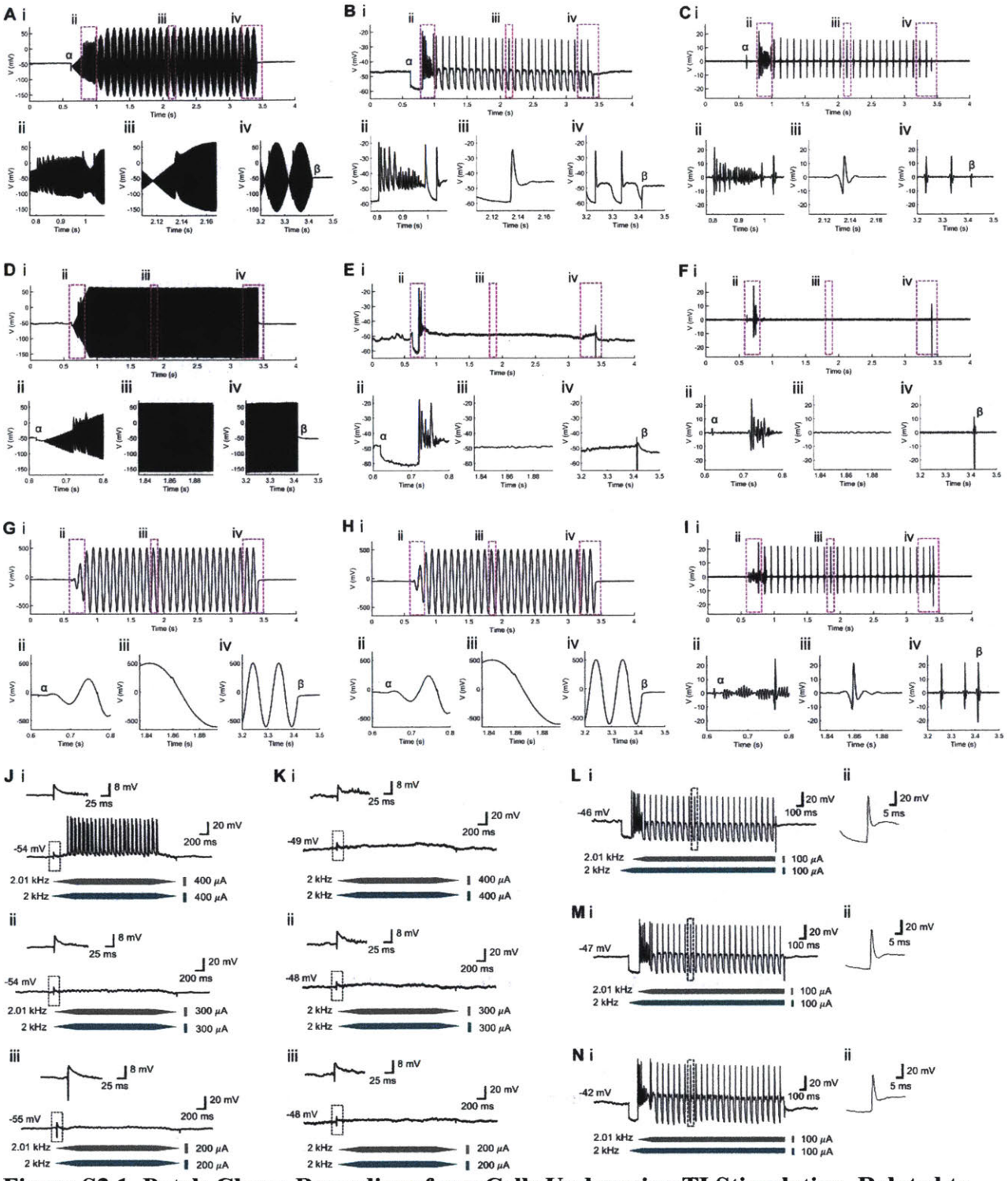

Figure S3.1. Patch-Clamp Recordings from Cells Undergoing TI Stimulation, Related to Figure 3.1.

(A) to (I) Removal of artifacts from current-clamp recordings as in Figure 3.1. (i) Trace of current-clamp recording, with (ii–iv) magnified views of the regions indicated by boxes in (i); α, artifact caused by connecting stimulation and recording grounds ($I_1 = I_2 = 0$ at this point); β,

artifact caused by disconnecting stimulation and recording grounds (I_1 and I_2 are forced to zero at this point).
(A) to (C) TI stimulations as in Figure 3.1D (I_1, 2.01 kHz, 100 μA amplitude, 0.25 s ramp-up, 1.75 s duration, 0.25 s delay relative to I_2; I_2, 2 kHz, 100 μA amplitude, 0.25 s ramp up, 2 s duration).
(A) Raw recording trace.
(B) Trace of (A), filtered using a fifth order Butterworth band-stop filter with cutoff frequencies of 1 kHz and 15 kHz.
(C) Trace of (B), further filtered using a third order Butterworth high-pass filter with a cutoff frequency of 100 Hz; this is the trace shown in Figure 3.1D.
(D–F) Are as in (A)–(C) but for the case of Figure 3.1F (I_1, 2 kHz, 200 μA amplitude, 0.25 s ramp-up, 2 s duration).
(G–I) Are as in (A)–(C) but for the case of Figure 3.1E (I_1, 10 Hz, 200 μA amplitude, 0.25 s ramp-up period, 2 s duration); ringing in (Iii) is filtering distortion due to the Gibbs phenomenon.
(J and K) Representative neural responses from a single patched neuron in the hippocampus, the neuron of Figures 3.1G and 3.1H, undergoing TI stimulation (J); gray waveform, stimulation at 2.01 kHz; blue waveform, 2 kHz) or high-frequency stimulation (K); gray waveform, 2 kHz; blue waveform, 2 kHz) with current amplitude of (i) 400 μA; (ii) 300 μA; (iii) 200 μA. The stimulation order was (iii), (ii), (i) with 2 s intervals between consecutive stimulations. Trace regions containing artifacts caused by connecting stimulation and recording devices (i.e., before current amplitudes are ramped up) are indicated by boxes, with magnified views shown above the boxes.
(L–N) Representative neural responses from a single patched neuron in the anesthetized mouse somatosensory cortex undergoing repeated TI stimulation (gray waveform, stimulation at 2.01 kHz, 100 μA amplitude, 0.25 s ramp-up, 1.75 s duration, 0.25 s delay relative to blue waveform; blue waveform, 2 kHz, 100 μA amplitude, 0.25 s ramp up, 2 s duration, no delay) with 2 s intervals between repetitions. (i) Neural response trace, (ii) magnified view of region indicated by a box in (i).
(L) Representative trace from the first stimulation period.
(M) Representative trace from the 10th stimulation period.
(N) Representative trace from the 20th stimulation period. To remove stimulation artifacts, all traces in the figure were filtered using a fifth order Butterworth band-stop filter with cutoff frequencies of 1 kHz and 15 kHz.

Table S3.1. Interferential neural activation in intact mouse brain (Related to Figure 3.1)

Cortex

Group number	Group name	Group mean (± st.d.) firing frequency (Hz)
1	Firing rate during 10 Hz stimulation	9.97 (± 0.85)
2	Firing rate during 1 kHz + 1.01 kHz TI stimulation	10.2 (± 0.83)
3	Firing rate during 2 kHz + 2.01 kHz TI stimulation	9.7 (± 0.85)
4	Firing rate during 1 kHz stimulation	0.2 (± 0.45)
5	Firing rate during 2 kHz stimulation	0.4 (± 0.31)
6	Spontaneous firing rate	0.35 (± 0.6)

ANOVA firing rates, cortex

Source	SS	df	MS	F	Prob>F
Groups	1122	5	224.5	502.6	2.8E-38
Error	20.1	45	0.44		
Total	1142	50			

Post-hoc multiple comparison test for neural firing rates, cortex

Group A	Group B	Mean (Group A – Group B)	95% CI (Group A – Group B)		p-value
1	2	-1.39	-0.23	0.91	1.00E+00
1	3	-0.78	0.32	1.43	1
1	4	8.56	9.77	10.98	7.79E-27
1	5	8.41	9.57	10.72	2.19E-27
1	6	8.72	9.63	10.54	6.57E-32
2	3	-0.58	0.56	1.71	1.00E+00
2	4	8.75	10.01	11.26	1.16E-26
2	5	8.61	9.8	11	3.71E-27
2	6	8.91	9.87	10.84	2.84E-31
3	4	8.23	9.44	10.66	3.25E-26
3	5	8.09	9.24	10.39	9.45E-27
3	6	8.4	9.31	10.22	2.92E-31
4	5	-1.45	-0.2	1.05	1.00E+00
4	6	-1.17	-0.13	0.9	1
5	6	-0.89	0.07	1.03	1.00E+00

Hippocampus

Group number	Group name	Group mean (± st.d.) firing frequency (Hz)
1	Firing rate during 10 Hz stimulation	9.74 (± 0.49)
2	Firing rate during 2 kHz + 2.01 kHz TI stimulation	10.22 (± 0.61)
3	Firing rate during 2 kHz stimulation	0.2 (± 0.47)
4	Spontaneous firing rate	0.45 (± 1.06)

ANOVA firing rates, hippocampus

Source	SS	df	MS	F	Prob>F
Groups	816	3	272.1	390.83	2.09E-26
Error	23.7	34	0.691		
Total	839.8	37			

Post-hoc multiple comparison test for neural firing rates, hippocampus

Group A	Group B	Mean (Group A – Group B)	95% CI (Group A – Group B)		p-value
1	2	-1.74	-0.48	0.77	1.00E+00
1	3	8.12	9.54	10.95	8.05E-19
1	4	8.17	9.26	10.36	5.93E-22
2	3	8.69	10.02	11.36	2.55E-20
2	4	8.76	9.75	10.73	3.74E-24
3	4	-1.44	-0.27	0.9	1

3.3. Discussion

In this chapter, we presented how automated *in vivo* patch clamping can help study and validate a new brain stimulation strategy, temporal interference-based non-invasive deep brain stimulation. The autopatcher facilitated the characterization of TI stimulation in multiple brain areas *in vivo*, allowing for accurate observations of responses from both cortical and hippocampal neurons in the intact mouse brain. Although the use of the autopatcher as the validation tool did not enable us to study responses from specific cell types, the automated system described in the earlier chapter (the imagepatcher) could be utilized to augment our understanding of the effect of TI on different classes of cells and what roles they may play for network-level responses to the stimulation. This chapter only presents one use case of automated patch clamping, but in principle, the autopatcher and the imagepatcher could be useful for other tools that require electrophysiological validation (e.g., optical tools that sense and visualize membrane voltages or flows of ionic current), ultimately facilitating the development of new technologies that can help us better understand the brain.

3.4. Methods

3.4.1. Experimental model and subject details

Mouse: C57BL/6
Sex: Male.
Age: 8–12 weeks old.
Source: All animals were purchased from Taconic Biosciences.
Housing and husbandry: Mice were housed in standard cages in the MIT animal facility with ad libitum food and water in a controlled light-dark cycle environment, with standard monitoring by veterinary staff.
Allocation of animals to experimental groups: Randomly assigned.
Committee approval: All animal procedures were approved by the Massachusetts Institute of Technology (MIT) Committee on Animal Care (CAC, Protocol Number: 1115-111-18), and all experiments conformed to the relevant regulatory standards.

3.4.2. Method details

Surgical Procedures

On the day of the experiment, the mice were injected with Meloxicam (1mg/kg) and buprenorphine (0.1mg/kg) and anesthetized with 1%–2% (vol/vol) isoflurane in oxygen.

Ophthalmic ointment (Puralube Vet Ointment, Dechra) was applied to the eyes. The scalp and the ventral torso were shaved and sterilized with Betadine and 70% ethanol. Two electrodes made of saline-filled polyimide tubes (Vention Medical Inc) with 1.5 mm outer diameter and 1.4 mm inner diameter or two electrodes made of adhesive electrogel with 1.5 mm diameter (SignaGel, ParkerLabs) were affixed to the skull (polyimide tubes were affixed using dental acrylic). During cortical recording, the positions of the skull electrodes relative to bregma were anteroposterior (AP) −1 mm, mediolateral (ML) −1.5 mm, and AP −1 mm, ML −2 mm; during hippocampus recording, their positions relative to bregma were: AP −2 mm, ML 0.25 mm, and AP −2 mm, ML −2.75 mm.

In Vivo Transcranial Stimulation

Transcranial stimulation was applied to anesthetized mice via the two skull electrodes, described above. Each skull electrode was paired with a cloth-base electrode (11 mm diameter conductive area; EL504, BioPac Inc) that was attached to the ventral torso with adhesive electrode gel (for the experiments of Figure 3.1D-F,Ii; SignaGel, Parker Laboratories Inc; 10-15 mm spacing between the edge of the conductive area of the torso electrodes) or with an adhesive electrode gel based electrode (SignaGel, ParkerLabs) on the cheeks (for the experiments of Figure 3.1G-H,Iii; approximately 11 mm diameter conductive area). Stimulation was applied for 1.5-2 s periods, with 0.25-0.5 s duration ramp-on periods and 0-0.5 s duration ramp-off periods, with at least a 2 s rest period between consecutive stimulations.

Whole-Cell Patch Clamp Recording

In vivo whole cell patching in current clamp mode (i.e., 0 pA holding current) was conducted in the cortex (depth of ~500 μm below the dura) and CA1 layer of the hippocampus (depth of 1131 ± 157 μm below the dura) of anesthetized mice with an autopatcher (Kodandaramaiah et al., 2012). Data were acquired using pClamp software (Molecular Devices) at a 400 kHz sampling rate. Patch electrodes were pulled from thin-walled borosilicate glass capillary tubing using a P-97 puller (Sutter Instruments). Tip electrode resistance was 4.6–7.4 MΩ in artificial cerebrospinal fluid (ACSF), containing 126 mM NaCl, 3 mM KCl, 1.25 mM NaH2PO4, 2 mM CaCl2, 2 mM MgSO4, 24 mM NaHCO3 and 10 mM glucose. The patch electrode solution consisted of (in mM) potassium gluconate 122.5, KCl 12.5, KOH-HEPES 10, KOH-EGTA 0.2, Mg-ATP 2, Na3-GTP 0.3, NaCl 8 (pH 7.35, mOsm 296), with 0.2–0.4 mg/ml biocytin added immediately before use. Capacitance, series resistance and input resistance were frequently measured throughout recording to monitor patch quality and cell health, using 10-pA hyperpolarization/depolarization square current pulses; a 300 pA ramp depolarization over 500 ms was used for AP generation.

Data Analysis

Data were analyzed using MATLAB (MathWorks). The recorded traces from each neuron were split into blocks corresponding to each trial within an experiment. Each block consisted of a single stimulation period of 1.5 −2 s duration with 1 s of baseline recorded before and after each stimulation period. To reduce stimulation artifacts for spike identification, traces were filtered using a 5th order Butterworth band-stop filter with cutoff frequencies of 1 kHz and 15 kHz and then with a 3rd order Butterworth high-pass filter with a cutoff frequency of 100 Hz (representative traces from the cortex are shown in the Supplemental Materials without filtering and after filtering with only the band-stop filter; representative traces from the hippocampus are

shown after filtering with only the band-stop filter). Single spikes were identified using a running window average that picked out depolarizations of > 40 mV above baseline, which were "peaky" (that is, exhibited amplitudes larger than the average amplitudes of the nearest 3 data points before and after, by > 0.001 mV). Consecutive spikes with inter-spike interval ≤ 15 ms, which occurred during a period of 50 ms or less, were defined as a spiking burst. Mean spiking frequency during stimulation periods (not including the ramping periods) was computed for each stimulation block and then averaged across neurons for each stimulation condition. Mean spontaneous firing rate was computed by a similar averaging of the firing rates across neurons, but for the 1 s interval before stimulation began. In the case of control 1 kHz or 2 kHz stimulation with no TI, we analyzed data from all complete blocks. Mean membrane potential was computed for a 500 ms period before the onset of 2 kHz or 1 kHz stimulation and was compared with a similar 500 ms period 1 s after stimulation onset, by dividing each period to 10 equally sized epochs and averaging across epochs. Overall, 18 neurons from 8 mice were analyzed with a minimal and maximal number of neurons per mouse of 1 and 4, respectively.

Chapter 4: Non-invasive gamma frequency sensory stimulation, a potential therapeutic for Alzheimer's disease, safely entrains the human brain

4.1. Introduction

Rhythmic activity of neuronal networks gives rise to brain waves that oscillate at frequencies ranging from about 0.05 Hz to 500 Hz in mammals (Buzsáki and Draguhn, 2004). Relatively high frequency (30 – 80 Hz) oscillations, called gamma oscillations, have been a topic of interest due to their close association with higher order cognitive functions (Engel et al., 2001; Fries, 2009; Fries et al., 2007; Singer and Gray, 1995; Wang, 2010) and their potential relevance in brain disorders (Herrmann and Demiralp, 2005; Llinás et al., 1999; Uhlhaas and Singer, 2006). Alzheimer's disease (AD), being a neurological disorder that entails substantial cognitive dysfunction, is expected to display changes in the high frequency oscillations, and indeed, several studies have revealed altered gamma band power and synchronization in AD patients compared to healthy controls (Van Deursen et al., 2008; Jelles et al., 2008; Koenig et al., 2005; Ribary et al., 1991; Stam et al., 2002; Wang et al., 2017).

Previously, we discovered that gamma frequency entrainment (i.e., enhancement of gamma oscillations in response to a periodic stimulation), induced either optogenetically or non-invasively with lights flickering at 40 Hz, can reduce amyloid load and activate microglia in the stimulated regions of the brain, effectively attenuating AD-related pathology in several AD mouse models (Iaccarino et al., 2016). We also found that another sensory stimulation, namely auditory tones repeating at 40 Hz, can induce gamma frequency entrainment, diminish amyloid load, induce glial responses, and change the vasculature in both the auditory cortex and the hippocampus of AD model mice (Martorell et al., 2019). In addition to the electrophysiological, molecular, and cellular changes, the auditory stimulation also led to improved hippocampal-dependent memory in 5XFAD mice (Martorell et al., 2019). Interestingly, we found that concurrent visual and auditory stimulation at 40 Hz, but not visual or auditory stimulation alone, could extend gamma frequency entrainment to the prefrontal cortex and induce amyloid reduction across broad cortical regions (Martorell et al., 2019). These findings suggest that gamma entrainment using sensory stimuli, which we call GENUS, can effectively attenuate AD-related pathology across multiple brain regions, which is an important feature for treating AD as the disease causes pathologic changes in many large-scale neural networks (Seeley et al., 2009; Sperling et al., 2010). However, the effect of gamma frequency sensory stimulation on the human brain, especially in terms of safety and feasibility, still needs to be studied to determine the possibility of translating the GENUS approach to AD patients.

In the healthy human brain, periodic sensory stimuli have been shown to induce robust entrainment, generating steady-state neural oscillations in the respective primary sensory areas (Herrmann, 2001; Pastor et al., 2002; Wang et al., 2015a). The steady-state oscillations have also been observed in AD patients in response to auditory clicks or tone bursts repeating at 40 Hz (van Deursen et al., 2011; Osipova et al., 2006), which suggests that gamma entrainment of the human brain using unimodal sensory stimulation is feasible. However, given the attenuation of AD-related pathology extended to multiple brain regions in AD mouse models by using concurrent 40 Hz visual and 40 Hz auditory stimulation (Martorell et al., 2019), it is important to

investigate the effect of this bimodal sensory stimulation on human subjects, which has not yet been reported to our knowledge.

Here, we developed a device that can concurrently deliver light and sound at 40 Hz, which was used to stimulate cognitively normal young and older subjects over acute and hour-long sessions. Electroencephalogram (EEG) recordings showed that our sensory stimulations could safely enhance gamma oscillations in the human brain, with concurrent visual and auditory stimulation inducing stronger and more widespread entrainment as well as synchronization at 40 Hz compared to visual or auditory stimulation alone. Our study demonstrates a safe and effective way of inducing widespread 40 Hz entrainment and synchronization in the human brain, opening up the possibility of investigating the effect of GENUS on AD-related pathology in humans.

4.2. 40 Hz sensory stimulation safely induces gamma frequency entrainment in young and older subjects

To determine the effect of 40 Hz sensory stimulation on the human brain, 32-channel EEG was recorded from each subject as they were exposed to a randomized sequence of 40 Hz visual, auditory, and bimodal stimulation, with each stimulation period preceded by a period of no stimulation (i.e., baseline period; see Methods for details). The EEG signals were closely monitored during the recording and reviewed after the recording, and no abnormal activity (e.g., sharp waves or spikes related to epileptic seizures) was observed. Subjects also did not report any adverse effects (e.g., headache, nausea, change in hearing and vision) during or after the exposure to the stimulation.

The overall frequency characteristics of the EEG signals were determined using global power spectral density (PSD), which was calculated by averaging the power spectral density across all 32 electrodes (see Methods for details). In both young and older subject groups, the global PSD showed an increase at 40 Hz for all three stimulation conditions compared to their respective baseline periods (Figures 4.1A-C, top panels). To quantify the increase in global spectral power at 40 Hz, for each stimulation condition and age group, we calculated the median of the difference between stimulation and baseline across subjects along the 95% confidence interval for the median (Figures 4.1A-C, bottom panels). All three stimulation conditions and both age groups showed a confidence interval whose lower bound was above zero at 40 Hz, suggesting that there was a significant enhancement in the 40 Hz power during stimulation compared to baseline. The median of the difference between stimulation and baseline across subjects also showed peaks at subharmonic and first harmonic frequencies of 40 Hz, namely 20 Hz and 80 Hz. The global PSD at these frequencies was significantly higher during visual and bimodal stimulation compared to their respective baseline periods in the young subject group. In the older subject group, the increase was significant only at 20 Hz for visual stimulation.

To determine whether the amount of 40 Hz power enhancement was dependent on stimulation conditions, we compared the increase in global PSD at 40 Hz between visual, auditory, and bimodal stimulation. In the young group, the group median of the global PSD increase at 40 Hz was significantly higher for bimodal stimulation compared to other stimulation conditions (Figure 4.1D, left panel), suggesting that bimodal stimulation induced much stronger gamma frequency entrainment than visual or auditory stimulation alone. Bimodal stimulation

also led to a higher level of entrainment compared to individual unimodal stimulation in the older group, with concurrent visual and auditory stimulation showing a group median of the 40 Hz global PSD change that was significantly larger than auditory stimulation alone and slightly higher than visual stimulation alone (Figure 4.1D, right panel).

We also looked at the increase in 40 Hz power at the individual EEG lead level and found that the distribution of gamma frequency entrainment was dependent on the stimulation condition, with bimodal stimulation inducing the highest number of leads to have a significant increase in 40 Hz spectral power compared to baseline, both for the young and older subject groups (Figure 4.1E). These findings, together with those from the global PSD, suggest that bimodal stimulation can lead to stronger and more widespread gamma frequency entrainment in both young and older subjects than visual or auditory stimulation alone.

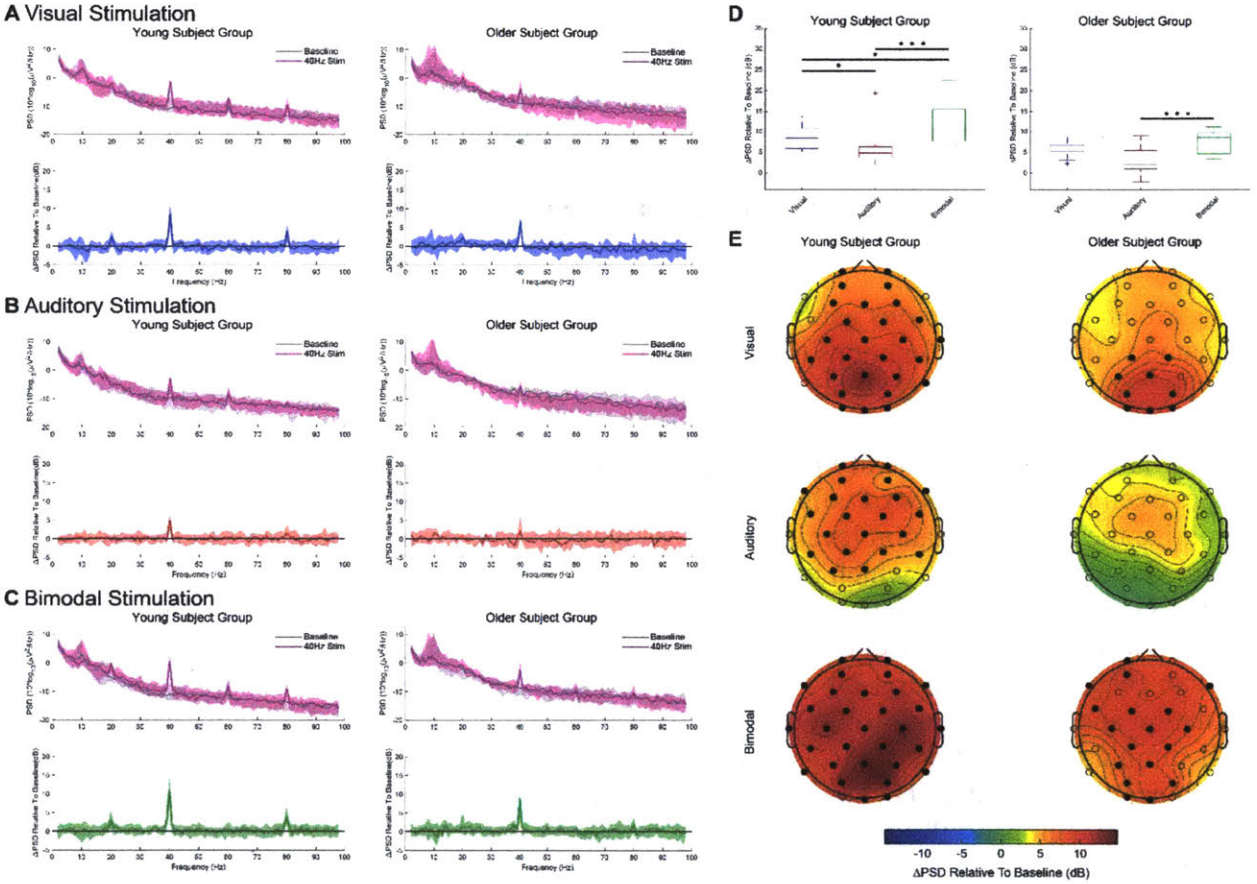

Figure 4.1. Spectral power of brain waves in young and older subjects, in response to different stimulation conditions.

(A-C) Group median (solid line) of global power spectral density (PSD) along with its 95% confidence interval (shaded area) for baseline (gray) and stimulation (magenta) periods, for young (*top left*) and older (*top right*) subject groups. Group median (solid line) of the difference in global PSD between stimulation and baseline periods along with its 95% confidence interval (shaded area) for young (*bottom left*) and older (*bottom right*) subject groups. Confidence intervals for the median of the difference in global PSD were calculated using a Bonferroni-corrected alpha value, controlling for three comparisons per age group (corrected alpha = 0.05/3).

(A) Visual stimulation.
(B) Auditory stimulation
(C) Bimodal stimulation.
(D) Box-and-whisker plots showing group median (horizontal line inside box) and quartiles (top and bottom of box) of global PSD at 40 Hz for visual (blue), auditory (red), and bimodal (green) stimulation, for young (*left*) and older (*right*) subject groups. Stars indicate that the group median of the difference in 40 Hz global PSD increase (relative to baseline) between two stimulation conditions had 95% (*), 99% (**), or 99.9% (***) confidence interval whose lower bound was above zero. Confidence intervals were calculated using a Bonferroni-corrected alpha value, controlling for three comparisons per age group (corrected alpha = 0.05/3 for 95% confidence, 0.01/3 for 99% confidence, 0.001/3 for 99.9% confidence).
(E) Topographical distribution of the group median of the change in 40 Hz PSD (relative to baseline) for visual (*top*), auditory (*middle*), and bimodal (*bottom*) stimulation, for young (*left*) and older (*right*) subject groups. Filled circles indicate EEG leads at which the group median of the difference in 40 Hz PSD between stimulation and baseline periods had 95% confidence interval whose lower bound was above zero. Confidence intervals were calculated using a Bonferroni-corrected alpha value, controlling for thirty-two comparisons per stimulation condition and three comparisons per age group (corrected alpha = $0.05/(32\times3)$).

4.3. 40 Hz sensory stimulation increases gamma frequency synchronization in young and older subjects

Given that synchronous gamma band activity between different cortical areas is closely associated with cognitive functions (Fries, 2009) and reduced in AD (Jelles et al., 2008; Koenig et al., 2005; Stam et al., 2002; Wang et al., 2017), we investigated the effect of 40 Hz sensory stimulation on gamma frequency synchronization. The level of synchronization was quantified using weighted phase lag index (wPLI), a sensitive index of phase synchronization and its changes even in the presence of volume-conduction and noise (Vinck et al., 2011). To summarize the synchronization levels of all possible pair-wise combinations of EEG leads, we calculated the global wPLI, which is the average of wPLI across all EEG lead pairs (see Methods for details), and found that global wPLI at 40 Hz was increased during the stimulation period compared to its preceding baseline period for all three stimulation conditions, in both young and older subject groups (Figures 4.2A-C, top panels). The group median of the difference between stimulation and baseline also had a 95% confidence interval whose lower bound was above zero for all stimulation conditions and age groups, implying a significant enhancement in the overall synchronization level at 40 Hz due to stimulation. In the young subject group, similar to the global PSD, the global wPLI was significantly increased at the first harmonic frequency (i.e., 80 Hz) during visual and bimodal stimulation compared to baseline, but the change at the subharmonic frequency (20 Hz) was not significant for all three conditions. A different pattern was observed in the older group, with only the auditory stimulation showing a significant increase at 20 Hz compared to baseline.

The relationship between the level of enhancement of 40 Hz synchronization and stimulation conditions was investigated by comparing the amplitude of the global wPLI changes between three stimulation conditions. Bimodal stimulation led to a group median of the 40 Hz wPLI increase that was higher than visual or auditory stimulation alone in both age groups, with

the comparison between auditory and bimodal stimulation being significant in the young group (Figure 4.2D). When the change in the wPLI value at 40 Hz was examined at the individual EEG lead pair level, both age groups showed a higher number of connections with a significant increase in 40 Hz wPLI in response to bimodal stimulation than visual or auditory stimulation alone (Figure 4.2E). These findings collectively demonstrate that bimodal stimulation can induce stronger and more extensive gamma frequency synchronization than visual or auditory stimulation alone in both young and older age groups.

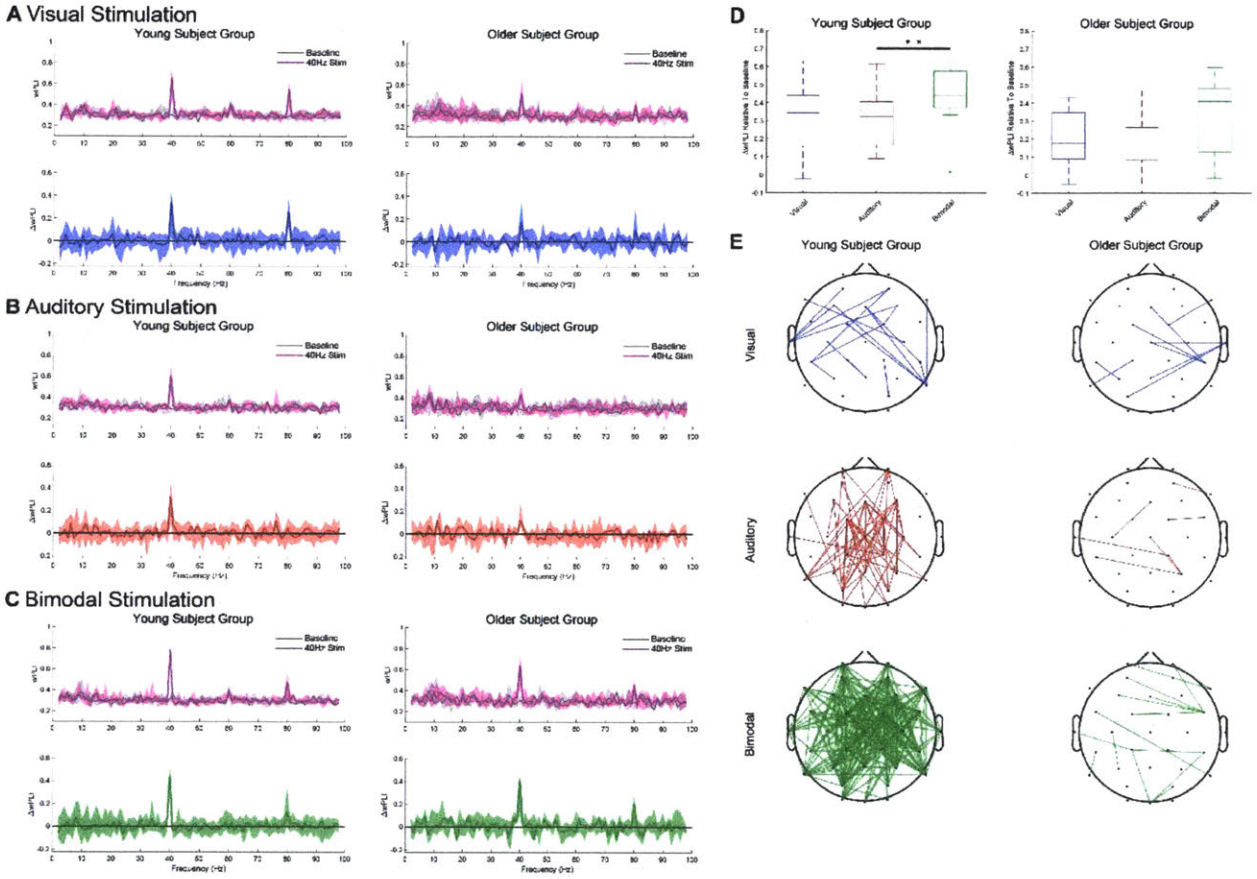

Figure 4.2. Synchronization of brain waves in young and older subjects, in response to different stimulation conditions.

(A-C) Group median (solid line) of global weighted phase lag index (wPLI) along with its 95% confidence interval (shaded area) for baseline (gray) and stimulation (magenta) periods, for young (*top left*) and older (*top right*) subject groups. Group median (solid line) of the difference in global wPLI between stimulation and baseline periods along with its 95% confidence interval (shaded area) for young (*bottom left*) and older (*bottom right*) subject groups. Confidence intervals for the median of the difference in global wPLI were calculated using a Bonferroni-corrected alpha value, controlling for three comparisons per age group (corrected alpha = 0.05/3).

(A) Visual stimulation.

(B) Auditory stimulation

(C) Bimodal stimulation.

(D) Box-and-whisker plots showing group median (horizontal line inside box) and quartiles (top and bottom of box) of global wPLI at 40 Hz for visual (blue), auditory (red), and bimodal (green)

stimulation, for young (*left*) and older (*right*) subject groups. Stars indicate that the group median of the difference in 40 Hz global wPLI increase (relative to baseline) between two stimulation conditions had 95% (*), 99% (**), or 99.9% (***) confidence interval whose lower bound was above zero. Confidence intervals were calculated using a Bonferroni-corrected alpha value, controlling for three comparisons per age group (corrected alpha = 0.05/3 for 95% confidence, 0.01/3 for 99% confidence, 0.001/3 for 99.9% confidence).
(E) Visualization of EEG lead pairs with a significant change in 40 Hz wPLI (relative to baseline) for visual (*top*), auditory (*middle*), and bimodal (*bottom*) stimulation, for young (*left*) and older (*right*) subject groups. Solid lines connect EEG lead pairs that showed the group median of the difference in 40 Hz wPLI between stimulation and baseline periods whose 95% confidence interval had a lower bound above zero. Confidence intervals were calculated using a Bonferroni-corrected alpha value, controlling for 496 lead pair comparisons per stimulation condition and three comparisons per age group (corrected alpha = 0.05/(496×3)).

4.4. Discussion

Here, we investigated the effect of GENUS on neural oscillations of the human brain for the first time, as a first step towards exploring the use of GENUS as a potential therapeutic for AD patients. We demonstrated that 40 Hz sensory stimulation induced gamma entrainment and synchronization in the human brain, without causing any adverse effects. Significant enhancement of 40 Hz oscillations observed over multiple EEG electrodes, which was most pronounced during bimodal stimulation, suggests that GENUS is an effective way of inducing widespread gamma frequency entrainment and synchronization in the human brain. Given the ability of gamma frequency entrainment to reduce AD-related pathology in AD mice (Iaccarino et al., 2016; Martorell et al., 2019), combined with the non-invasive nature of sensory stimulation, GENUS holds a great potential to be an effective and practical treatment strategy for AD patients.

4.5. Methods

4.5.1. Experimental procedures

Each subject was recorded with EEG while being sequentially exposed to six different stimulation conditions. These conditions included 40 Hz visual stimulation with random inter-stimulus interval, 40 Hz visual stimulation with uniform inter-stimulus interval, 40 Hz auditory stimulation with random inter-stimulus interval, 40 Hz auditory stimulation with uniform inter-stimulus interval, 40 Hz bimodal stimulation with random inter-stimulus interval, and 40 Hz bimodal stimulation with uniform inter-stimulus interval. For the stimulation conditions with random inter-stimulus interval, each inter-stimulus interval was randomly chosen from a uniform distribution of values between 20 and 30 ms. Each stimulation condition lasted for 3 minutes and was preceded by a minute of baseline period, during which the light was obscured and the sound volume was set to zero. At the end of the last stimulation condition, the light was obscured and the sound volume was set to zero again for another minute to conclude the experiment. The order in which the six stimulation conditions were delivered was randomized for each subject. The subjects were instructed to remain still and to keep their eyes on the visual stimulation device during the entire experiment.

4.5.2. EEG

EEG was recorded in a dimly lit chamber using a 32-channel EEG system (ActiveTwo, BioSemi) at 512 Hz sampling rate. Pin-type electrodes were inserted to their corresponding plastic electrode holders on an elastic cap. The electrode holders were arranged on the cap according to the international 10-20 layout. Before inserting the electrodes into their corresponding holders, each holder was filled with electrode gel (Signagel, Parker). Horizontal eye movements and eye blinks were monitored by recording the signals from a flat-type electrode attached near the outer canthus of the right eye and below the orbit of the left eye respectively. The signals from active electrodes were referenced to the average of the signals collected from left and right mastoid electrodes, and then bandpass filtered between 0.1 and 100 Hz. Custom-written MATLAB scripts that call on functions from EEGLAB (Delorme and Makeig, 2004) and MATLAB's built-in functions were used to preprocess and analyze the EEG signals.

Appendix A: Imagepatcher user manual

A.1. Hardware Setup

A.1.1. Installing 4-axis micromanipulator

To setup the 4-axis micromanipulator, the SMX-series micromanipulation system (Sensapex) and a single-axis micromanipulator (SMX-SA, Sensapex) are required. One of two 3-axis micromanipulators in the SMX-series should be configured to operate in the inverse virtual axis mode, and the single-axis micromanipulator should be mounted on the x-axis of the 3-axis micromanipulator at an angle suitable for *in vivo* patching. For our experiments, we mounted the single-axis micromanipulator at 30° below the horizontal due to the geometry of our microscope objective (Figure A.1.1).

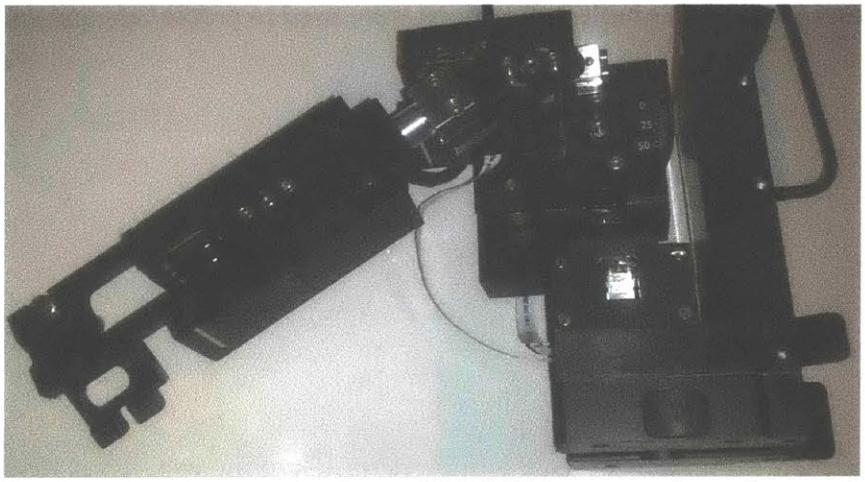

Figure A.1.1: Single-axis micromanipulator (SMX-SA) mounted on the x-axis of the 3-axis micromanipulator (SMX-series) at 30° below the horizontal.

Both the 3-axis and single-axis micromanipulators should then be connected to the control unit of the SMX-series micromanipulation system. The control unit should be connected to the computer via a USB cable. Before operating the micromanipulators, the firmware should be updated. Detailed instructions on how to configure the 3-axis micromanipulator, how to load the single-axis micromanipulator onto the 3-axis micromanipulator, and how to update the firmware can be found from:
www.sensapex.com

The COM port number for the micromanipulator control unit, device id's for the 3-axis micromanipulator as well as the single-axis micromanipulator, and angles of each axis of the 4-axis micromanipulator relative to the horizontal (i.e. x-y plane of the microscope stage) are required for specifying the Imagepatcher user settings (see section A.2.3) and thus should be noted.

A.1.2. Microscope hardware for ScanImage

ScanImage supports several commercial two-photon microscope hardware (e.g., MOM from Sutter; Ultima from PrairieTechnologies) and custom-made microscopes composed of various components from multiple vendors. Detailed information on supported microscope hardware can be found from:
http://vidriotechnologies.com:3000/pages/viewpage.action?pageId=361795

For two-photon microscopes from PrairieTechnologies, several connections have to be made to allow ScanImage to control the microscope hardware. Detailed information on these connections can be found from:
https://openwiki.janelia.org/wiki/display/ephus/(FAQ)+0007

A.1.3. Modifying the autopatcher control box for imagepatching

To correctly generate and control pressure of a patch pipette during imagepatching, the original autopatcher control box (assembled using the instructions provided in the "Autopatcher control assembly manual" in the supplementary material of our 2016 Nature Protocols paper) has to be modified.

*Note: this manual assumes that you have already installed PCIe-6343 (from National Instruments) in a computer that will run the Imagepatcher software and the device's outputs are connected to BNC-2110 (from National Instruments; other NI DAQ devices and connector blocks may be used in place of PCIe-6343 and BNC-2110, as long as they provide 3 analog outputs that can generate voltages ranging from 0 to 5 VDC, with < 400 mA). Please follow the instructions provided by the DAQ device manufacturer to install the device and connect it to its connector blocks. Observe antistatic precautions (use antistatic mat and wrist strap) when touching or wiring to the boards in the autopatcher control box. Do not touch the boards inside the autopatcher control box unnecessarily.

1. **Turn off the autopatcher control box.**

2. **Remove the top panel from the autopatcher control box.**

   Loosen and remove four black screws used to secure the top panel to the chassis.

3. **Remove the connection between the potentiometers and the pressure control board.**

   Remove the wires connected to pins 2, 5, 8, and 11 of the POTS/AO_PH_PL_VL_VH_GND_SIGNAL_5V block on the pressure control board (these are the wires soldered to tab 2 of the potentiometers; pins from which the wires should be removed are highlighted in Figure A.1.2). Use a small flat-head screwdriver to loosen the screw of each terminal BEFORE pulling on the wires to remove them.

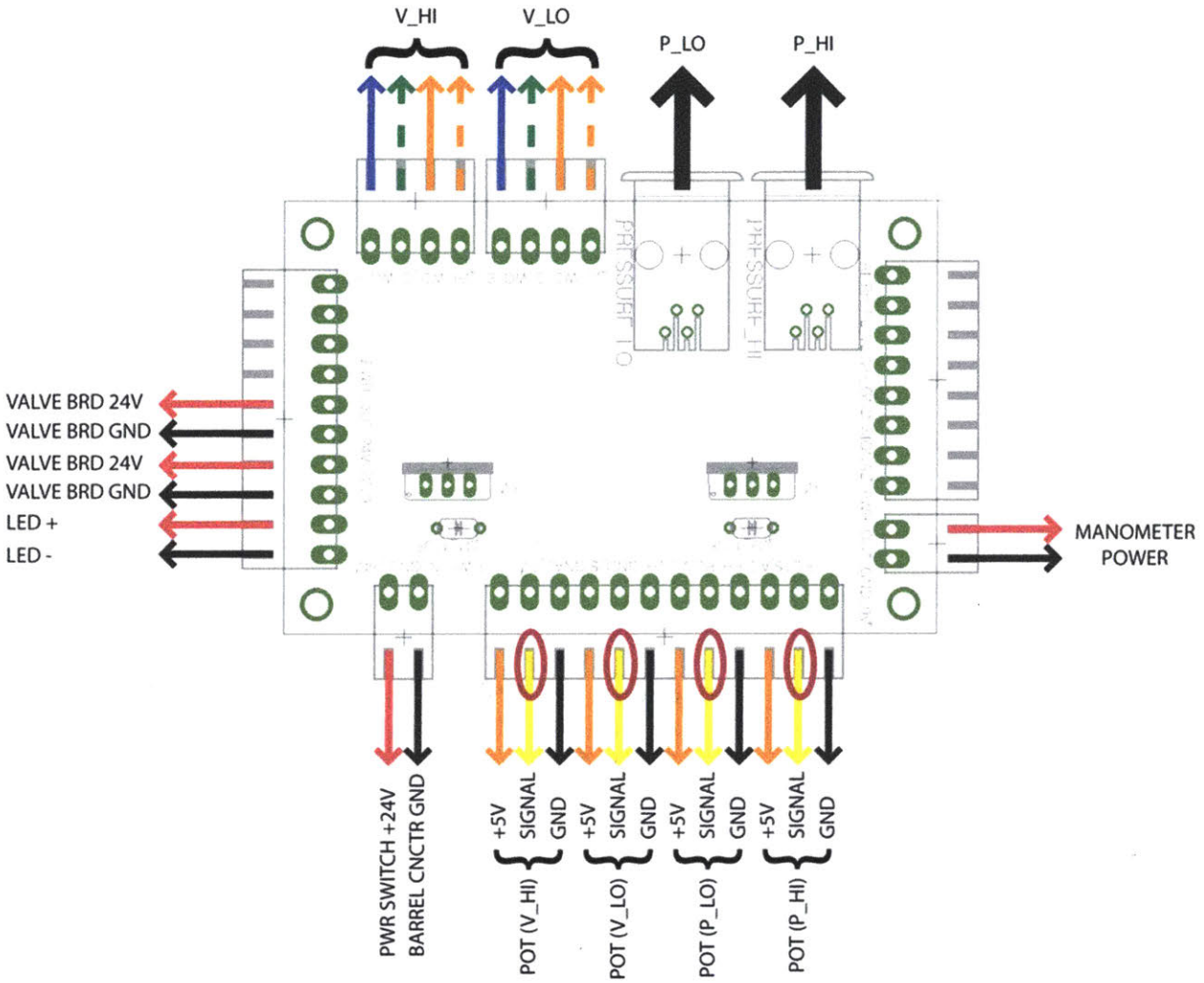

Figure A.1.2: Drawing showing the wiring connections on the pressure control board. Wires to be removed from the board are shown in red circles.

4. **Connect BNC cables to analog output channels #1, 2, and 3 of PCIe-6343.**

   PCIe-6343's pin arrangements are such that the device's analog output #1 (AO1) is on a different connector than analog outputs #2 (AO2) and 3 (AO3). To connect to AO1 of PCIe-6343, connect a BNC cable to AO1 on the BNC-2110 connector block that is connected to "Connector 0" of PCIe-6343. To connect to AO2 of PCIe-6343, connect a BNC cable to AO0 on the BNC-2110 connector block that is connected to "Connector 1" of PCIe-6343. To connect to AO3 of PCIe-6343, connect a BNC cable to AO1 on the BNC-2110 connector block that is connected to "Connector 1" of PCIe-6343. Use BNC cables that are long enough such that their ends can reach the leftmost potentiometer ("high pressure") mounted on the front panel of the autopatcher control box.

5. **Attach BNC adapters to the BNC cables.**

Attach a female BNC adapter to each of the BNC cables connected to the analog outputs of PCIe-6343.

6. **Wire the BNC adapters to the pressure control box.**

Cut three 10" lengths each of yellow and black 24 gauge wire and strip the ends. Wire one end of a yellow wire to each BNC adapter's red terminal. Wire one end of a black wire to each BNC adapter's black terminal. Twist each pair of wires together along most of their length to shield from electrical noise. Connect the pairs of yellow and black wires from the BNC adapters to the POTS/AO_PH_PL_VL_VH_GND_SIGNAL_5V block of the pressure board, in the following way: connect the wires from the BNC adapter connected to AO1 of PCIe-6343 (i.e., the BNC adapter attached to the BNC cable connected to AO1 on the BNC-2110 connector block that is connected to "Connector 0" of PCIe-6343) to the second and the third terminals from the left (pins 2 and 3) in the order yellow-black (i.e., the second terminal from the left (pin 2) gets the yellow wire, and the third terminal from the left (pin 3) gets the black wire). Connect the wires from the BNC adapter connected to AO2 of PCIe-6343 (i.e., the BNC adapter attached to the BNC cable connected to AO0 on the BNC-2110 connector block that is connected to "Connector 1" of PCIe-6343) to the eighth and the ninth terminals from the left (pins 8 and 9) in the same order (yellow-black). Connect the wires from the BNC adapter connected to AO3 of PCIe-6343 (i.e., the BNC adapter attached to the BNC cable connected to AO1 on the BNC-2110 connector block that is connected to "Connector 1" of PCIe-6343) to the eleventh and the twelfth terminals from the left (pins 11 and 12) in the same order (yellow-black). Use a small flat-head screwdriver to loosen the screw of each terminal, then insert the striped end of the wire and tighten the screw to secure the wire.

7. **Set "Name" of PCIe-6343 to "Dev2" and USB-6211 to "Dev3".**

Start "NI MAX," the National Instrument Measurement and Automation Explorer program that is installed with NIDAQmx (the National Instruments device drivers), and expand the "Devices and Interfaces" list in the left hand column. Click "NI PCIe-6343 "Dev#"" from the list, where "Dev#" is a default device name given to PCIe-6343 upon the driver installation (# is most likely any number greater than or equal to 0). If # is not 2 (i.e., if "Dev#" is not "Dev2"), delete "Dev#" in the "Name" field, under "Settings" in the middle column, and type in "Dev2" (without quotation marks). Click "NI USB-6211 "Dev#"" from the list in the left hand column, where "Dev#" is again a default device name given to USB-6211 upon the driver installation (# is most likely any number greater than or equal to 0). If # is not 3 (i.e., if "Dev#" is not "Dev3"), delete "Dev#" in the "Name" field, under "Settings" in the middle column, and type in "Dev3" (without quotation marks). Click "Save" on the top left corner of the middle column to save the device name.

A.1.4. Pressure calibration of the modified autopatcher control box

Pressure generated and output at the "PIPETTE" port by the modified autopatcher control box needs to be calibrated before imagepatching.

1. **Extract Calibration Results.zip.**

2. **Add the "Calibration Results" folder to the MATLAB search path; alternatively, move all the files in the "Calibration Results" folder to a folder previously added to the MATLAB search path**

3. **Set a handheld high-range manometer (e.g., 475-5-FM from Dwyer) to read pressure values in mBar.**

4. **Note the reading on the manometer without anything connected to it.**

   This reading will serve as the baseline value that the manometer reads for the atmospheric pressure.

5. **Input the reading in pressure_calibration_autopatcher box.xlsx file in the "Calibration Results" folder.**

   Input the reading **in column I, row 2.**

6. **Connect the "PIPETTE" output port of the modified autopatcher control box to the input of the manometer.**

   Use appropriate tubing and connectors to fit the input of the manometer. The length/OD/ID of the tubing should be as close, if not same, as those of the tubing that would be used to connect the "PIPETTE" output port of the modified autopatcher control box to the pipette holder.

7. **Type in "pressure_control_HJS_calibration(0:100, 1, 5)" in the MATLAB workspace.**

   The autopatcher control box will start outputting 101 pressure levels in series, for 5 seconds for each pressure level, from low to high positive levels.

8. **Note down the readings from the manometer.**

   All 101 pressure levels should be noted, near the end of the 5-second period for each level. The maximum reading should be at least 100 mBar. If not, plumbing/wiring within the autopatcher control box and the pressurized air supply should be checked.

9. **Input the readings in pressure_calibration_autopatcher box.xlsx file in the "Calibration Results" folder.**

   Input 101 readings, corresponding to the 101 pressure levels output by the autopatcher control box, **in column B, from rows 2 to 102**, in the order they were noted.

10. **Type in "pressure_control_HJS_calibration(0:100, 2, 5)" in the MATLAB workspace.**

    The autopatcher control box will again start outputting 101 pressure levels in series, for 5 seconds for each pressure level, from low to high positive levels.

11. **Note down the readings from the manometer.**

    All 101 pressure levels should be noted, near the end of the 5-second period for each level. These readings should have larger values than those observed in Step 8 above, at least from the 10^{th} reading or so. The maximum reading should be around 1,000 mBar. If the readings are lower or similar to those observed in Step 8, or if the maximum reading is much less than 1,000 mBar, plumbing/wiring within the autopatcher control box and the pressurized air supply should be checked.

12. **Input the readings in pressure_calibration_autopatcher box.xlsx file in the "Calibration Results" folder.**

    Input 101 readings, corresponding to the 101 pressure levels output by the autopatcher control box, **in column C, from rows 2 to 102**, in the order they were noted.

13. **Type in "pressure_control_HJS_calibration(0:100, 3, 5)" in the MATLAB workspace.**

    The autopatcher control box will again start outputting 101 pressure levels in series, for 5 seconds for each pressure level, but this time, the pressure levels would vary from low to high **negative** levels (i.e., from weak to strong suction).

14. **Note down the readings from the manometer.**

    All 101 pressure levels should be noted, near the end of the 5-second period for each level. These readings should be negative, at least from the 5^{th} reading or so, with the last reading around -350 mBar. If the readings are not negative, or if the last reading is not as low as -350 mBar, plumbing/wiring within the autopatcher control box and the pressurized air supply should be checked.

15. **Input the readings in pressure_calibration_autopatcher box.xlsx file in the "Calibration Results" folder.**

    Input 101 readings, corresponding to the 101 pressure levels output by the autopatcher control box, **in column D, from rows 2 to 102**, in the order they were noted.

16. **Type in "pressure_calibration_results_calc_HJS" in the MATLAB workspace.**

    With all the values in the appropriate rows/columns, the function pressure_calibration_results_calc_HJS calculates the best-fit line for each of the three groups of pressure readings and saves the calculation results in a file that will be loaded by the Imagepatcher software.

A.2. Software Setup

The Imagepatcher program is written in MATLAB 2013b (MathWorks) running in a Windows XP or Windows 7 operating system. Current version of the Imagepatcher program requires ScanImage 3.8.1 (free, open-source imaging software from Vidrio Technologies) that can be downloaded from:
http://scanimage.vidriotechnologies.com/display/SIH/ScanImage+Home

Detailed information on how to install and configure ScanImage 3.8.1. can be found from:
http://scanimage.vidriotechnologies.com/display/SIH/ScanImage+r3.8+Documentation

Example initialization file and user file can be found in the "ScanImage Files" folder in Imagepatcher.zip.

*Note: the initialization file ("standard_HJS.ini") in the "ScanImage Files" folder is a modified version of the default initialization file, with the following assumptions: the name of the DAQ device for PMT acquisition, galvo mirror output, and the trigger signal generation/output is "Dev4"; analog output channels 0 and 1 (AO0 and AO1) of the DAQ device for galvo mirror output (i.e., "Dev4") are connected to the X and Y galvo mirror command inputs, respectively; digital output 0 (P0.0) serves as the ScanImage start trigger source; PFI 0 serves as a terminal on which input trigger from P0.0 is received; a DAQ device is installed for pockels cell control, and its name is "Dev2"; analog output channel 0 (AO0) of the DAQ device for the pockels cell control (i.e., "Dev2") is connected to the appropriate analog input on the pockels cell control box. If your setup does not satisfy any of the above assumptions, please make sure you either change your setup such that all of the above assumptions are satisfied or modify appropriate sections in the initialization file to reflect your setup.

A.2.1. Imagepatcher installation

To install the Imagepatcher program on your system, the Imagepatcher files need to be placed in the MATLAB search path, and one of the original ScanImage files needs to be overwritten with

a file with new codes that enable real-time raw image data transfer from ScanImage to the Imagepatcher program. Detailed information on how to view and modify the MATLAB search path can be found from:
http://www.mathworks.com/help/matlab/matlab_env/what-is-the-matlab-search-path.html.

1. **Extract Imagepatcher.zip.**

2. **Add the "Imagepatcher Files" folder to the MATLAB search path; alternatively, move all the files in the "Imagepatcher Files" folder to a folder previously added to the MATLAB search path (e.g., ScanImage folders added to the MATLAB search folder during ScanImage installation).**

3. **Move makeFrameByStripes.m file from the "ScanImage Files" folder to ScanImage 3.8.1\ScanImage\io\ad_da\data_in.**

   The original makeFrameByStripes.m file should be overwritten.

A.2.2. User functions

The Imagepatcher program needs to be bound to three ScanImage events by defining them as user functions in ScanImage. Detailed information on how to interact with the User Functions window in ScanImage 3.8.1. can be found from:
https://openwiki.janelia.org/wiki/pages/viewpage.action?pageId=29524376

1. **Open ScanImage.**

2. **Open User Functions window.**

3. **Toggle to User Functions under User Settings by pressing the "USR" button under "View".**

4. **Add "image_autopatcher_v1.m" as a user function for the events "acquisitionDone" and "sliceDone."**

5. **Enable the user function by clicking the checkbox to the right of each event.**

6. **Expand the User Functions window by pressing the "v" button.**

7. **Under USR-only, add "image_autopatcher_v1.m" as a user function for the event "appOpen."**

8. **Enable the user function by clicking the checkbox to the right of the event.**

   The User Functions window should look like Figure A.2.1.

9. **Save the user function bindings by clicking the "Save" button.**

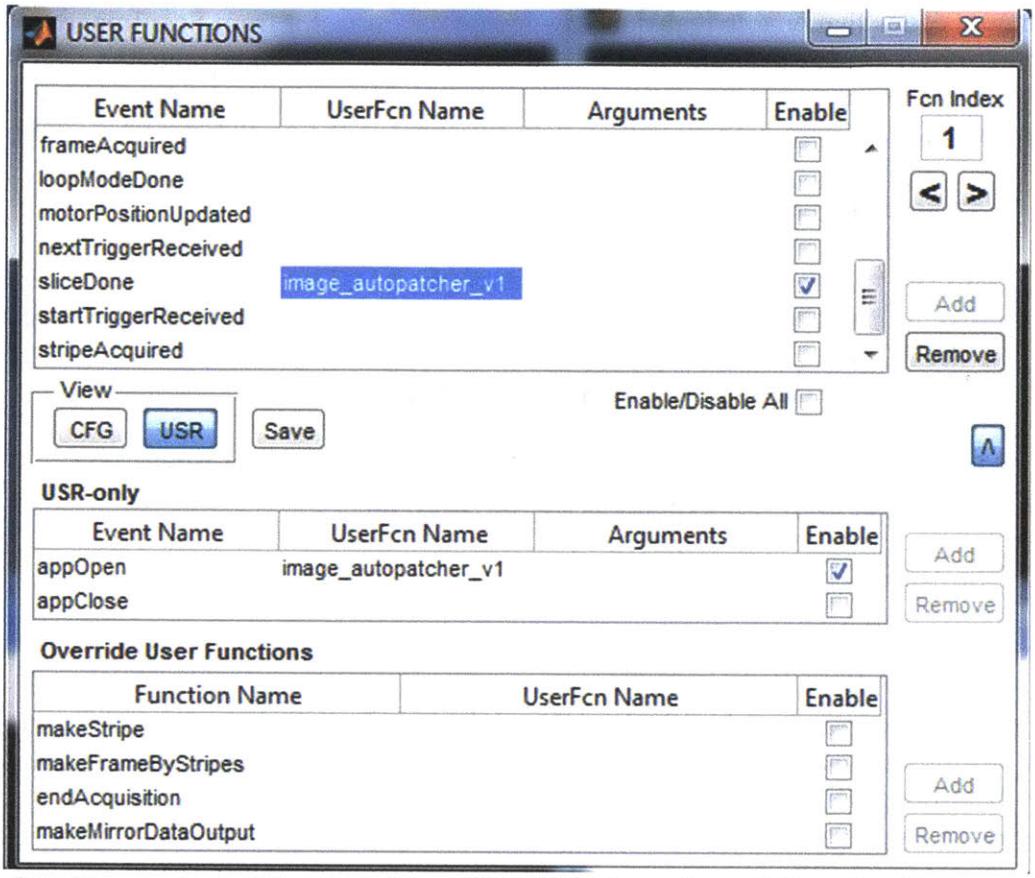

Figure A.2.1: Screenshot of the User Functions Window after adding the Imagepatcher file to two ScanImage events.

A.2.3. Imagepatcher user settings

Information about the microscope objective, the 4-axis micromanipulator, and the patch amplifier has to be specified as user settings in the Imagepatcher software.

*Note: the current version of the Imagepatcher utilizes the remote control functionality of Multiclamp Commander (from Molecular Devices) to enable automated pipette offset zeroing and pipette capacitance neutralization during the Imagepatcher operation (the code for Multiclamp Commander control was obtained from https://clm.utexas.edu/robotpatch/, the website for the MATLAB-based automated blind patching system in awake mice (Desai et al., 2015); big thanks to Dr. Niraj Desai). The Imagepatcher is designed to work with a number of patch clamp amplifiers other than Multiclamp amplifiers, but the current version of the Imagepatcher software is designed for the Multiclamp amplifiers that are controlled by Multiclamp Commander. This manual assume that a Multiclamp amplifier is used and Multiclamp Commander can control it. Another version of the Imagepatcher software that is not paired to Multiclamp Commander will soon be uploaded to our website.

1. **Open ScanImage.**

2. **Click "Default" when the dialog box asking for the Imagepatcher user settings appears.**

   Since no user settings have been saved yet, choose "Default" to proceed (Figure A.2.2). The Imagepatcher GUI should then appear (Figure A.2.3). If it does not, check if the Imagepatcher software has been correctly set as a user function (refer to section A.2.2).

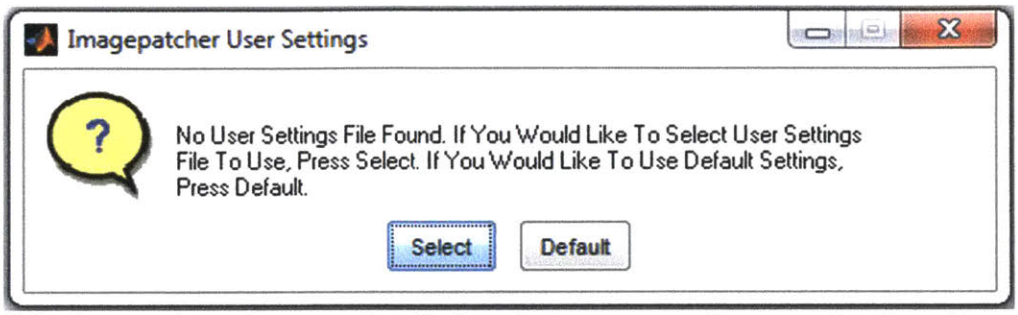

Figure A.2.2: Screenshot of a question dialog that appears after opening ScanImage.

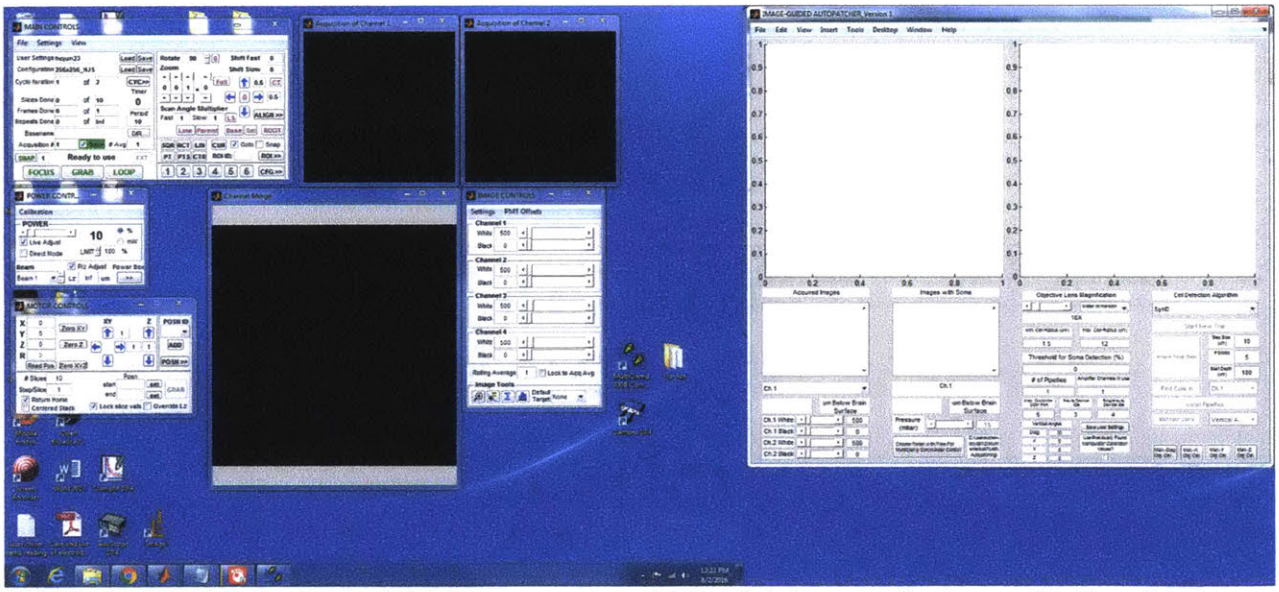

Figure A.2.3: Screenshot of the Imagepatcher GUI (right) opened along with ScanImage 3.8.1 (left).

3. **Specify magnification and type of the microscope objective.**

   Specify magnification and water immersion vs non-water immersion of the microscope objective using the slider and the dropdown menu respectively, under "Objective Lens Magnification" on the Imagepatcher GUI (Figure A.2.4).

4. **Specify the number of pipettes to be used simultaneously to patch a targeted cell.**

   Type in the number of pipettes in the "# of Pipettes" textbox on the Imagepatcher GUI (Figure A.2.4); for single cell patching, type in 1 in the textbox.

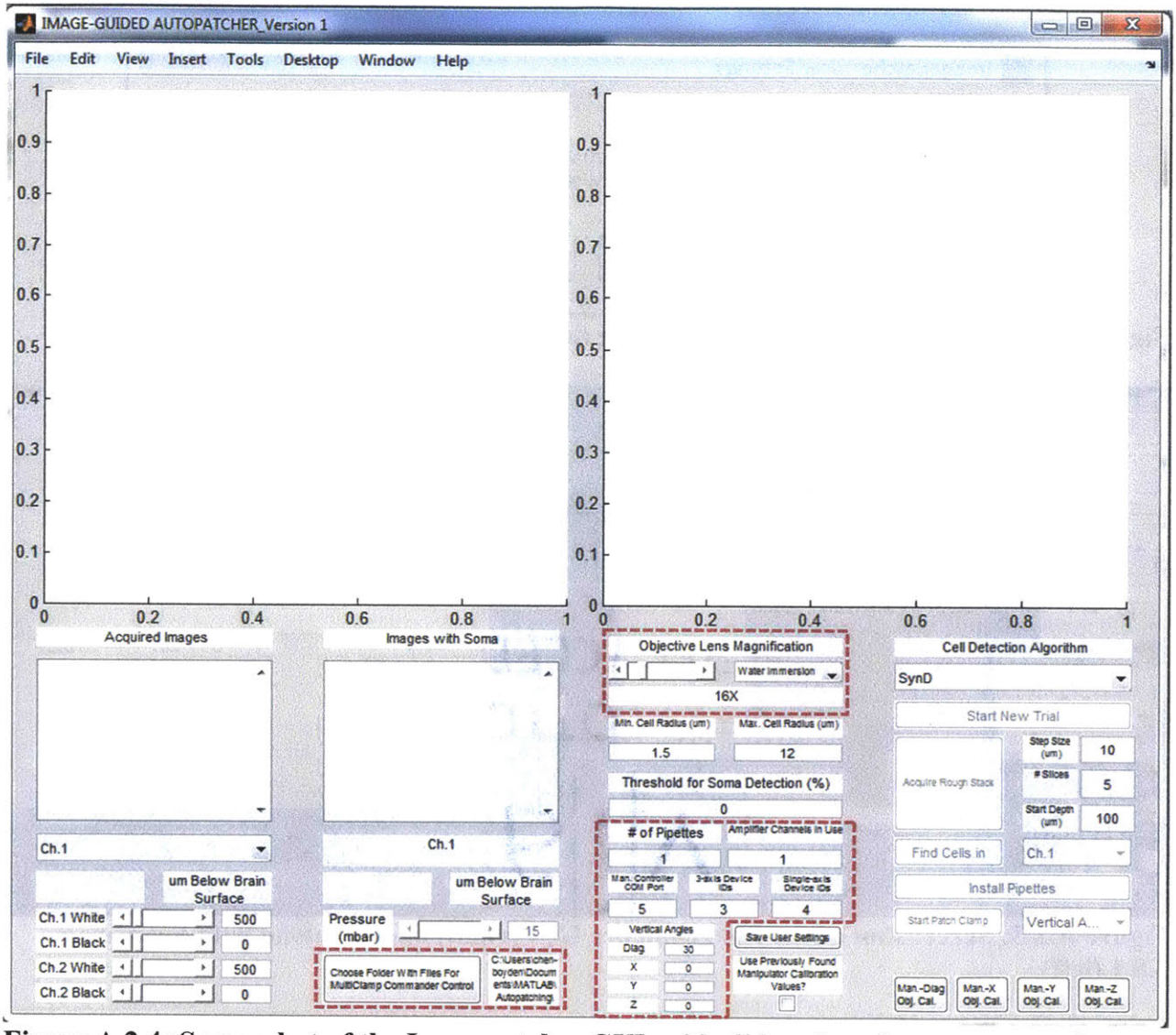

Figure A.2.4: Screenshot of the Imagepatcher GUI, with slider, dropdown menu, and textboxes for user settings outlined with red dash lines.

5. **Specify the information about the micromanipulator.**

   Specify the COM port number for the micromanipulator control unit, device id's for the 3-axis micromanipulator as well as the single-axis micromanipulator, and angles of each axis of the 4-axis micromanipulator relative to the horizontal (based on the

information noted during the micromanipulator installation in section A.1.1) using corresponding textboxes on the Imagepatcher GUI (Figure A.2.4).

6. **Specify the information about the Multiclamp amplifier and Multiclamp Commander.**

   Type in the amplifier channel number in the "Amplifier Channel In Use" textbox on the Imagepatcher GUI (Figure A.2.4); for single cell patching, type in a single number in the textbox. Specify the location of the folder that contains the files for remote control of Multiclamp Commander by clicking the "Choose Folder With Files For MultiClamp Commander Control" pushbutton on the Imagepatcher GUI (Figure A.2.4) and choosing the "multiclamp_control" folder (one of the folders that were in Imagepatcher.zip and extracted along the "Imagepatcher Files" folder and the "ScanImage Files" folder) using the dialog box that pops up.

7. **Save the user settings by clicking the "Save User Settings" pushbutton on the Imagepatcher GUI.**

   The user settings are now saved and will be loaded automatically when ScanImage is opened.

A.3. FOV Size Calibration

The current version of the Imagepatcher uses the FOV size that was calibrated using a 16x water immersion objective lense (CFI75 LWD 16x W NA 0.8 WD 3.0mm objective, Nikon) on our two-photon microscope (Ultima moving IV, Prairie Technologies). Unless the same objective and microscope are used, the FOV sizes should be calibrated (it is strongly recommended to calibrate the FOV sizes even if the same objective and microscope as ours are used).

1. **Place a calibration slide (e.g., 2285-27 from Ted Pella) on the microscope stage.**

2. **Image the calibration slide using ScanImage at zoom of 1.**

   Focus on the calibration slide such that the divisions on the scale of the calibration slide are clearly visible, even at the edges of the FOV.

3. **Calculate the FOV size.**

   Determine the size of FOV by counting the scale divisions inside the FOV.

4. **Add the calculated FOV size to the Imagepatcher software.**

   The current version of the Imagepatcher software requires manual edits in four .m files (the next version will incorporate a method for easier/simpler addition of the

pixel sizes to the Imagepatcher software). Change the files at appropriate lines as indicated by **Table 3.1**.

File name	Lines	Things to change
Find_cells_gui_SI.m	2126-2127, 2129-2130, 2635-2636, 2638-2639, 3148-3149, 3151-3152, 3656-3657, 3659-3660, 4173-4174, 4176-4177, 4681-4682, 4684-4685, 5206-5207, 5209-5210, 5713-5714, 5716-5717, 6696-6697, 6699-6700, 6849-6850, 6852-6853, 7454-7455, 7456-7457, 8326-8327, 8329-8330, 8363-8364, 8366-8367,	If water immersion objective was used: - replace every "5.2384*256" with the calculated FOV size. - replace every "16" with the zoom factor of the objective. If non-water immersion objective was used: - replace every "7.6006*256" with the calculated FOV size. - replace every "10" with the zoom factor of the objective.
Find_soma_HJS.m	82-83, 85-86	
Image_autopatcher_v1.m	403-404, 406-407, 411-412, 414-415, 1056-1057, 1059-1060, 2100-2101, 2103-2104, 2982-2983, 2985-2986, 3129-3130, 3132-3133	
Plot_scalebar_HJS.m	6, 8	

Table 3.1: Files and their lines to be changed to incorporate the calibrated FOV sizes.

A.4. Micromanipulator-Microscope Motorized Platform Calibration

Before performing imagepatching experiments, step sizes of motion and axis angles of the 4-axis micromanipulator need to be calibrated to those of the motorized platform of the two-photon microscope. This calibration can be performed using four pushbuttons on the Imagepatcher GUI.

1. **Prepare a well that is at least 1 mm deep and 2 mm in diameter (e.g., disposable medicine cups from Cypress Medical Products; item # 95-00).**

2. **Fill the well to the top with a clear solution (e.g., deionized water).**

3. **Place the well on the microscope stage.**

4. **Immerse the lens of a water immersion microscope objective into the well.**

   Microscope objective that will be used during patching experiments should be used here.

5. **Click one of four pushbuttons located near the bottom right corner of the Imagepatcher GUI.**

These pushbuttons (Figure A.4.1) each represents calibration of each of the four micromanipulator axes.

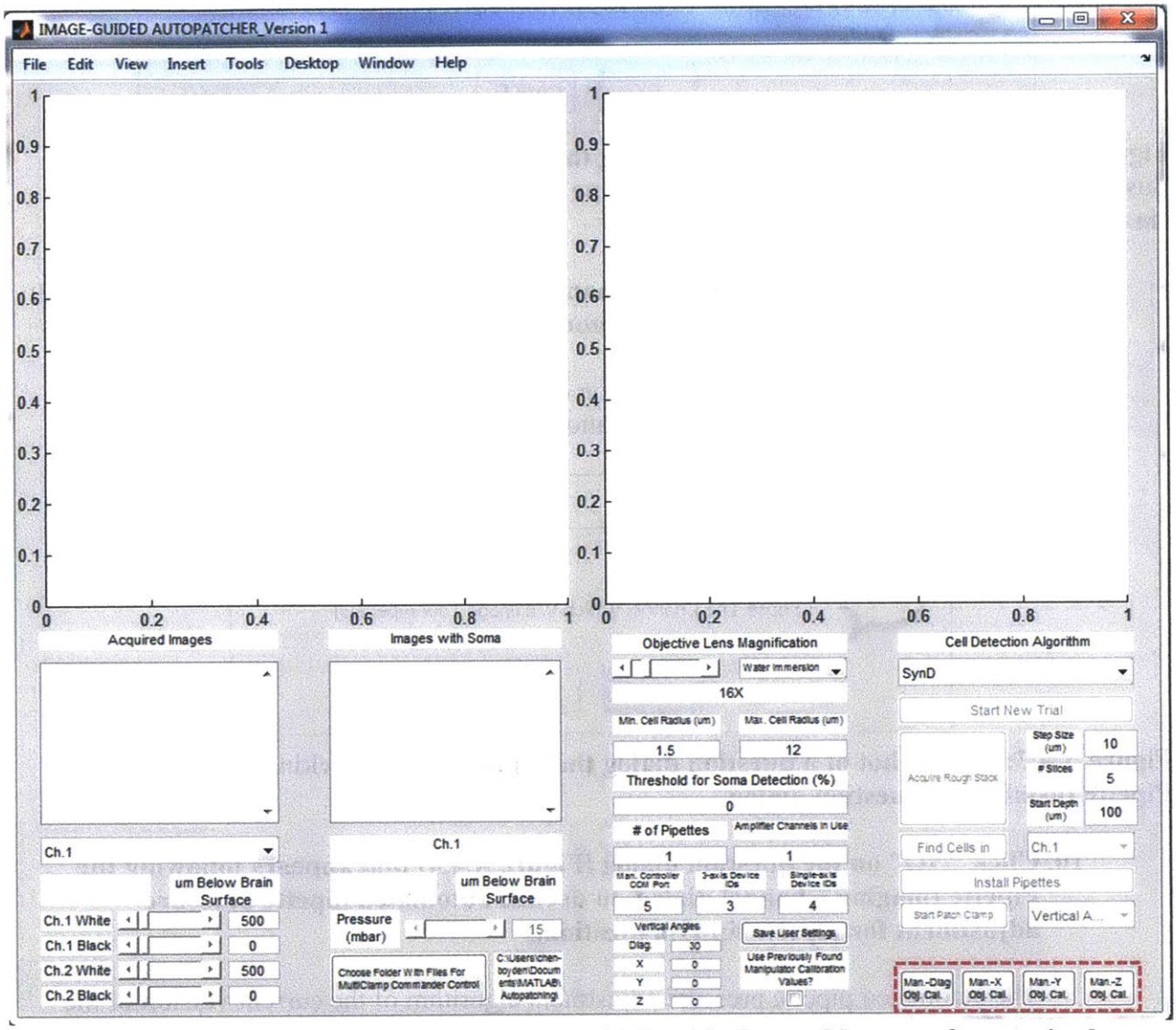

Figure A.4.1: Screenshot of the Imagepatcher GUI, with the pushbuttons for manipulator-microscope platform calibration outlined with red dash lines.

6. **Fill a patch pipette with a solution mixed with a fluorescent dye (e.g., 50 µM Alexa 488 dye in deionized water).**

7. **Install the pipette in a pipette holder.**

8. **Click "OK" on the question dialog (Figure A.4.2) that appears following the pushbutton click, to confirm proper pipette installation.**

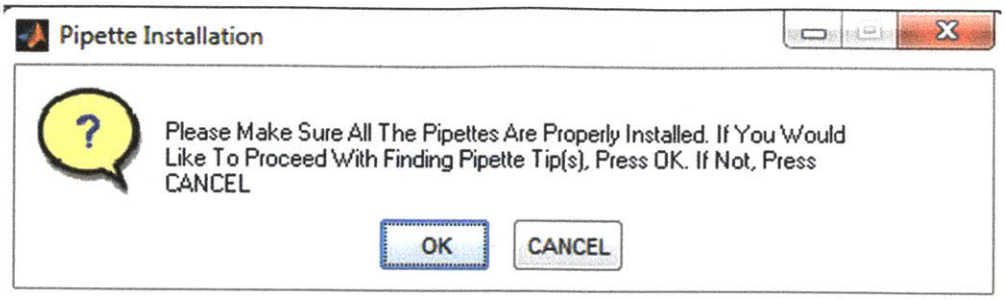

Figure A.4.2: Screenshot of a question dialog that appears after clicking one of the four pushbuttons for micromanipulator-microscope motorized platform calibration on the Imagepatcher GUI.

9. **Specify the microscope imaging channel (i.e., the photomultiplier tube channel) that the dye inside the pipette is fluorescent in.**

   Choose the channel using the question dialog (Figure A.4.3) that appears after clicking "OK" on the Pipette Installation question dialog.

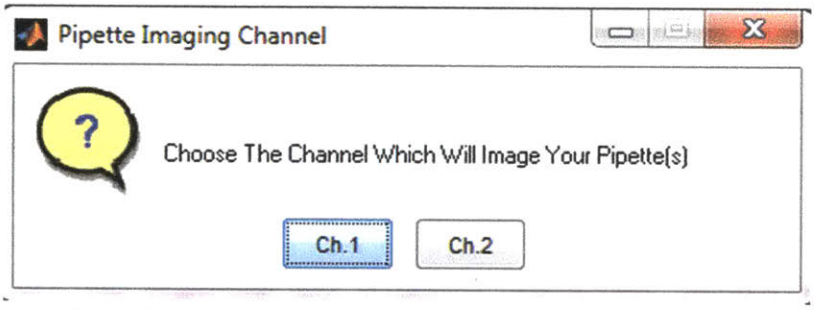

Figure A.4.3: Screenshot of a question dialog that appears after clicking "OK" on the Pipette Installation question dialog.

10. **Click "NO" on the question dialog (Figure A.4.4) that appears following the Pipette Imaging Channel dialog, to decline automated pipette pressure adjustment for pipette tip visualization.**

    The automated pipette pressure adjustment algorithm of the current version of the Imagepatcher software is not yet robust. More robust algorithm will be developed and updated on our website.

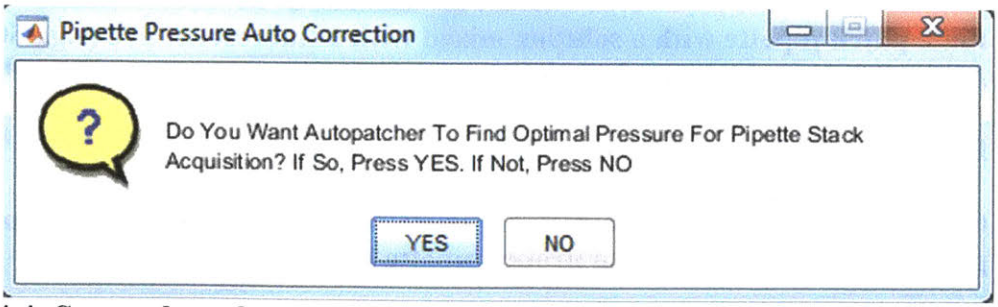

Figure A.4.4: Screenshot of a question dialog that appears after choosing the imaging channel on the Pipette Imaging Channel question dialog.

11. Using the rotary knobs on the micromanipulator control unit, move the tip of the pipette to the center of field of view.

12. Visualize the pipette tip using ScanImage.

Use a high enough zoom (one that results in a field of view of around 80 x 80 μm^2) to see the fine details of the pipette tip. Adjust the pipette tip position as necessary.

13. Adjust the pipette pressure for clear visualization of the pipette tip.

Use the pressure slider on the Imagepatcher GUI (Figure A.4.5) to adjust the pipette pressure such that the pipette tip is clearly visible (e.g., Figure A.4.6). Choose pressure that is high enough to eject little dye at the tip but not too high to cause a large bolus.

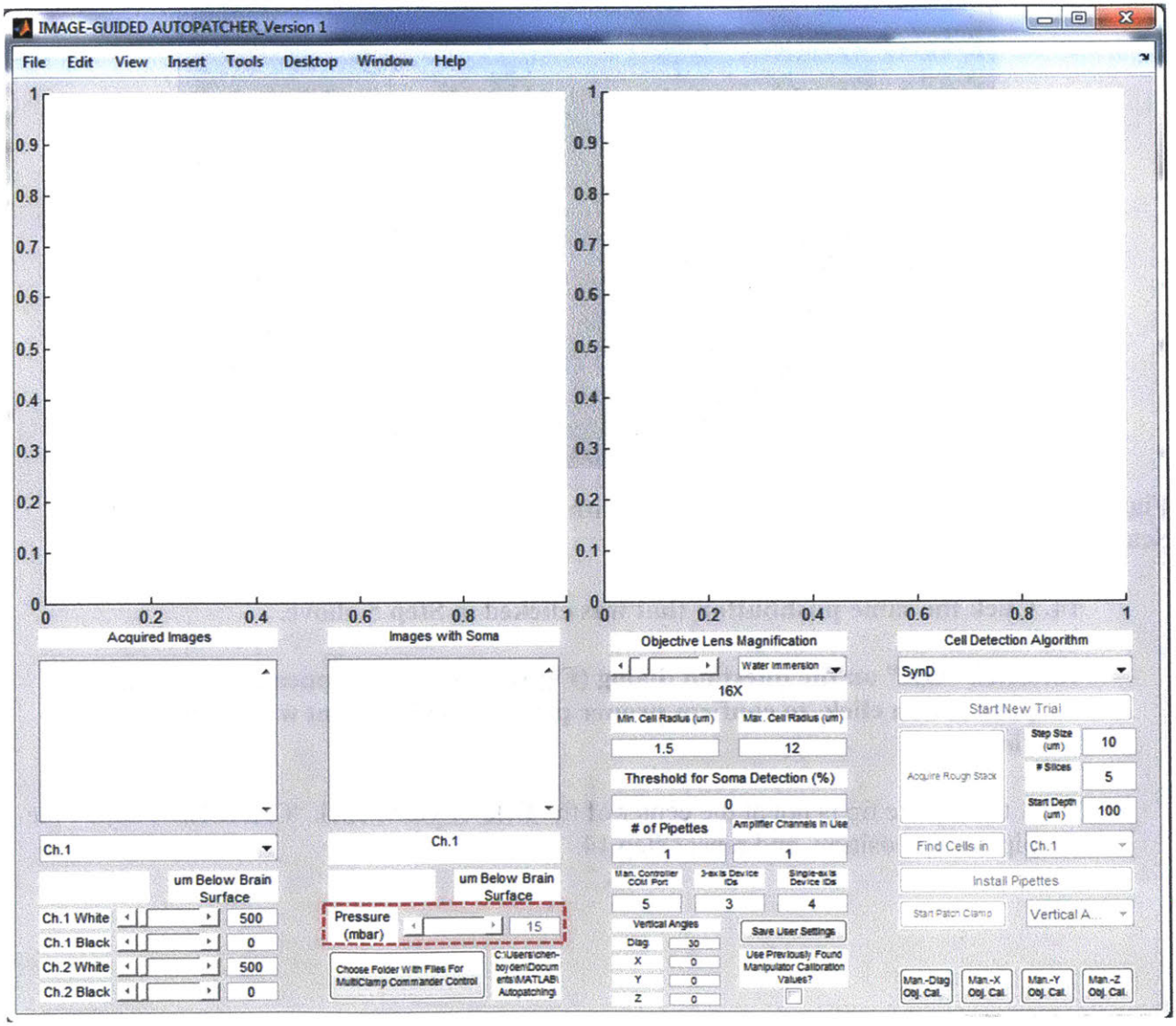

Figure A.4.5: Screenshot of the Imagepatcher GUI, with the pipette pressure slider outlined with red dash lines.

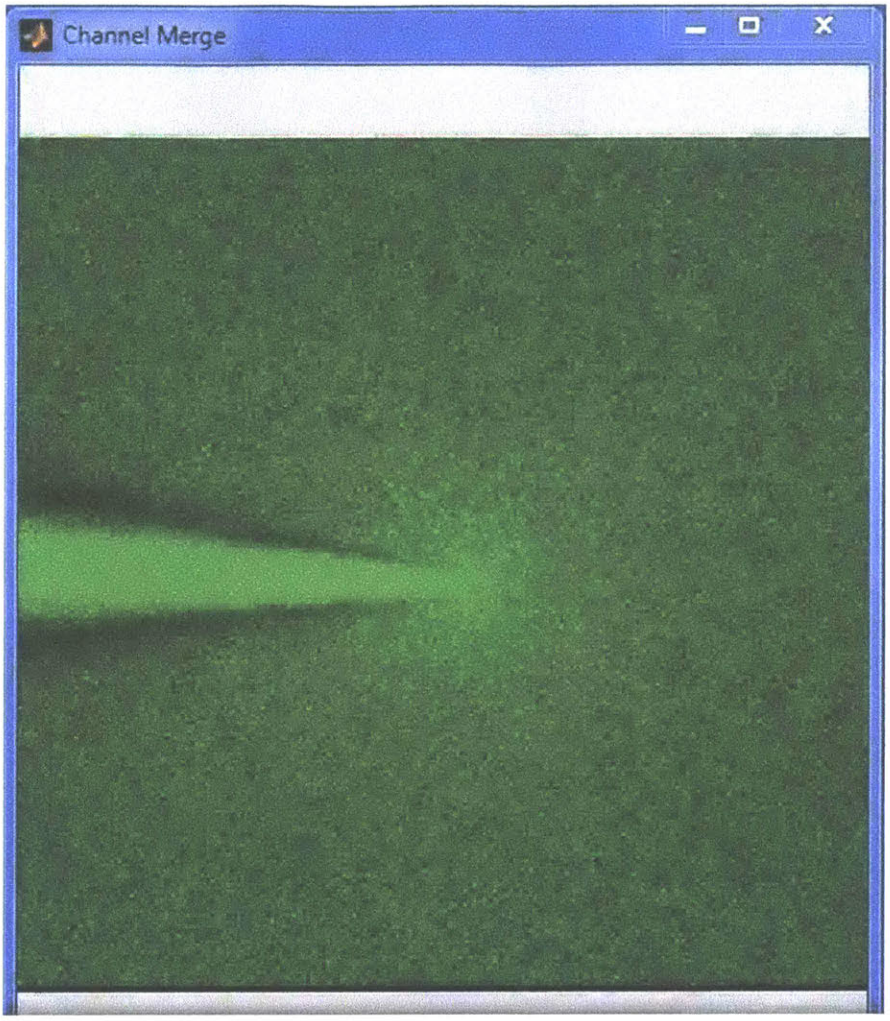

Figure A.4.6: Screenshot of a pipette filled with Alexa 488 dye solution, visualized using ScanImage via the merge channel.

14. **Click the same pushbutton that was clicked in Step 5 above.**

15. **Click "OK" on the question dialog (Figure A.4.7) that appears following the pushbutton click, to confirm proper pipette tip placement within the field of view.**

    If the pipette tip is not at the center of the field of view, click "CANCEL", adjust the pipette tip position, and repeat step 14.

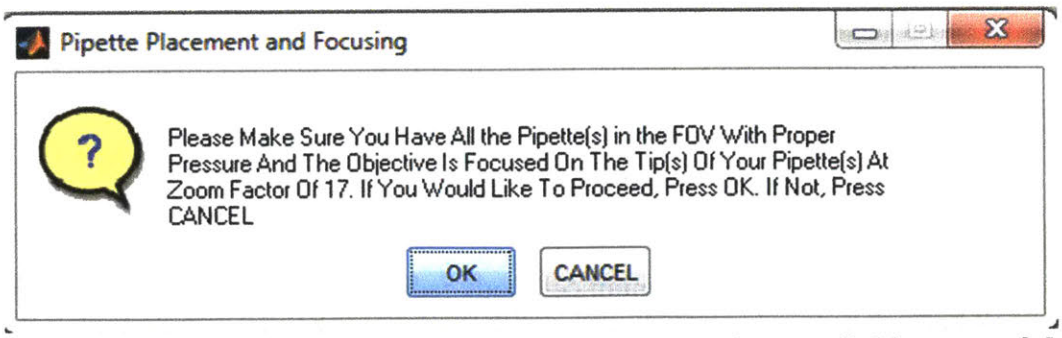

Figure A.4.7: Screenshot of a question dialog that appears after re-clicking one of the four pushbuttons for micromanipulator-microscope motorized platform calibration on the Imagepatcher GUI.

16. **Repeat steps 5 – 15 for the calibration of each of the remaining micromanipulator axes.**

    The same pipette may be used for calibrating multiple axes.

After performing the calibration of all 4 axes of the micromanipulator, the Imagepatcher software automatically saves the calibration results to a .mat file. The saved calibration results can be used for future experiments by simply clicking the checkbox under "Use Previously Found Manipulator Calibration Values?" on the Imagepatcher GUI.

A.5. Running Imagepatching Experiment

With the user settings and the calibration results saved, the Imagepatcher software is ready for an imagepatching experiment.

1. **Find the brain surface inside the craniotomy.**

   Image the brain inside the craniotomy (using ScanImage) and look for hallmark features of the brain surface (e.g., prominent blood vessels on the brain surface; very dim and scattered fluorescence).

2. **Specify the characteristics of a z-stack of the brain to be acquired.**

   Type in the number of images, the step size between two consecutive images, and the starting depth of the z-stack inside the brain using the corresponding textboxes on the Imagepatcher GUI (Figure A.5.1).

3. **Click the "Acquire Rough Stack" pushbutton on the Imagepatcher GUI to start acquisition of the z-stack.**

   The Imagepatcher will automatically initiate the acquisition of the z-stack, starting from the depth that was specified in step 2.

4. **Select images on which to run the cell detection.**

To select the images, click image names from the list of acquired images shown under "Acquired Images" on the Imagepatcher GUI. Selected image names will be highlighted in blue, and the first of the selected images will be displayed in the left display window of the Imagepatcher GUI (e.g., Figure A.5.2).

5. **Specify the cell detection criteria**.

Type in minimum and maximum cell body radii (in microns) as well as threshold for cell body detection (as a percentage of the maximum pixel intensity within the selected images) using the corresponding textboxes on the Imagepatcher GUI (Figure A.5.2).

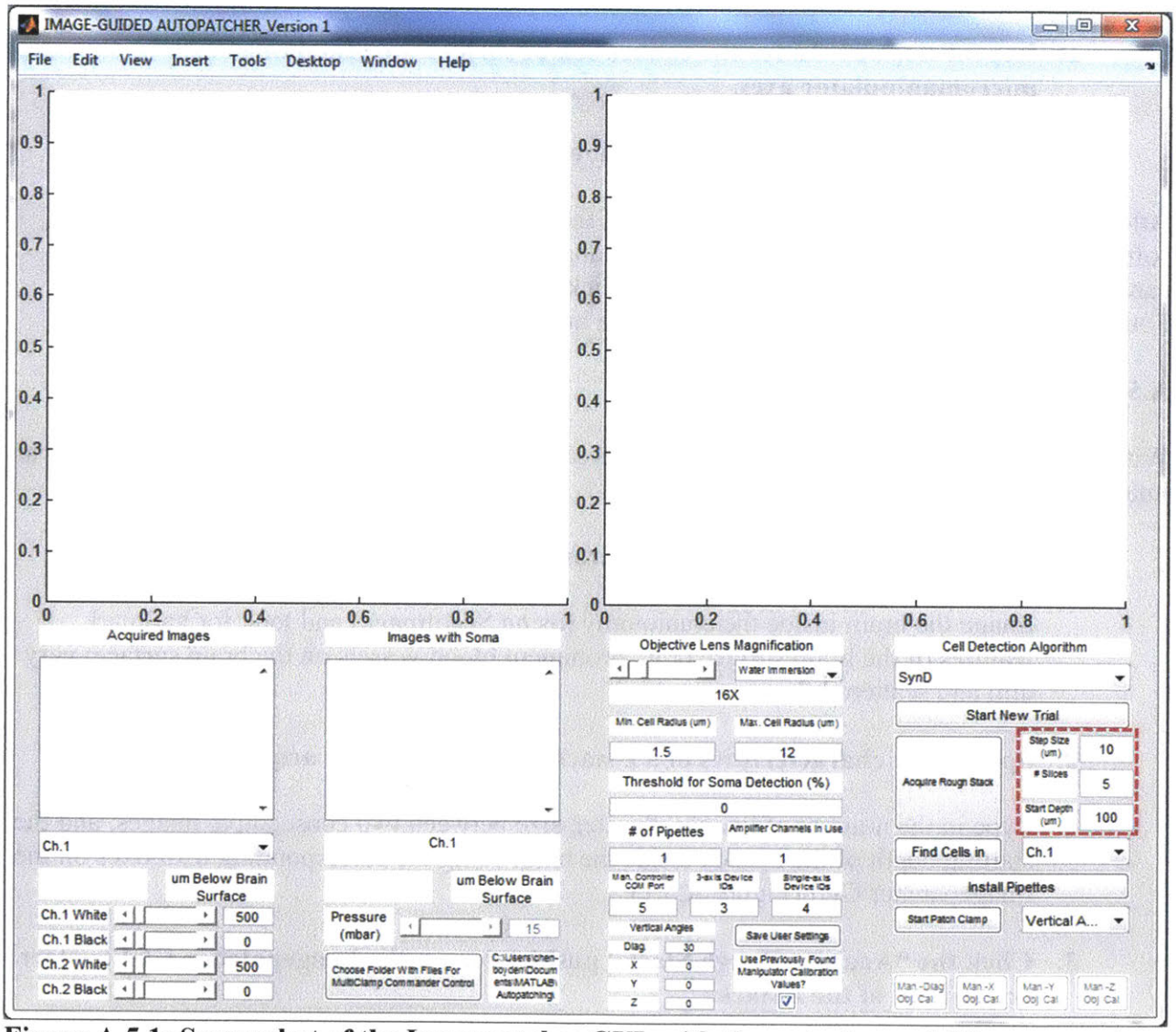

Figure A.5.1: Screenshot of the Imagepatcher GUI, with the z-stack acquisition parameter textboxes outlined with red dash lines

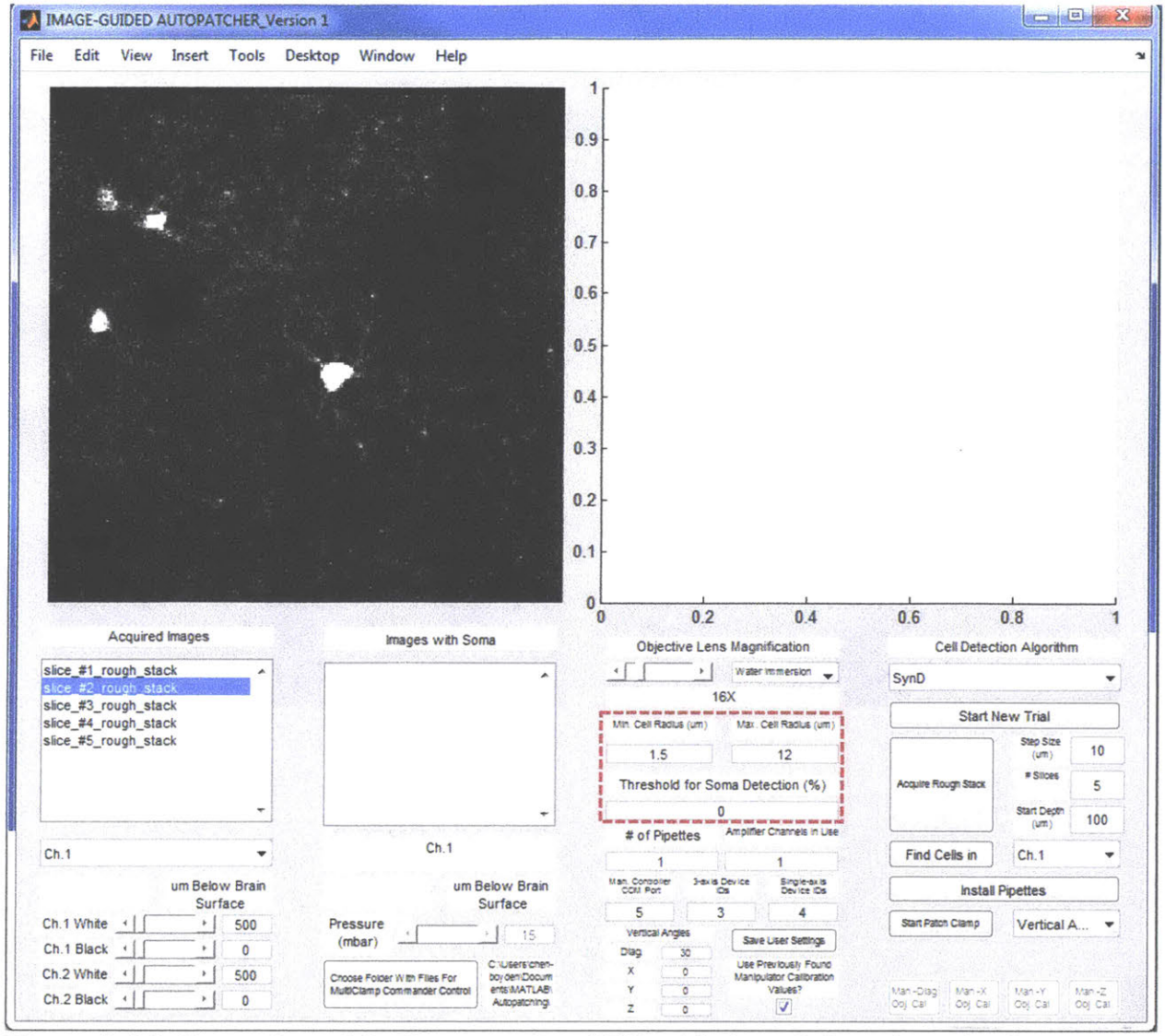

Figure A.5.2: Screenshot of the Imagepatcher GUI, with the cell detection criteria textboxes outlined with red dash lines.

6. **Specify the microscope imaging channel (i.e., the photomultiplier tube channel) that the cells are fluorescent in**.

   Use the dropdown menu next to the "Find Cells in" pushbutton (Figure A.5.3) on the Imagepatcher GUI to select the channel.

7. **Click the "Find Cells in" pushbutton on the Imagepatcher GUI to detect and visualize cells from each of the selected images.**

   Cells that meet the detection criteria specified in step 5 will be outlined with red lines and displayed in the right display window of the Imagepatcher GUI (e.g., Figure A.5.3).

8. **Select a cell to patch by clicking inside one of the detected cells.**

   The red outline of the selected cell will change to yellow (Figure A.5.3).

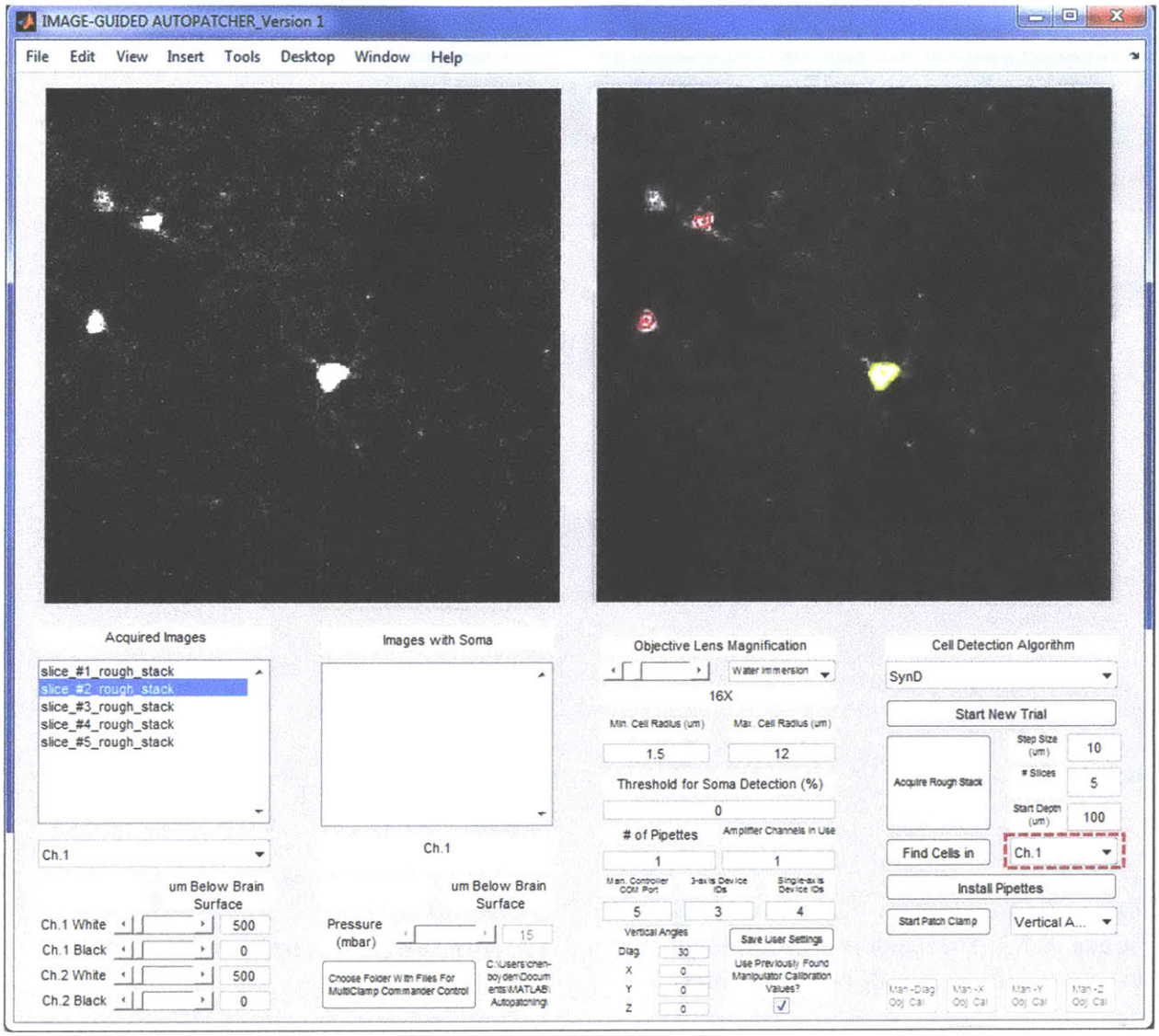

Figure A.5.3: Screenshot of the Imagepatcher GUI, with the cell imaging channel dropdown menu outlined with red dash lines.

9. **Open Multiclamp 700B Commander.**

10. **Select the "VC" button under "Mode" on the Multiclamp 700B Commander GUI.**

    Select the VC mode for the amplifier channel that was specified in the user settings (Figure A.2.4; step 6 in section A.2.3).

11. **Click the "Install Pipettes" pushbutton on the Imagepatcher GUI to start the pipette installation.**

12. **Fill a patch pipette with an internal solution mixed with a fluorescent dye (e.g., 50 µM Alexa 488 dye).**

13. **Install the pipette in a pipette holder.**

14. **Click "OK" on the question dialog (Figure A.5.4) that appears following the "Install Pipettes" pushbutton click, to confirm proper pipette installation.**

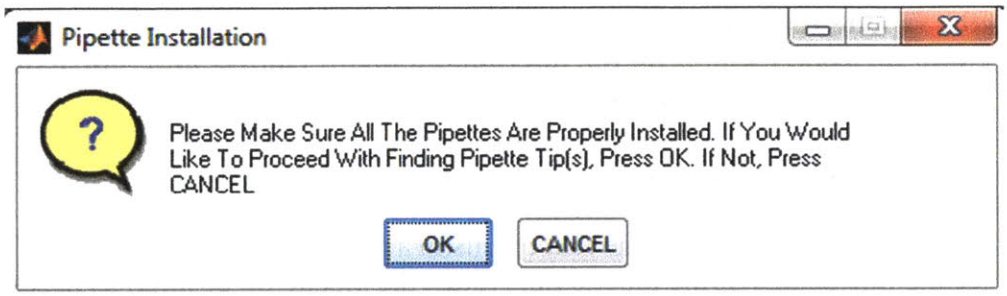

Figure A.5.4: Screenshot of a question dialog that appears after clicking the "Install Pipettes" pushbutton on the Imagepatcher GUI.

15. **Specify the microscope imaging channel (i.e., the photomultiplier tube channel) that the dye inside the pipette is fluorescent in.**

    Choose the channel using the question dialog (Figure A.5.5) that appears after clicking "OK" on the Pipette Installation question dialog.

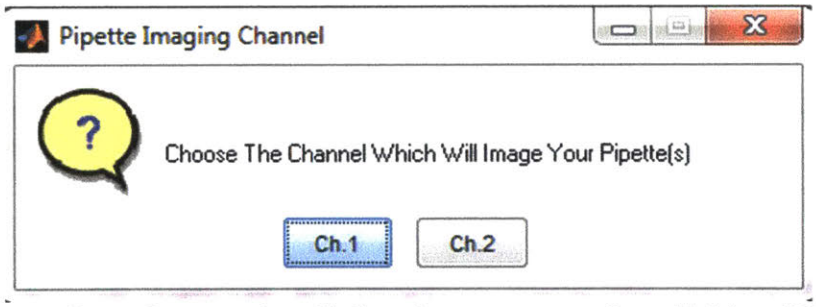

Figure A.5.5: Screenshot of a question dialog that appears after clicking "OK" on the Pipette Installation question dialog.

16. **Click "NO" on the question dialog (Figure A.5.6) that appears following the Pipette Imaging Channel dialog, to decline automated pipette pressure adjustment for pipette tip visualization.**

    The automated pipette pressure adjustment algorithm of the current version of the Imagepatcher software is not yet robust. More robust algorithm will be developed and updated on our website. After the click, the Imagepatcher software communicates with Multiclamp Commander to zero the pipette offset and neutralize pipette

capacitance. The "Install Pipettes" pushbutton on the Imagepatcher GUI also changes to the "Acquire Pipette Image Stack" pushbutton.

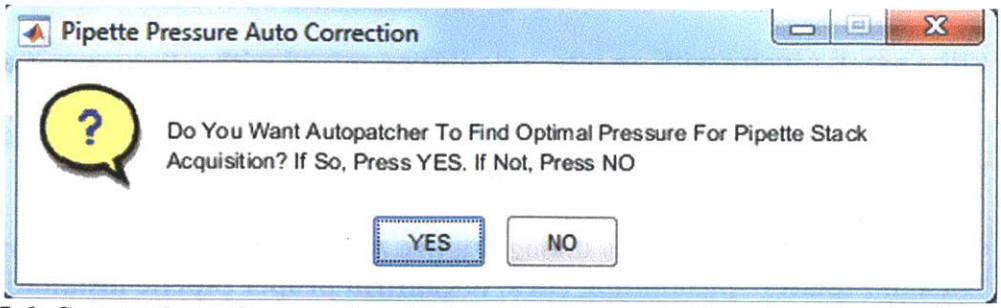

Figure A.5.6: Screenshot of a question dialog that appears after choosing the imaging channel on the Pipette Imaging Channel question dialog.

17. **Using the rotary knobs on the micromanipulator control unit, move the tip of the pipette to the center of field of view.**

18. **Visualize the pipette tip using ScanImage.**

    Use a high enough zoom (one that results in a field of view of around 80 x 80 μm^2) to see the fine details of the pipette tip. Adjust the pipette tip position as necessary.

19. **Adjust the pipette pressure for clear visualization of the pipette tip.**

    Use the pressure slider on the Imagepatcher GUI to adjust the pipette pressure such that the pipette tip is clearly visible (e.g., Figure A.5.7). Choose pressure that is high enough to eject little dye at the tip but not too high to cause a large bolus.

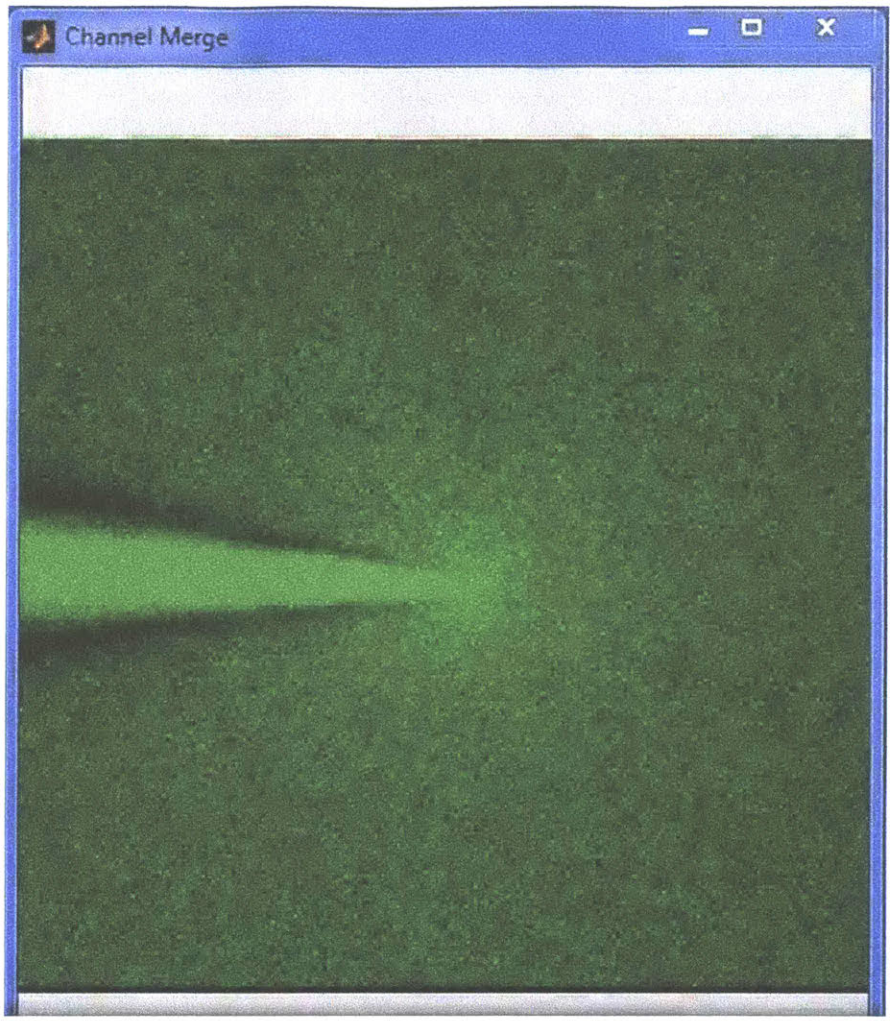

Figure A.5.7: Screenshot of a pipette filled with Alexa 488 dye solution, visualized using ScanImage via the merge channel.

20. Click the "Acquire Pipette Image Stack" pushbutton on the Imagepatcher GUI.

21. Click "OK" on the question dialog (Figure A.5.8) that appears following the pushbutton click, to confirm proper pipette tip placement within the field of view.

If the pipette tip is not at the center of the field of view, click "CANCEL", adjust the pipette tip position, and repeat step 20. When "OK" is clicked, the resistance of the pipette is measured, and the measurement statistics are displayed on another question dialog (Figure A.5.9).

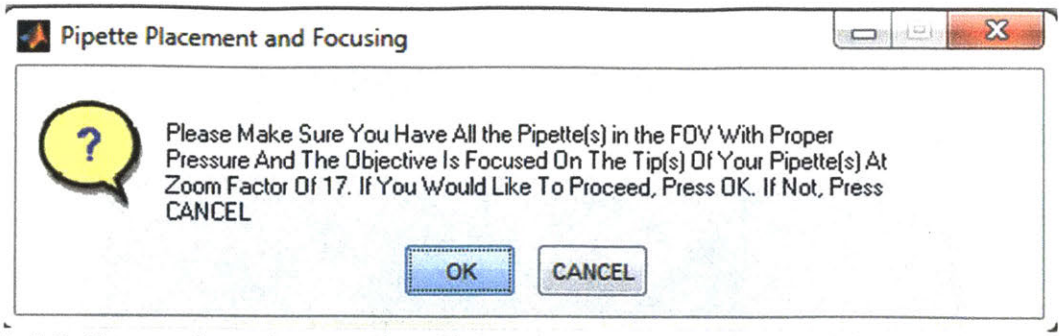

Figure A.5.8: Screenshot of a question dialog that appears after clicking the "Acquire Pipette Image Stack" pushbutton on the Imagepatcher GUI.

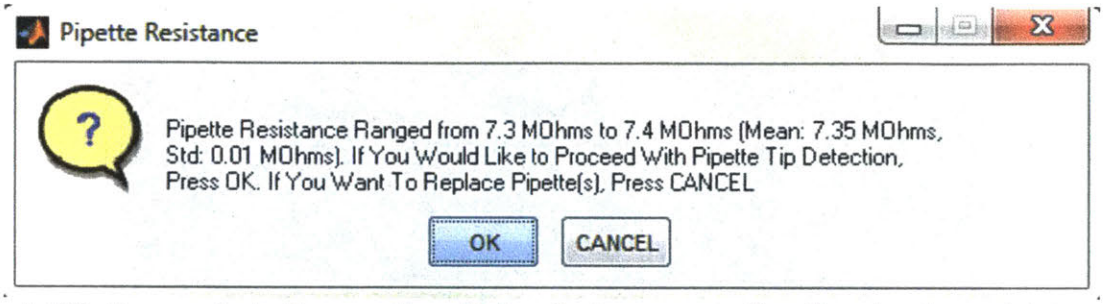

Figure A.5.9: Screenshot of a question dialog that appears after the pipette resistance is measured.

22. **Check the displayed pipette resistance and click "OK" on the question dialog (Figure A.5.9) if it is within an acceptable range (e.g., 5 – 7.5 MΩ).**

    If the pipette resistance is not within the acceptable range, click "CANCEL", remove the pipette, and repeat steps 11 – 22. When "OK" is clicked, the Imagepatcher acquires a z-stack around the pipette tip, detects the pipette tip, and displays the detected pipette tip in the left display window (Figure A.5.10).

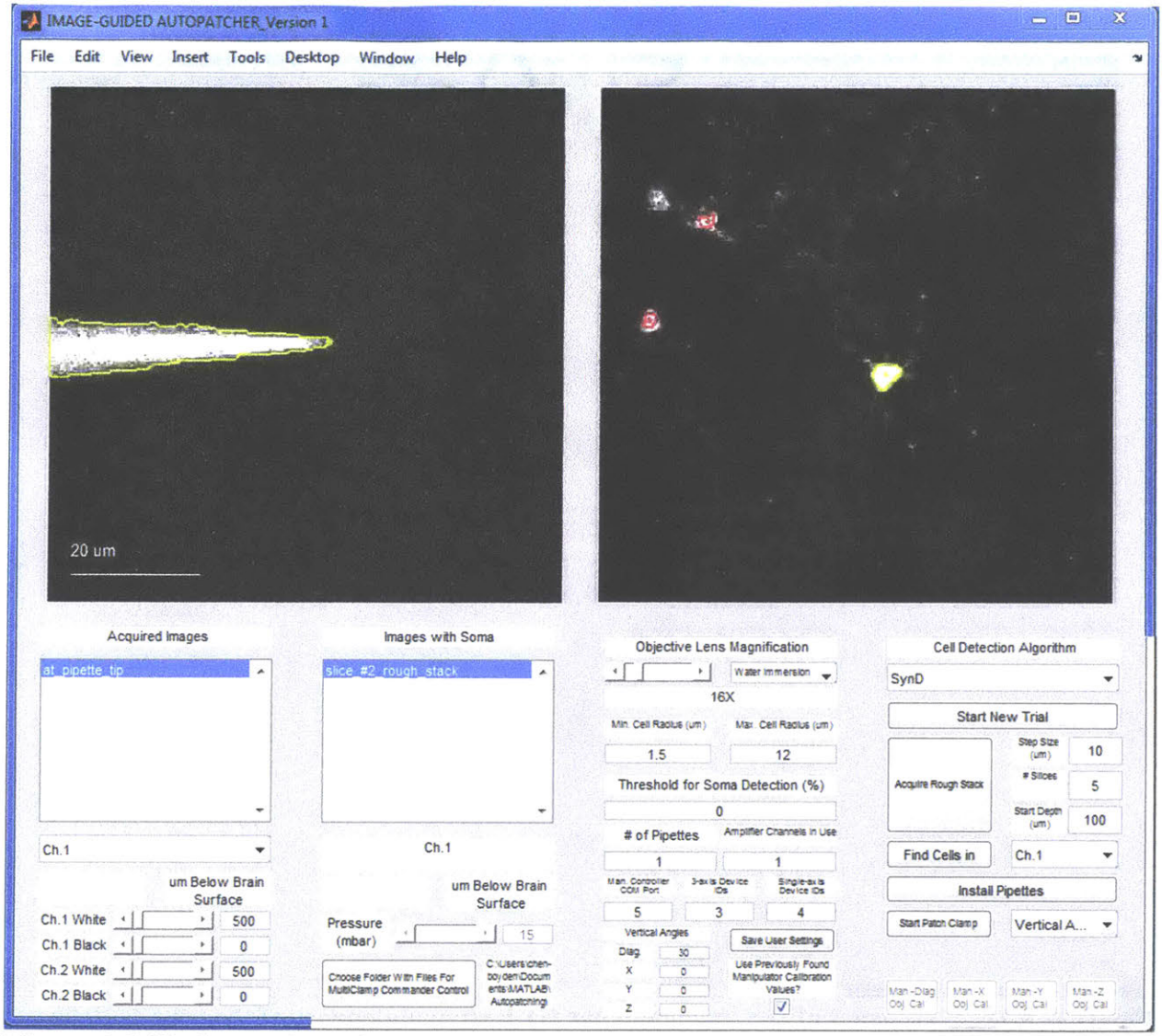

Figure A.5.10: Screenshot of the Imagepatcher GUI, showing the image of the pipette in the left display window, with the pipette's boundary outlined by yellow lines and a yellow star at its tip.

23. Click the "Start Patch Clamp" pushbutton on the Imagepatcher GUI to start the automated patching process.

The Imagepatcher automatically performs the second stage of micromanipulator-microscope motorized platform calibration and starts the patching process. Throughout the patching process, multiple images are displayed in the left and right display windows of the Imagepatcher GUI, with the left and the right display windows showing the pipette tip and the target cell respectively. The target cell contour and its centroid location are highlighted along with the location of the pipette tip (Figure A.5.11). Pipette resistance trace during the target cell approach will be displayed in a separate window (e.g., Figure A.5.12)

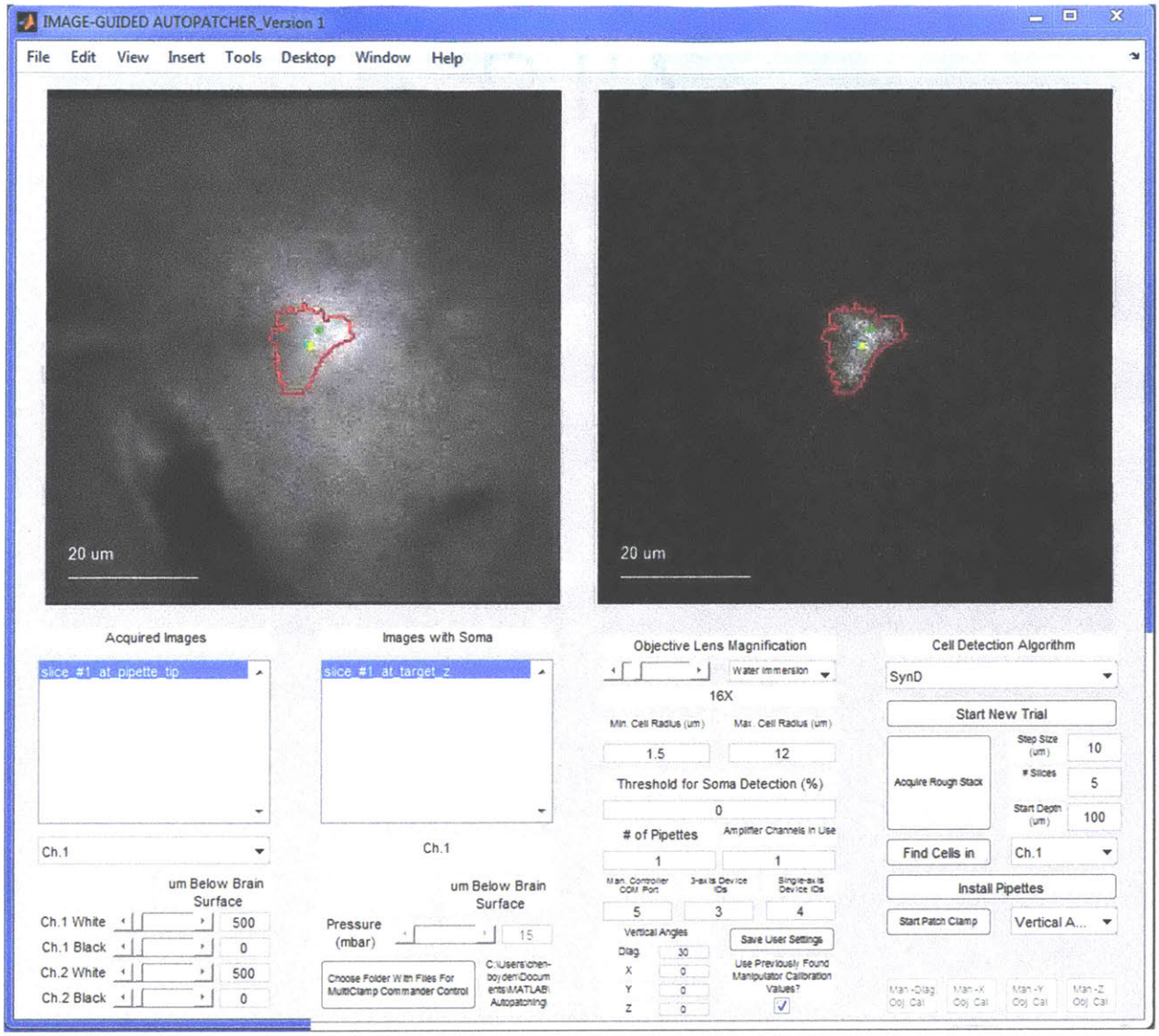

Figure A.5.11: Screenshot of the Imagepatcher GUI, showing images of the pipette (left) and the target cell (right) with the pipette tip (yellow dot), the target cell centroid (cyan dot), and the target cell contour (red outline) highlighted

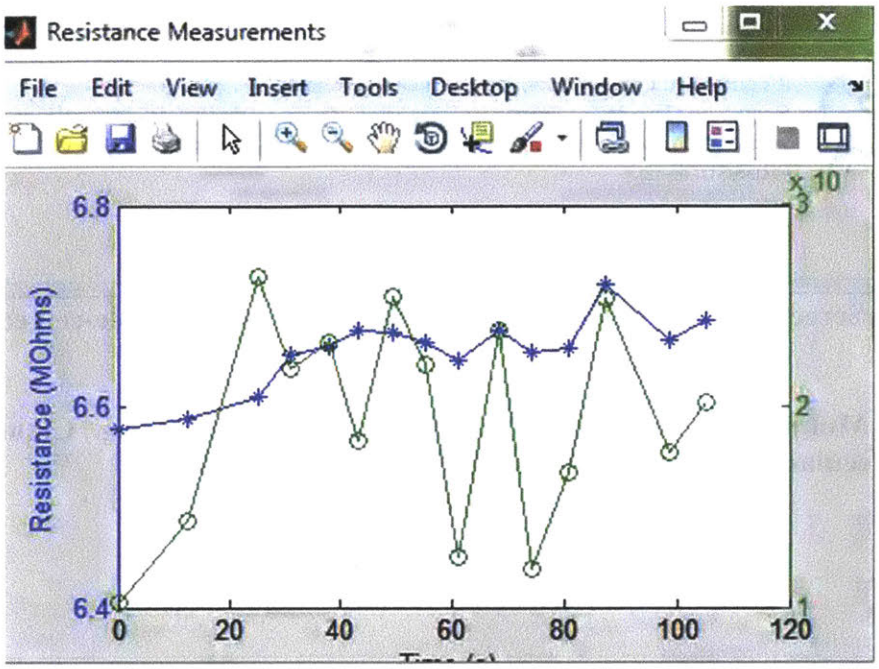

Figure A.5.12: Screenshot of a pipette resistance measurement window, showing the average (blue) and standard deviation (green) of 1-second long pipette resistance measurement following each z-step that the pipette takes towards the target cell.

24. **Click the "Break In For Whole Cell Recording" pushbutton that appears once a stable gigaseal is obtained.**

    Clicking the pushbutton starts the break-in process to achieve the whole-cell configuration. If cell-attached extracellular recordings are required, use Multiclamp Commander and the digitizer software (e.g., Clampex from Molecular Devices) to perform recordings.

25. **Click either "POSITIVE PRESSURE" and "NO POSITIVE PRESSURE" on the dialog box (Figure A.5.13) that appears after the whole-cell configuration is achieved, to select pipette pressure during recording.**

    Clicking "POSITIVE PRESSURE" causes the Imagepatcher to apply low positive pressure (same value as the one used in step 19), which may help prevent re-sealing and thus extend the recording duration. Clicking "NO POSITIVE PRESSURE" causes the Imagepatcher to release pressure from the pipette (i.e., the pipette is at the atmospheric pressure).

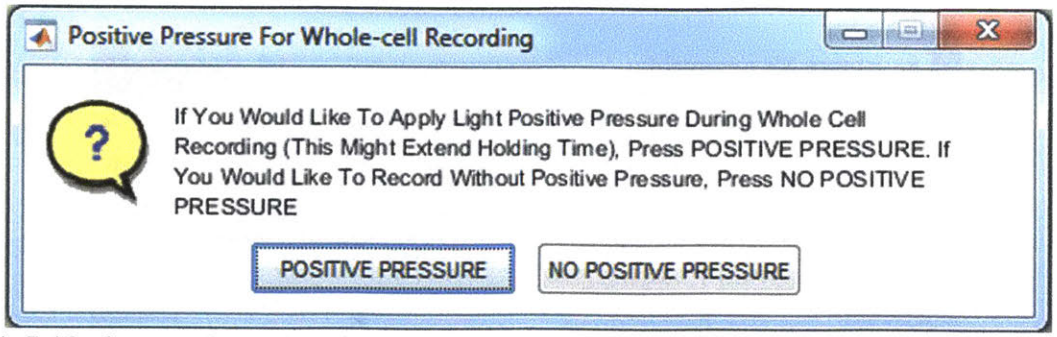

Figure A.5.13: Screenshot of a dialog box that appears when the whole-cell configuration is achieved.

26. **Use Multiclamp Commander and the digitizer software (e.g., Clampex from Molecular Devices) to perform whole-cell recordings.**

References

Altamura, C., Dell'Acqua, M.L., Moessner, R., Murphy, D.L., Lesch, K.P., and Persico, A.M. (2007). Altered neocortical cell density and layer thickness in serotonin transporter knockout mice: A quantitation study. Cereb. Cortex *17*, 1394–1401.

Amatniek, J.C., Hauser, W.A., DelCastillo-Castaneda, C., Jacobs, D.M., Marder, K., Bell, K., Albert, M., Brandt, J., and Stern, Y. (2006). Incidence and predictors of seizures in patients with Alzheimer's disease. Epilepsia *47*, 867–872.

Arispe, N., Pollard, H.B., and Rojas, E. (1996). Zn2+ interaction with Alzheimer amyloid beta protein calcium channels. Proc. Natl. Acad. Sci. U. S. A.

Atallah, B. V., Bruns, W., Carandini, M., and Scanziani, M. (2012). Parvalbumin-Expressing Interneurons Linearly Transform Cortical Responses to Visual Stimuli. Neuron *73*, 159–170.

Bartos, M., Vida, I., and Jonas, P. (2007). Synaptic mechanisms of synchronized gamma oscillations in inhibitory interneuron networks. Nat. Rev. Neurosci. *8*, 45–56.

Başar, E. (2013). Brain oscillations in neuropsychiatric disease. Dialogues Clin. Neurosci. *15*, 291–300.

Başar, E., Emek-Savaş, D.D., Güntekin, B., and Yener, G.G. (2016). Delay of cognitive gamma responses in Alzheimer's disease. NeuroImage Clin. *11*, 106–115.

Blanton, M.G., Lo Turco, J.J., and Kriegstein, A.R. (1989). Whole cell recording from neurons in slices of reptilian and mammalian cerebral cortex. J. Neurosci. Methods.

Buzsáki, G., and Draguhn, A. (2004). Neuronal olscillations in cortical networks. Science (80-.).

Callaway, E.M. (2005). A molecular and genetic arsenal for systems neuroscience. Trends Neurosci. *28*, 196–201.

Chen, I.-W., Helmchen, F., and Lutcke, H. (2015). Specific Early and Late Oddball-Evoked Responses in Excitatory and Inhibitory Neurons of Mouse Auditory Cortex. J. Neurosci. *35*, 12560–12573.

Clarke, S.D. (1993). Regulation of fatty acid synthase gene expression: an approach for reducing fat accumulation. J. Anim. Sci. *71*, 1957–1965.

Delorme, A., and Makeig, S. (2004). EEGLAB: an open source toolbox for analysis of single-trial EEG dynamics including independent component analysis. J. Neurosci. Methods.

Denk, W., Delaney, K.R., Gelperin, A., Kleinfeld, D., Strowbridge, B.W., Tank, D.W., and Yuste, R. (1994). Anatomical and functional imaging of neurons using 2-photon laser scanning microscopy. J. Neurosci. Methods *54*, 151–162.

Desai, N.S., Siegel, J.J., Taylor, W., Chitwood, R.A., and Johnston, D. (2015). MATLAB-based automated patch-clamp system for awake behaving mice. J. Neurophysiol. *114*, 1331–1345.

van Deursen, J.A., Vuurman, E.F.P.M., van Kranen-Mastenbroek, V.H.J.M., Verhey, F.R.J., and Riedel, W.J. (2011). 40-Hz steady state response in Alzheimer's disease and mild cognitive impairment. Neurobiol. Aging.

Van Deursen, J.A., Vuurman, E.F.P.M., Verhey, F.R.J., Van Kranen-Mastenbroek, V.H.J.M., and Riedel, W.J. (2008). Increased EEG gamma band activity in Alzheimer's disease and mild cognitive impairment. J. Neural Transm.

Dittgen, T., Nimmerjahn, A., Komai, S., Licznerski, P., Waters, J., Margrie, T.W., Helmchen, F., Denk, W., Brecht, M., and Osten, P. (2004). Lentivirus-based genetic manipulations of cortical neurons and their optical and electrophysiological monitoring in vivo. Proc. Natl. Acad. Sci. U. S. A. *101*, 18206–18211.

Dragicevic, E., Schiemann, J., and Liss, B. (2015). Dopamine midbrain neurons in health and

Parkinson's disease: Emerging roles of voltage-gated calcium channels and ATP-sensitive potassium channels. Neuroscience.
Dunlop, J., Bowlby, M., Peri, R., Vasilyev, D., and Arias, R. (2008). High-throughput electrophysiology: an emerging paradigm for ion-channel screening and physiology. Nat. Rev. Drug Discov. *7*, 358–368.
Edwards, F.A., Konnerth, A., Sakmann, B., and Takahashi, T. (1989). A thin slice preparation for patch clamp recordings from neurones of the mammalian central nervous system. Pflügers Arch. Eur. J. Physiol.
Engel, A.K., Fries, P., and Singer, W. (2001). Dynamic predictions: Oscillations and synchrony in top–down processing. Nat. Rev. Neurosci.
Fries, P. (2009). Neuronal Gamma-Band Synchronization as a Fundamental Process in Cortical Computation. Annu. Rev. Neurosci. *32*, 209–224.
Fries, P., Nikolić, D., and Singer, W. (2007). The gamma cycle. Trends Neurosci. *30*, 309–316.
Gentet, L.J., Avermann, M., Matyas, F., Staiger, J.F., and Petersen, C.C.H. (2010). Membrane Potential Dynamics of GABAergic Neurons in the Barrel Cortex of Behaving Mice. Neuron *65*, 422–435.
Gentet, L.J., Kremer, Y., Taniguchi, H., Huang, Z.J., Staiger, J.F., and Petersen, C.C. (2012). Unique functional properties of somatostatin-expressing GABAergic neurons in mouse barrel cortex. Nat Neurosci *15*, 607–612.
Gradinaru, V., Mogri, M., Thompson, K.R., Henderson, J.M., and Deisseroth, K. (2009). Optical deconstruction of parkinsonian neural circuitry. Science (80-.).
Gray, R., and Johnston, D. (1985). Rectification of single GABA-gated chloride channels in adult hippocampal neurons. J. Neurophysiol.
Greenberg, B.D., Gabriels, L.A., Jr, D.A.M., Rezai, A.R., Friehs, G.M., Okun, M.S., Shapira, N.A., Foote, K.D., Cosyns, P.R., Kubu, C.S., et al. (2010). Deep brain stimulation of the ventral internal capsule/ventral striatum for obsessive-compulsive disorder: worldwide experience. Mol. Psychiatry 2008 151 *15*, 64.
Hamill, O.P., Marty, A., Neher, E., Sakmann, B., and Sigworth, F.J. (1981). Improved patch-clamp techniques for high-resolution current recording from cells and cell-free membrane patches. Pfl??Gers Arch. Eur. J. Physiol. *391*, 85–100.
Häusser, M., and Margrie, T.W. (2014). Two-photon targeted patching and electroporation in vivo. Cold Spring Harb. Protoc. *2014*, 78–85.
Helmchen, F., and Denk, W. (2005). Deep tissue two-photon microscopy. Nat. Methods *2*, 932–940.
Herrmann, C.S. (2001). Human EEG responses to 1-100 Hz flicker: Resonance phenomena in visual cortex and their potential correlation to cognitive phenomena. Exp. Brain Res.
Herrmann, C.S., and Demiralp, T. (2005). Human EEG gamma oscillations in neuropsychiatric disorders. Clin. Neurophysiol. *116*, 2719–2733.
Hippenmeyer, S., Vrieseling, E., Sigrist, M., Portmann, T., Laengle, C., Ladle, D.R., and Arber, S. (2005). A developmental switch in the response of DRG neurons to ETS transcription factor signaling. PLoS Biol. *3*, 0878–0890.
Histed, M.H., Bonin, V., and Reid, R.C. (2009). Direct Activation of Sparse, Distributed Populations of Cortical Neurons by Electrical Microstimulation. Neuron.
Hochbaum, D.R., Zhao, Y., Farhi, S.L., Klapoetke, N., Werley, C.A., Kapoor, V., Zou, P., Kralj, J.M., MacLaurin, D., Smedemark-Margulies, N., et al. (2014). All-optical electrophysiology in mammalian neurons using engineered microbial rhodopsins. Nat. Methods.

Horton, N.G., Wang, K., Wang, C.C., and Xu, C. (2013). In vivo three-photon imaging of subcortical structures of an intact mouse brain using quantum dots. 2013 Conf. Lasers Electro-Optics Eur. Int. Quantum Electron. Conf. CLEO/Europe-IQEC 2013 *7*, 205–209.
Hutcheon, B., and Yarom, Y. (2000). Resonance, oscillation and the intrinsic frequency preferences of neurons. Trends Neurosci.
Iaccarino, H.F., Singer, A.C., Martorell, A.J., Rudenko, A., Gao, F., Gillingham, T.Z., Mathys, H., Seo, J., Kritskiy, O., Abdurrob, F., et al. (2016). Gamma frequency entrainment attenuates amyloid load and modifies microglia. Nature *540*, 230–235.
Ibáñez-Sandoval, O., Carrillo-Reid, L., Galarraga, E., Tapia, D., Mendoza, E., Gomora, J.C., Aceves, J., and Bargas, J. (2007). Bursting in Substantia Nigra Pars Reticulata Neurons In Vitro: Possible Relevance for Parkinson Disease. J. Neurophysiol.
Jelles, B., Scheltens, P., van der Flier, W.M., Jonkman, E.J., da Silva, F.H.L., and Stam, C.J. (2008). Global dynamical analysis of the EEG in Alzheimer's disease: Frequency-specific changes of functional interactions. Clin. Neurophysiol.
Jouhanneau, J.-S., Kremkow, J., Dorrn, A.L., and Poulet, J.F.A. (2015). In Vivo Monosynaptic Excitatory Transmission between Layer 2 Cortical Pyramidal Neurons. Cell Rep. *13*, 2098–2106.
Kalia, S.K., Sankar, T., and Lozano, A.M. (2013). Deep brain stimulation for Parkinson,s disease and other movement disorders. Curr. Opin. Neurol.
Kiskinis, E., Kralj, J.M., Zou, P., Weinstein, E.N., Zhang, H., Tsioras, K., Wiskow, O., Ortega, J.A., Eggan, K., and Cohen, A.E. (2018). All-Optical Electrophysiology for High-Throughput Functional Characterization of a Human iPSC-Derived Motor Neuron Model of ALS. Stem Cell Reports.
Kitamura, K., Judkewitz, B., Kano, M., Denk, W., and Hausser, M. (2008). Targeted patch-clamp recordings and single-cell electroporation of unlabeled neurons in vivo. Nat Methods *5*, 61–67.
Kodandaramaiah, S.B., Franzesi, G.T., Chow, B.Y., Boyden, E.S., and Forest, C.R. (2012). Automated whole-cell patch-clamp electrophysiology of neurons in vivo. Nat. Methods *9*, 585–587.
Kodandaramaiah, S.B., Holst, G.L., Wickersham, I.R., Singer, A.C., Franzesi, G.T., McKinnon, M.L., Forest, C.R., and Boyden, E.S. (2016). Assembly and operation of the autopatcher for automated intracellular neural recording in vivo. Nat. Protoc. *11*, 634–654.
Kodandaramaiah, S.B., Flores, F.J., Holst, G.L., Singer, A.C., Han, X., Brown, E.N., Boyden, E.S., and Forest, C.R. (2018). Multi-neuron intracellular recording in vivo via interacting autopatching robots. Elife.
Koenig, T., Prichep, L., Dierks, T., Hubl, D., Wahlund, L.O., John, E.R., and Jelic, V. (2005). Decreased EEG synchronization in Alzheimer's disease and mild cognitive impairment. Neurobiol. Aging.
Kolb, I., Stoy, W.A., Rousseau, E.B., Moody, O.A., Jenkins, A., and Forest, C.R. (2016). Cleaning patch-clamp pipettes for immediate reuse. Sci. Rep. *6*, 35001.
Komai, S., Denk, W., Osten, P., Brecht, M., and Margrie, T. (2006). Two-photon targeted patching (TPTP) in vivo. Nat. Protoc. *1*, 647–652.
Lee, A.K., Manns, I.D., Sakmann, B., and Brecht, M. (2006). Whole-Cell Recordings in Freely Moving Rats. Neuron *51*, 399–407.
Lee, A.K., Epsztein, J., and Brecht, M. (2009). Head-anchored whole-cell recordings in freely moving rats. Nat. Protoc. *4*, 385–392.
Li, L.Y., Xiong, X.R., Ibrahim, L.A., Yuan, W., Tao, H.W., and Zhang, L.I. (2015). Differential

Receptive Field Properties of Parvalbumin and Somatostatin Inhibitory Neurons in Mouse Auditory Cortex. Cereb. Cortex *25*, 1782–1791.
Llinás, R.R., Ribary, U., Jeanmonod, D., Kronberg, E., and Mitra, P.P. (1999). Thalamocortical dysrhythmia: A neurological and neuropsychiatric syndrome characterized by magnetoencephalography. Proc. Natl. Acad. Sci. U. S. A.
Long, B., Li, L., Knoblich, U., Zeng, H., and Peng, H. (2015). 3D Image-Guided Automatic Pipette Positioning for Single Cell Experiments in vivo. Sci. Rep. *5*, 18426.
Margrie, T.W., Brecht, M., and Sakmann, B. (2002). In vivo, low-resistance, whole-cell recordings from neurons in the anaesthetized and awake mammalian brain. Pflugers Arch. Eur. J. Physiol. *444*, 491–498.
Margrie, T.W., Meyer, A.H., Caputi, A., Monyer, H., Hasan, M.T., Schaefer, A.T., Denk, W., and Brecht, M. (2003). Targeted whole-cell recordings in the mammalian brain in vivo. Neuron *39*, 911–918.
Martorell, A.J., Paulson, A.L., Suk, H.-J., Abdurrob, F., Drummond, G.T., Guan, W., Young, J.Z., Kim, D.N.-W., Kritskiy, O., Barker, S.J., et al. (2019). Multi-sensory Gamma Stimulation Ameliorates Alzheimer's-Associated Pathology and Improves Cognition. Cell.
Mateo, C., Avermann, M., Gentet, L.J., Zhang, F., Deisseroth, K., and Petersen, C.C.H. (2011). In vivo optogenetic stimulation of neocortical excitatory neurons drives brain-state-dependent inhibition. Curr. Biol. *21*, 1593–1602.
Merrill, D.R., Bikson, M., and Jefferys, J.G.R. (2005). Electrical stimulation of excitable tissue: Design of efficacious and safe protocols. J. Neurosci. Methods.
Meyer, A.H., Blatow, M., Rozov, A., Monyer, H., and Katona, I. (2002). In vivo labeling of parvalbumin-positive interneurons and analysis of electrical coupling in identified neurons. J. Neurosci.
Miranda, P.C., Mekonnen, A., Salvador, R., and Ruffini, G. (2013). The electric field in the cortex during transcranial current stimulation. Neuroimage.
Mountcastle, V.B. (2003). Introduction. Computation in cortical columns. Cereb. Cortex *13*, 2–4.
Neher, E., and Sakmann, B. (1976). Single-channel currents recorded from membrane of denervated frog muscle fibres. Nature *260*, 799–802.
Nieweg, K., Andreyeva, A., Van Stegen, B., Tanriöver, G., and Gottmann, K. (2015). Alzheimer's disease-related amyloid-β induces synaptotoxicity in human iPS cell-derived neurons. Cell Death Dis.
Nowakowski, R.S. (2006). Stable neuron numbers from cradle to grave. Proc. Natl. Acad. Sci. U. S. A. *103*, 12219–12220.
Okada, Y. (2012). Patch clamp techniques from beginning to advanced protocols (Tokyo/New York: Springer).
Osipova, D., Pekkonen, E., and Ahveninen, J. (2006). Enhanced magnetic auditory steady-state response in early Alzheimer's disease. Clin. Neurophysiol.
Pala, A., and Petersen, C.C.H.C.H. (2015). In Vivo Measurement of Cell-Type-Specific Synaptic Connectivity and Synaptic Transmission in Layer 2/3 Mouse Barrel Cortex. Neuron *85*, 68–75.
Palop, J.J., Chin, J., Roberson, E.D., Wang, J., Thwin, M.T., Bien-Ly, N., Yoo, J., Ho, K.O., Yu, G.Q., Kreitzer, A., et al. (2007). Aberrant Excitatory Neuronal Activity and Compensatory Remodeling of Inhibitory Hippocampal Circuits in Mouse Models of Alzheimer's Disease. Neuron *55*, 697–711.
Pastor, M.A., Artieda, J., Arbizu, J., Marti-Climent, J.M., Peñ, I., and Masdeu, J.C. (2002). Activation of Human Cerebral and Cerebellar Cortex by Auditory Stimulation at 40 Hz. J.

Neurosci.
Pei, X., Volgushev, M., Vidyasagar, T.R., and Creutzfeldt, O.D. (1991). Whole cell recording and conductance measurements in cat visual cortex in-vivo. Neuroreport *2*, 485–488.
Perin, R., and Markram, H. (2013). A Computer-assisted Multi-electrode Patch-clamp System. J. Vis. Exp. e50630.
Piatkevich, K.D., Suk, H.J., Kodandaramaiah, S.B., Yoshida, F., DeGennaro, E.M., Drobizhev, M., Hughes, T.E., Desimone, R., Boyden, E.S., and Verkhusha, V. V. (2017). Near-Infrared Fluorescent Proteins Engineered from Bacterial Phytochromes in Neuroimaging. Biophys. J.
Pologruto, T.A., Sabatini, B.L., and Svoboda, K. (2003). ScanImage: Flexible software for operating laser scanning microscopes. Biomed. Eng. Online *2*, 13.
Ribary, U., Ioannides, A.A., Singh, K.D., Hasson, R., Bolton, J.P., Lado, F., Mogilner, A., and Llinás, R. (1991). Magnetic field tomography of coherent thalamocortical 40-Hz oscillations in humans. Proc. Natl. Acad. Sci. *88*, 11037–11041.
Runyan, C.A., Schummers, J., Van Wart, A., Kuhlman, S.J., Wilson, N.R., Huang, Z.J., and Sur, M. (2010). Response Features of Parvalbumin-Expressing Interneurons Suggest Precise Roles for Subtypes of Inhibition in Visual Cortex. Neuron *67*, 847–857.
Sakmann, B., and Neher, E. (1984). Patch Clamp Techniques for Studying Ionic Channels in Excitable Membranes. Annu. Rev. Physiol.
Seeley, W.W., Crawford, R.K., Zhou, J., Miller, B.L., and Greicius, M.D. (2009). Neurodegenerative Diseases Target Large-Scale Human Brain Networks. Neuron.
Sigworth, F.J., and Neher, E. (1980). Single Na+channel currents observed in cultured rat muscle cells. Nature.
Šimić, G., Babić Leko, M., Wray, S., Harrington, C., Delalle, I., Jovanov-Milošević, N., Bažadona, D., Buée, L., de Silva, R., Giovanni, G. Di, et al. (2016). Tau protein hyperphosphorylation and aggregation in alzheimer's disease and other tauopathies, and possible neuroprotective strategies. Biomolecules *6*, 2–28.
Singer, W., and Gray, C.M. (1995). Visual Feature Integration and the Temporal Correlation Hypothesis. Annu. Rev. Neurosci. *18*, 555–586.
Spencer, K.M., Nestor, P.G., Niznikiewicz, M. a, Salisbury, D.F., Shenton, M.E., and McCarley, R.W. (2003). Abnormal neural synchrony in schizophrenia. J. Neurosci. *23*, 7407–7411.
Sperling, R.A., Dickerson, B.C., Pihlajamaki, M., Vannini, P., LaViolette, P.S., Vitolo, O. V., Hedden, T., Becker, J.A., Rentz, D.M., Selkoe, D.J., et al. (2010). Functional alterations in memory networks in early alzheimer's disease. NeuroMolecular Med.
Stam, C.J., Van Cappellen van Walsum, A.M., Pijnenburg, Y.A.L., Berendse, H.W., De Munck, J.C., Scheltens, P., and Van Dijk, B.W. (2002). Generalized synchronization of MEG recordings in Alzheimer's disease: Evidence for involvement of the gamma band. J. Clin. Neurophysiol. *19*, 562–574.
Steinmeyer, J.D., and Yanik, M.F. (2012). High-throughput single-cell manipulation in brain tissue. PLoS One *7*, e35603.
Stoy, W.A., Kolb, I., Holst, G., Liew, Y.J., Pala, A., Yang, B., Boyden, E.S., Stanley, G.B., and Forest, C.R. (2017). Robotic navigation to sub-cortical neural tissue for intracellular electrophysiology in vivo. J. Neurophysiol. jn.00117.2017.
Stuart, G.J., Dodt, H.U., and Sakmann, B. (1993). Patch-clamp recordings from the soma and dendrites of neurons in brain slices using infrared video microscopy. Pflugers Arch. *423*, 511–518.
Suk, H.J., van Welie, I., Kodandaramaiah, S.B., Allen, B., Forest, C.R., and Boyden, E.S. (2017).

Closed-Loop Real-Time Imaging Enables Fully Automated Cell-Targeted Patch-Clamp Neural Recording In Vivo. Neuron.
Svoboda, K., Denk, W., Kleinfeld, D., and Tank, D.W. (1997). In vivo dendritic calcium dynamics in neocortical pyramidal neurons. Nature *385*, 161–165.
Ting, J.T., Daigle, T.L., Chen, Q., and Feng, G. (2014). Acute brain slice methods for adult and aging animals: Application of targeted patch clamp analysis and optogenetics. Methods Mol. Biol.
Tsien, J.Z., Chen, D.F., Gerber, D., Tom, C., Mercer, E.H., Anderson, D.J., Mayford, M., Kandel, E.R., and Tonegawa, S. (1996). Subregion- and cell type-restricted gene knockout in mouse brain. Cell *87*, 1317–1326.
Uhlhaas, P.J., and Singer, W. (2006). Neural Synchrony in Brain Disorders: Relevance for Cognitive Dysfunctions and Pathophysiology. Neuron *52*, 155–168.
Uhlhaas, P.J., and Singer, W. (2010). Abnormal neural oscillations and synchrony in schizophrenia. Nat. Rev. Neurosci. *11*, 100–113.
Verret, L., Mann, E.O., Hang, G.B., Barth, A.M.I., Cobos, I., Ho, K., Devidze, N., Masliah, E., Kreitzer, A.C., Mody, I., et al. (2012). Inhibitory interneuron deficit links altered network activity and cognitive dysfunction in alzheimer model. Cell *149*, 708–721.
Vinck, M., Oostenveld, R., Van Wingerden, M., Battaglia, F., and Pennartz, C.M.A. (2011). An improved index of phase-synchronization for electrophysiological data in the presence of volume-conduction, noise and sample-size bias. Neuroimage.
Wang, X.-J. (2010). Neurophysiological and Computational Principles of Cortical Rhythms in Cognition. Physiol. Rev.
Wang, H., Ge, Y., Song, A., Li, B., and Xu, B. (2015a). The vibro-tactile stimulations experiment to verify the optimal resonance frequency of human's tactile system. In 2015 IEEE International Conference on Information and Automation, ICIA 2015 - In Conjunction with 2015 IEEE International Conference on Automation and Logistics, p.
Wang, J., Fang, Y., Wang, X., Yang, H., Yu, X., and Wang, H. (2017). Enhanced gamma activity and cross-frequency interaction of resting-state electroencephalographic oscillations in patients with Alzheimer's disease. Front. Aging Neurosci.
Wang, Y., Cella, M., Mallinson, K., Ulrich, J.D., Young, K.L., Robinette, M.L., Gilfillan, S., Krishnan, G.M., Sudhakar, S., Zinselmeyer, B.H., et al. (2015b). TREM2 lipid sensing sustains the microglial response in an Alzheimer's disease model. Cell.
van Welie, I., Roth, A., Ho, S.S.N., Komai, S., and Häusser, M. (2016). Conditional Spike Transmission Mediated by Electrical Coupling Ensures Millisecond Precision-Correlated Activity among Interneurons In Vivo. Neuron *90*, 810–823.
Wilson, N.R., Schummers, J., Runyan, C.A., Yan, S.X., Chen, R.E., Deng, Y., and Sur, M. (2013). Two-way communication with neural networks in vivo using focused light. Nat. Protoc. *8*, 1184–1203.
Wu, Q., Kolb, I., Callahan, B.M., Su, Z., Stoy, W., Kodandaramaiah, S.B., Neve, R.L., Zeng, H., Boyden, E.S., Forest, C.R., et al. (2016). Integration of autopatching with automated pipette and cell detection in vitro. J. Neurophysiol. *116*, 1564–1578.
Zhang, Z., Russell, L.E., Packer, A.M., Gauld, O.M., and Häusser, M. (2018). Closed-loop all-optical interrogation of neural circuits in vivo. Nat. Methods.